

Low Cost Manufacturing of Light Trapping Features on Multi-Crystalline Silicon Solar Cells: Jet Etching Method and Cost Analysis

by

Amine Berrada Sounni

B.S. Mechanical Engineering,
UC Berkeley, Dec 2005

Submitted to the Department of Mechanical Engineering
and the Engineering System Division
in Partial Fulfillment of the Requirements for the Degrees of

Master of Science in Mechanical Engineering
and Master of Science in Technology and Policy

at the
Massachusetts Institute of Technology
June 2010

©2010 Massachusetts Institute of Technology. All rights reserved

Signature of Author _____
Department of Mechanical Engineering and Engineering Systems Division
May 14, 2010

Certified by _____
Emanuel M. Sachs
Fred Fort Flowers and Daniel Fort Flowers Professor of Mechanical Engineering
Thesis Supervisor

Certified by _____
Frank R. Field
Senior Research Engineer and Associate Director of TPP
Thesis Reader

Accepted by _____
David E. Hardt
Ralph E. and Eloise F. Cross Professor of Mechanical Engineering
Chair, Departmental Committee on Graduate Studies

Accepted by _____
Dava J. Newman
Professor of Aeronautics and Astronautics and Engineering Systems
Director, Technology and Policy Program

Low Cost Manufacturing of Light Trapping Features on Multi-Crystalline Solar Cells: Jet Etching Method and Cost Analysis

by

Amine Berrada Sounni

Submitted to the Department of Mechanical Engineering and the Engineering Systems Division on May 14, 2010 in Partial Fulfillment of the Requirements for the Degrees of Master of Science in Mechanical Engineering and Master of Science in Technology and Policy

ABSTRACT

An experimental study was conducted in order to determine low cost methods to improve the light trapping ability of multi-crystalline solar cells. We focused our work on improving current wet etching methods to achieve the desired light trapping features which consists in micro-scale trenches with parabolic cross-sectional profiles with a target aspect ratio of 1.0. The jet etching with a hard mask method, which consists in impinging a liquid mixture of hydrofluoric, nitric and acetic acids through the opening of hard mask, was developed.

First, a computational fluid dynamics simulation was conducted to determine the desired jet velocity and angle to be used in our experiments. We find that using a jet velocity of 3 m/s and a jetting angle of 45° yields the necessary flow characteristics for etching high aspect ratio features.

Second, we performed experiments to determine the effect of jet etching using a photo-resist mask and thermally grown silicon oxide mask on multiple silicon substrates : $\langle 100 \rangle$, $\langle 110 \rangle$, $\langle 111 \rangle$ and multi-crystalline silicon. Compared to a baseline of etching with no jet, we find that the jet etching process can improve the light trapping ability of the baseline features by improving their aspect ratio up to 65.2% and their light trapping ability up to 38.1%. The highest aspect ratio achieved using the jet etching process was 0.62. However, it must be noted that the repeatability of the results was not consistent: significant variations in the results of the same experiment occurred, making the jet etching process promising but difficult to control.

Finally, we performed a cost analysis in order to determine the minimum efficiency that a jet etching process would have to achieve to be cost competitive and its corresponding features aspect ratio. We find that a minimum cell efficiency of 16.63% and feature aspect ratios of 0.57 are necessary for cost competitiveness with current solar cell manufacturing technology.

Thesis Supervisor: Emanuel M. Sachs
Fred Fort Flowers and Daniel Fort Flowers Professor of Mechanical Engineering

Acknowledgments

This work and my academic endeavors would not have been possible without the advice and encouragements of several people that I would like to thank warmly.

First, I would like to thank my advisor Prof. Ely Sachs whose guidance and mentoring have been key to the success of this project and my academic work. His support and flexibility for my desire to pursue a dual degree in Mechanical Engineering and Technology and Policy afforded me the opportunity to expand my technical training with an education in policy. His encouragements and mentorship for my extra-curricular activities have thought me valuable skills for my career development.

I also would like to acknowledge several members of the Sachs group for their contribution to my work. Dr. Jim Bredt has participated greatly to developing the jet etching process and ensuring the safety of with my experimental work. Jim Serdy was instrumental in the design and fabrication of the jet etching apparatus as well as being an invaluable resource for my experimental work. Laura Zaganjori has been a resourceful help throughout my research work and academic experience at MIT.

My thanks also go to my labmates: Anjuli Appapillai, Alison Greenlee, Chris Ruggiero, Christoph Sachs, David Li and Eerik Hantsoo. Each, in their own way, have participated immensely to the enrichment of my experience at MIT.

My cost analysis study would not have been possible without the close supervision Dr. Richard Roth, whose help has been indispensable to the success of this work. I would like to thank Prof. Frank Field for his advice on my thesis work. And last but not least, I would like to take Andrew Gabor for his valuable explanations of the cell making process.

This work would not have been possible without the generous funding supporting it. I would like to thank TOTAL company for awarding me a wonderful two-year fellowship, allowing me to pursue research in the field of energy. I would also like to thank the Chesonis Foundation for their support for both my academic research and career development activities.

Finally, and above all, I would like to thank my parents: Azzedine and Rachida, and my brothers: Marwane, Younes, Hicham and Reda for their unconditional moral support and for making it possible for me to reach this accomplishment. I dedicate this work to them.

Table of Contents

- Acknowledgments 4
- List of Figures 8
- Chapter 1 – Background 12
 - 1.1. Energy Landscape..... 12
 - 1.2. Solar Energy 14
 - 1.2.1. Resource Assessment: 14
 - 1.2.2. Market history for PV 15
 - 1.3. Multi-crystalline Photovoltaic Cells..... 17
 - 1.4. Surface patterning methods: 18
 - 1.4.1 Random pyramids: 19
 - 1.4.2 Texturing of multi-Si:..... 20
- Chapter 2 - This work’s approach..... 23
 - 2.1 Theoretical Determination of Ideal Cross-section Shape..... 23
 - 2.2 Isotropic etching with high Aspect Ratio 25
 - 2.2.1 The H-N-A etching system: 25
 - 2.2.2 Boundary layer removal 26
 - 2.3 Magnetic particle etching..... 30
- Chapter 3 - Jet Etching..... 34
 - 3.1 Jet Etching introduction 34
 - 3.2 Jet Etching Simulation 35
 - 3.2.1 Description of Simulation Method..... 35
 - 3.2.2 Jet Velocity..... 38
 - 3.2.3 Impinging Jet at 45 degree Angle..... 44
 - 3.3 Conclusion: 48
- Chapter 4 - Methodology for Evaluating Trench Cross-section Quality 49
 - 4.1 Total Internal Reflection:..... 49
 - 4.2 Q-Factor Definition: 50
 - 4.3 Aspect Ratio Definition: 52
 - 4.4 Theoretical Limits: 53
 - 4.5 Measurement Method..... 57

Chapter 5 - Jet Etching Experimental Set Up and Hardware:	59
5.1 Etching Solution used.....	59
5.2 Stationary Jet Apparatus Description	59
5.3 Moving Jet Apparatus Description.....	61
5.3.1 The Sample Holder:.....	61
5.3.2 The Etch bath Over-Flow Container:.....	65
5.3.3 The Jet Nozzle Holder.....	69
5.3.4 The Revolving Mechanism.....	70
5.4 Technical Information on the Apparatus Operation.....	76
Chapter 6 - Experiments and Results	78
6.1 Single Crystalline Silicon and Photo-Resist Mask.....	78
6.1.1 Single Si <100> + Photo-Resist + Stationary Jet	78
6.2 Silicon + Oxide mask + Photo-Resist	81
6.2.1 Single Si + Photo-Resist + Oxide <100>	83
6.2.2 Single Si <111> + Photo-Resist + Oxide	85
6.2.3 Single Si <110> + Photo-Resist + Oxide	87
6.2.3 Multi Si + Photo-Resist + Oxide + Jet.....	89
6.2.4 Polished multi-crystalline Silicon + Photo-Resist + SiO ₂	91
6.3 Silicon + Oxide mask + PR (BOE Opening)	93
6.3.1 Silicon + Oxide + PR + BOE : <100> Si	94
6.3.2 Silicon + Oxide + PR + BOE : <110> Si	95
6.3.3 Silicon + Oxide + PR + BOE : <111> Si	97
6.4 Discussion of Results.....	99
6.5 Conclusion and Future Work.	102
Chapter 7 Cost Analysis.	103
7.1 Introduction.....	103
7.2 Cell Making Process Description.....	103
7.2.1. SDR removal + Iso- Texture:	104
7.2.2 Doping Step and In-line Furnace:.....	106
7.2.3 PSG removal:.....	108
7.2.4 Silicon Nitride PECVD:	109
7.2.5 Metallization:.....	110

7.2.6 Cell Testing and Sorting:.....	111
7.2.7 Additional Steps	112
7.3 Cost of Cell Making Process:.....	113
7.3.1 Iso-Texture.....	114
7.3.2 Texture + Mask	115
7.3.3 Jet Etching + Mask.....	116
7.4 Sensitivity Analysis.....	118
7.4.1 Sensitivity Analysis for Jet Texture with Iso-Texture.....	118
7.4.2 Sensitivity Analysis of Jet Texture with Texture + Mask	119
7.4.3 Sensitivity Analysis for Jet etching Cost and Texture + Mask cost.....	120
7.5 Implications of efficiency for aspect ratio.....	122
7.6 Discussion and Conclusion	124
Bibliography	126
Appendix A:.....	129

List of Figures

Figure 1.1: World Marketed Energy Consumption (4)	12
Figure 1.2: Total Energy Consumption in US in quadrillion Btu (2006) (5). The US consumes more energy than it produces and is dependent on energy imports.....	13
Figure 1.3: Energy Consumption by Fuel (Quadrillion BTU) (5).....	14
Figure 1.4: PV solar radiation map in US (6).....	15
Figure 1.5: Experience Curve for PV module cost (1976-2005) (source IEA)(7). The cost of PV modules has been steadily decreasing with cumulative capacity.....	16
Figure 1.6: PV module cost (8)	17
Figure 1.7: Solar cell efficiency increase (9).....	18
Figure 1.8: Incident light on a flat substrate is reflected back to the atmosphere and never enters the Silicon. A textured cell provides reflective surfaces directing the reflected light into the material itself. (10).....	19
Figure 1.9: Light path lengthening due to surface texturing. When light rays enter a silicon substrate, they travel until they are absorbed by the silicon. If rays take a longer path within the silicon, they have a greater chance of being absorbed. A textured silicon substrate helps trap rays better, by providing inclined surfaces which make it harder to a ray to strike at an angle less than the critical angle (10).....	19
Figure 1.10: SEM micrograph of Random Pyramids Fabricated Using KOH Etch (12).....	20
Figure 1.11: Microwave Enhanced RIE resulting in ellipsoidal features with low reflectance.(14).....	21
Figure 1.12: Isotropic texturing of multi-crystalline Silicon using acidic etching(15). Acidic etching methods are used on the surface of multi-crystalline silicon to generate randomly etched feature which increase the light trapping ability of the cell.....	22
Figure 2.1: Cross-section of each parabola that was tested a) 1/4 aspect ratio parabola, b) 1/2 aspect ratio parabola, c) 3/4 aspect ration parabola, d) 1 aspect ration parabola, e) 1.5 aspect ratio and f) 2 aspect ratio parabola (10).....	24
Figure 2.2: Graph of the number of detector hits versus the aspect ratio of the parabola. The optimum Parabola has a unit aspect ratio (10)	24
Figure 2.3: Diffusion Barrier: the reactants for the dissolution reaction are limited by the presence of the products of the oxidation reaction which creates a diffusion barrier.....	27
Figure 2.4: Diffusion Barrier preferentially reduced to enable faster etching in the vertical direction	28
Figure 2.5: Fluid Boundary Layer Thickness: As fluid velocity increases, the thickness decreases and the start of the boundary layer has the smallest thickness.	29
Figure 2.6: Magnetic Etching Theory. As the steel particle brushes the surface of the sample it breaks the diffusion barrier, allowing fresh etching to enter in contact with the surface of the sample.	30
Figure 2.7: Magnetic Etching Apparatus.....	31
Figure 2.8: Magnetic Etching Sample. The etching pattern of the steel particle's motion on the surface of the sample is shown as the circular pattern on this picture.	31
Figure 2.9: Trench Profile - Profilometer Data.....	32
Figure 3.1: Schematic of jet etching process for large trenches.(24) Fresh etchant enters through the mask opening, reaches the bottom of the trench first at higher etch rates then as the etchant is depleted it etches the sidewalls at slower etch rates. This results is high aspect ratios features.....	34
Figure 3.2: CFD simulation - Side View 3m/s , T = 25C. The jetted etchant enters the trench at a velocity of about 0.6m/s indicating the presence of local jet effect at the entrance of the trench.....	35
Figure 3.3: CFD simulation 3m/s at T =25 C	36
Figure 3.4: 90° and 45° jet impingement angle (SHOW 3-D for 90 and 45 deg)	38

Figure 3.5: Jet velocity simulation results - 3m/s (Cross-section view). As the trenches cross-section widens the jet is less capable of reaching the bottom of the trench.	39
Figure 3.6: Jet velocity simulation results: 3 m/s (side view).....	40
Figure 3.7: Jet velocity simulation results: 5 m/s (cross-section view). At 5 m/s the jet reaches deeper into the trench than at 3m/s even when the trench cross-section is widening.	41
Figure 3.8: Jet velocity simulation results: 5 m/s (side view).....	42
Figure 3.9: Jet velocity simulation results: 10 m/s (cross-section view). At 10m/s the jet penetrates even deeper into the trench than at 5 m/s indicating that higher jet velocities are desirable for the jet etching process.	43
Figure 3.10: Penetration of the impinging jet as a function of speed. As jet velocity increases the etchant penetrates deeper into the trenches.	43
Figure 3.11: Simulation results for jet velocity 3 m/s and angle of 45° (cross-section view). At 45°, the jet enters deeper into the trench than a 90° jet for the same jet velocity.....	44
Figure 3.12: Simulation results for jet velocity 3 m/s and angle of 45 degrees (side view).	46
Figure 3.13: Simulation results for jet velocity 5 m/s and angle of 45 degrees (cross-section view).....	46
Figure 3.14: Simulation results for jet velocity 5 m/s and angle of 45 degrees (side view)	47
Figure 3.15: Simulation results for jet velocity 10 m/s and angle of 45 degrees (cross-section view)	48
Figure 4.1: Total Internal Reflection (26). A ray of light that is incident of the interface at an angle greater than the critical angle is reflected.....	50
Figure 4.2: Total Internal Reflection (27).....	50
Figure 4.3: Light Bouncing on Surface of Trench. Incident light at locations with slopes higher than $\theta_c / 2$ are absorbed immediately by the substrate (a), the ones incident at slope about $\theta_c / 2$ are reflected out of the trench but recaptured by the glass (b). Finally incident light at slopes lower than $\theta_c / 2$ is reflected of the trench and escapes through the glass.....	51
Figure 4.4: Illustration of trench quality.....	52
Figure 4.5: High Aspect Ratio Trench. When the aspect ratio of a trench increases, it becomes capable of trapping light that would have escaped at lower aspect ratios.....	53
Figure 4.6: Parabola of aspect ratio of ½. Light incident at 20.9° escapes the trench but is captured by the glass through TIR.	54
Figure 4.7: Parabola of Aspect Ratio 1. Light incident at 20.9° is captured by the sidewalls of the trench of aspect ratio 1.....	55
Figure 4.8: Parabola of aspect ratio 0.65 (limiting case). At this aspect ratio incident light at 20.9° is absorbed by the top of the trench and is the limiting aspect ratio for the Q-factor method to be used.....	56
Figure 4.9: Illustration of method used to measure Q-factor and Aspect Ratio. The No Double Bounce region is the ratio of non-absorbing area over the width of the trench.	57
Figure 5.1: Stationary Etch Apparatus.....	60
Figure 5.2: 3-D model of sample holder	62
Figure 5.3: Wax Pocket and Sample Pocket Dimensions in Inches.....	62
Figure 5.4: Linear Position vs Angular Position. Over the sample region the jet nozzle has a constant linear velocity.....	63
Figure 5.5: Side-view of sample holder	64
Figure 5.6: Top view of sample holder.	64
Figure 5.7: Dimension details for Sample holder.....	65
Figure 5.8: Sample Holder Picture.....	65
Figure 5.9: Overflow container - Side View	66
Figure 5.10: Over-flow container top view.....	67
Figure 5.11: Etch Bath Container (view showing magnet locations).....	67

Figure 5.12: Over-flow container 3D view	67
Figure 5.13: Over-flow container Dimensions	68
Figure 5.14: Over-flow container 3D view	68
Figure 5.15: Jet nozzle holder 45°	69
Figure 5.16: Jet Nozzle Holder 90°	70
Figure 5.17: Jet Nozzle Holder 90°	70
Figure 5.18: Revolving Mechanism.....	72
Figure 5.19: Revolving Mechanism – Top View	72
Figure 5.20: Revolving Mechanism – Front View.....	73
Figure 5.21: Apparatus Assembly	73
Figure 5.22: Apparatus Assembly - back view	74
Figure 5.23: Apparatus Assembly	74
Figure 5.24: Back Plate / Plenum - Back View	75
Figure 5.25: Back Plate / Plenum - Front View	75
Figure 5.26: Plenum Back Cover.....	75
Figure 5.27: Apparatus Picture.....	77
Figure 5.28: Apparatus Picture (view of sample holder and over-flow container)	77
Figure 6.1: Silicon sample covered with a pattern photo-resist mak.	78
Figure 6.2: Si <100> + PR + Jet etch (AR = 0.62, Q = 0.277).....	79
Figure 6.3: <100> Si + PR control experiment (AR = 0.359, Q = 0.3356)	80
Figure 6.4: Moving Jet Nozzle Apparatus	81
Figure 6.5: Diagram of silicon substrate covered with hard SiO ₂ mask and patterned photo-resist layer	82
Figure 6.6: Diagram of Silicon substrate covered with hard SiO ₂ and Photo-Resist after opening	82
Figure 6.7: Control Experiment for <100> + SiO ₂ + PR (AR = 0.49, Q = 0.3152)	83
Figure 6.8: <100> + SiO ₂ +PR Jet etched (AR = 0.54, Q = 0.273)	84
Figure 6.9: SiO ₂ Mask effect on local etch. Regions in the vicinity of the mask are etched slower which result in more vertical side-wall.	85
Figure 6.10: <111> Si + SiO ₂ +PR – Control (AR = 0.479, Q = 0.5297)	86
Figure 6.11: <111> Si + SiO ₂ + PR - with jet (AR = 0.422, Q = 0.4598)	87
Figure 6.12: <110> Si + SiO ₂ + PR – Control (AR = 0.2178, Q =0.6247)	88
Figure 6.13: <110> Si +SiO ₂ +PR - with Jet (AR = 0.3598, Q = 0.615)	88
Figure 6.14: Multi-Si + SiO ₂ + PR – Control (AR = 0.5722, Q = 0.1359)	90
Figure 6.15: Multi-Si + SiO ₂ + PR - with Jet (AR = 0.5316, Q = 0.4373)	91
Figure 6.16: Polished Multi + SiO ₂ + PR - Control (AR = 0.4398, Q = 0.4039)	92
Figure 6.17: Polished Multi - Si + SiO ₂ + PR + Jet (AR = 0.4796, Q = 0.3170)	93
Figure 6.18: <100> Si + SiO ₂ + PR + BOE – Control (AR = 0.3059, Q = 0.2238)	94
Figure 6.19: <100> Si + SiO ₂ + PR + BOE - with Jet (AR = 0.4, Q = 0.228).....	95
Figure 6.20: <110> Si + SiO ₂ + PR + BOE – Control (AR = 0.2751, Q = 0.54).....	96
Figure 6.21: <110> Si + SiO ₂ + PR + BOE - with Jet (AR= 0.3395, Q = 0.4995)	96
Figure 6.22: <111> Si + SiO ₂ + PR + BOE – Control (AR = 0.4434, Q = 0.4705)	97
Figure 6.23: <111> Si + SiO ₂ + PR + BOE - with Jet (AR = 0.4412, Q = 0.291)	98
Figure 7.1: Cell processing steps diagram.....	104
Figure 7.2: Comparison of two cell making processes with the jet etching process (assuming the jet etcher additional cost is 20% more than iso-texturing equipment and the masking step is the same cost as the doping step)	114
Figure 7.3: Sensitivity analysis for Jet texture compared to Iso-Texture.....	119

Figure 7.4: Sensitivity Analysis for Jet Texture compared to Texture + Mask	120
Figure 7.5: Sensitivity analysis for jet etcher cost and masking cost.....	121
Figure 7.6: Relationship between aspect ratios and detector hits	122
Figure 7.7: Relationship between Q and A.R.	123
Figure 7.8: Relationship between aspect ratio and cell efficiency	124

Chapter 1 – Background

It is now a well established reality that the world is facing an increasingly severe energy crisis. Energy demand has stretched out resources to peak supply levels, driving energy prices to record levels. Renewable energy, an environmental effort in its beginnings, is now an indispensable energy source which must be developed to its full potential in order to meet the increase in energy demand and tackle the problem of climate change. Solar energy, with an average power of 1.740×10^{17} W (1) reaching the earth, represents the largest energy resource on earth.

1.1. Energy Landscape

As the world's population increases, tripling since the 1930s (2) and reaching 6.5 billion in 2005 (3), energy needs will have to increase with population and economic development. The world's energy consumption for year 2006 was 472 Quadrillion Btu (497.96×10^{18} Joules) and expected to reach 508 Quadrillion Btu (535.94×10^{18} Joules) by 2010 as shown in Figure 1.1.

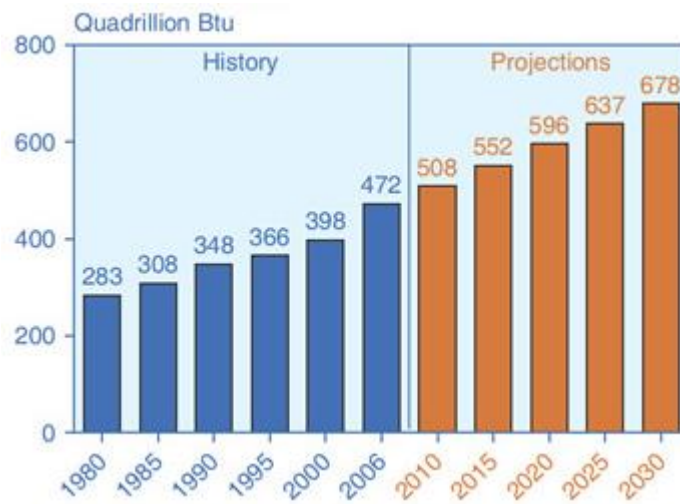


Figure 1.1: World Marketed Energy Consumption (4).

The United States alone represents about 25% of this energy consumption. Figure 1.2 below shows the historical energy consumption in the US up to 2006 and projection from then onwards. It is clear from this graph that the energy consumption has been increasing steadily with projections of further increase in the future. Energy production in the US is however lower than its consumption exposing the

significant energy imports the US faces in meeting its energy demand, which creates dependence on energy imports that have become a national security concern.

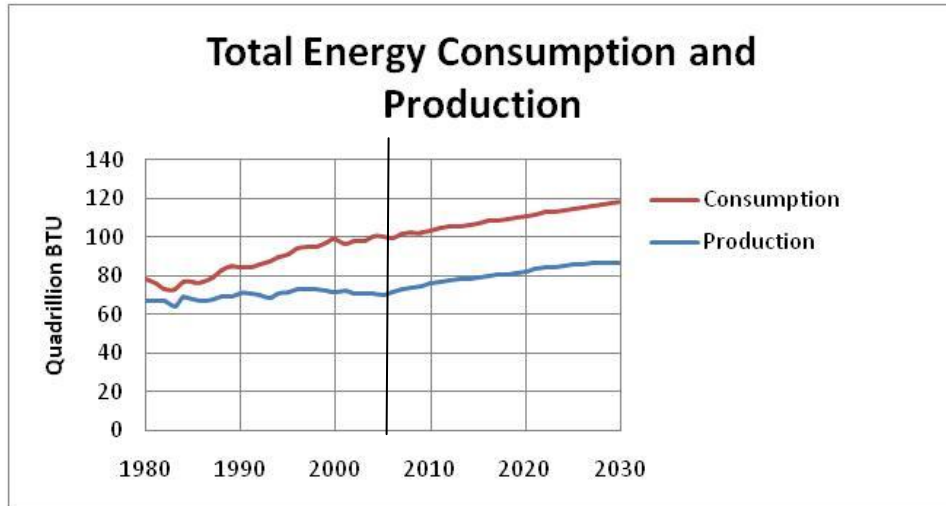


Figure 1.2: Total Energy Consumption in US in quadrillion Btu (2006) (5). The US consumes more energy than it produces and is dependent on energy imports.

An important aspect of energy consumption is the type of fuel utilized and its impact on the environment. As Figure 1.3 below shows, the highest energy consumptions come from polluting fuels such as coal, natural gas and liquid fuels (Oil and other petroleum products). It is interesting to note that renewable energies excluding hydro power are projected to represent a bigger part of energy consumption, reflecting increased awareness of recent climate change concerns and high volatility in fossil fuels prices. However, they are still projected to be relatively small percentage of the energy mix, primarily due to their elevated cost.

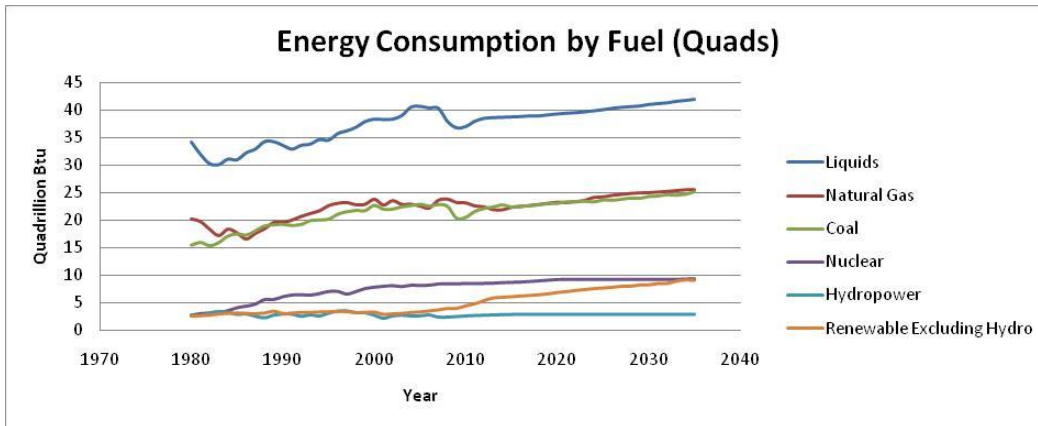


Figure 1.3: Energy Consumption by Fuel (Quadrillion BTU) (5).

The high energy demand generated by an increase in population and economic development around the world, is pushing the current energy supply infrastructure to its limits. Spiking oil prices in summer 2008 have shown that the world's supply of oil was being stretched to its limits, further justifying the integration of more renewable energy in the US energy supply.

1.2.Solar Energy

1.2.1. Resource Assessment:

One can easily appreciate the abundance of solar energy through its daily flooding of the surface of the earth and its ability to sustain life on this planet. On a clear day, the surface of the earth can receive up to 1050 W/m^2 , enough energy to power a microwave oven. The solar energy reaching the entire surface of the earth in one year is approximately 3.3×10^6 Exajoules, which is more than 6000 times the projected global energy consumption. In the US alone, more than 40,000 EJ of solar energy is available per year, which is over 400 times the total primary energy consumed during 2002 (2). The cost and technology necessary in harnessing this energy have been the two most significant barriers in exploiting this source of energy.

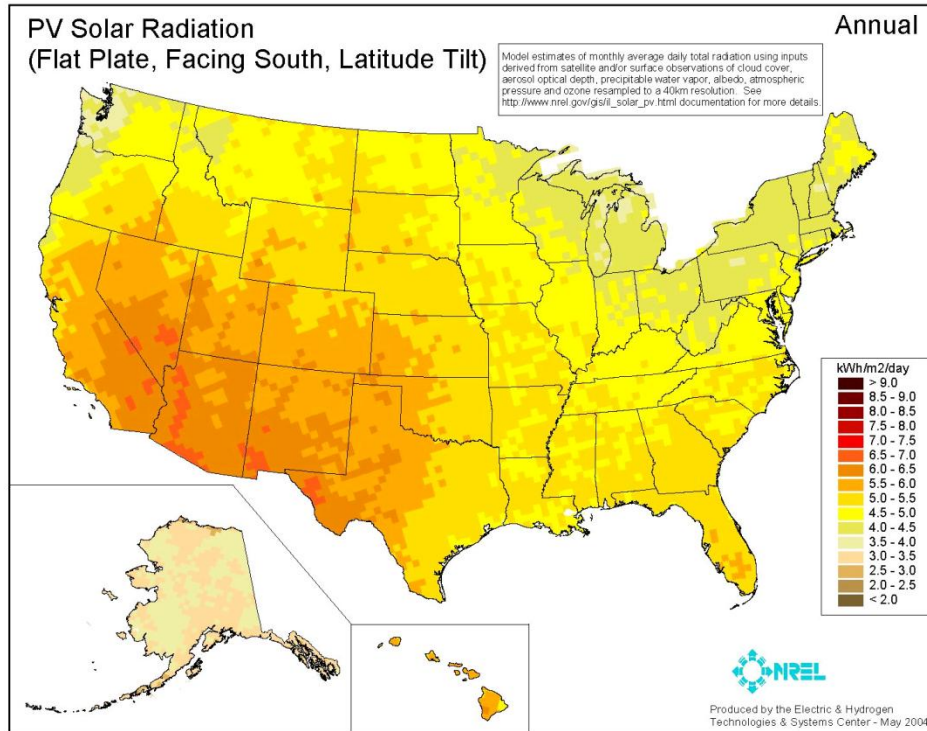


Figure 1.4: PV solar radiation map in US (6)

Figure 1.4 above, shows the average annual insolation (solar radiation) in the US. A significant percentage on US main land receives about 5 KWh/m²/day. Areas with the highest solar radiations are uninhabited, arid and desertic regions, making it suitable for the deployment of PV which requires vast land usage due to the poor energy density of the resource. Although these location are somewhat remote from population centers, energy can be transmitted through large transmission infrastructure.

1.2.2. Market history for PV

Discovered in the mid-1800's the photoelectric effect in semiconductor materials is the basis of solar photovoltaic technology where solar energy is directly converted to electrical energy. The first PV devices did not happen until the 1960 when the US and Russian space programs motivated the development of the technology. Early PV cells were constructed of crystalline Silicon and cost more than \$250/W, a figure not suitable for terrestrial applications. In the 1970's, as manufacturing technology and experience expanded, the first terrestrial application of PV started to appear in devices such as calculators, watches and remote communication systems. Following, the first oil shock of 1973, small scale PV power generation application (around 100 kW or less) started appearing and has been

increasing steadily since at a rate of 15-20% per year for the last 25 years (2). In 2002, an entire PV system including crystalline silicon modules, inverters, battery storage system and other power conditioning equipment could range from \$600-\$900/m² of collection area (installation included)

Experience curve for PV modules

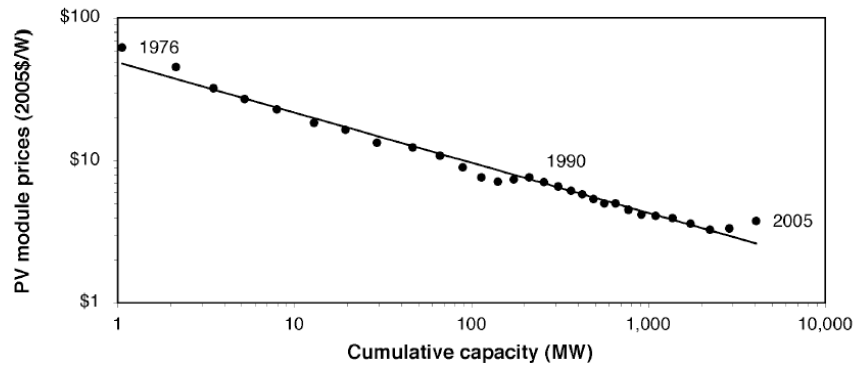


Figure 1.5: Experience Curve for PV module cost (1976-2005) (source IEA)(7). The cost of PV modules has been steadily decreasing with cumulative capacity.

As PV technology continues to develop and manufacturing techniques continue to be improved the price of PV technology keeps decreasing as shown in Figure 1.5 above and Figure 1.6 below. At about 1 \$/Wp, PV is expected to be competitive with electricity generation from fossil fuels. As Figure 1.5 above shows, the cost of a PV module has been decreasing from about \$60/W in 1976 to about \$2.70/Wp in 2005. In February 2010, module prices are as low as \$2.00 / Wp according to Photon International Magazine.

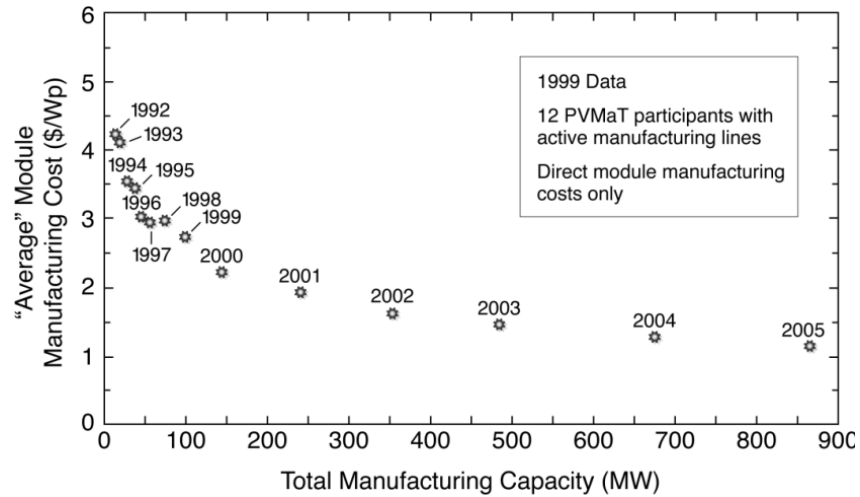


Figure 1.6: PV module cost (8)

1.3. Multi-crystalline Photovoltaic Cells

Our research work focuses on improving the efficiency of multi-crystalline solar cells. Since cast multi-silicon is a cheaper substrate than single crystalline silicon, it offers a greater promise for cell cost reduction. As can be seen in Figure 1.7, multi-crystalline cell efficiency has been constantly increasing for the past two decades although it is lower than single crystalline cell efficiency. The goal of the research work undertaken is to bring multi-crystalline cell efficiency closer to single crystal efficiency while taking advantage of its lower cost. Multiple research directions can be explored, however in this work we only focus on increasing the light trapping capability of multi-crystalline solar cells through the fabrication of light trapping texture.

Best Research-Cell Efficiencies

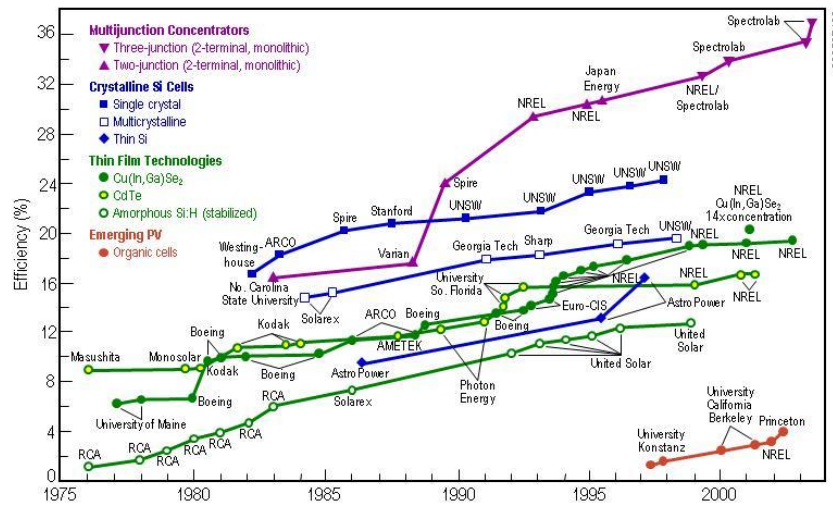


Figure 1.7: Solar cell efficiency increase (9).

1.4. Surface patterning methods:

There are many ways to improve the efficiency of solar cells, among them surface texturing is an attractive method to reduce surface reflection and improve light-trapping capabilities of a silicon solar cell. Different surface texturing methods have been developed but they all follow the same guiding principal of patterning the cell to provide surfaces enabling more reflection of incident sun light into the semiconductor material itself. Figure 1.8 below shows diagrams portraying the difference in reflectivity between a flat surface and one textured with pyramidal-shaped features. In the first case, incident light is partially reflected off of the flat surface and is lost to the atmosphere instead of being absorbed by the substrate. However in the second case, the pyramidal features offer reflective surfaces allowing the incident light to be reflected towards the substrate thus offering it an additional opportunity to be absorbed by the substrate and be converted to electrical energy.

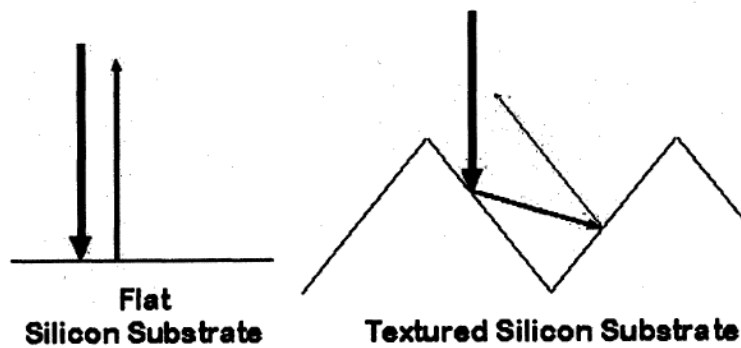


Figure 1.8: Incident light on a flat substrate is reflected back to the atmosphere and never enters the Silicon. A textured cell provides reflective surfaces directing the reflected light into the material itself. (10)

Another advantage presented by surface texturing is the lengthening of the path traveled by a ray of light inside a cell. Light penetrating the substrate is not systematically absorbed and converted to electrical energy, it can travel within it and be reflected out of it without being absorbed. When the path of light traveling within the substrate is lengthened, it increases the probability that light would be absorbed by the substrate. Figure 1.9 shows how surface texturing acts on lengthening the path of light travel by providing a surface inclined in direction making it difficult for light to escape the substrate as light can only escape at angles lower than the critical angle of total internal reflection.

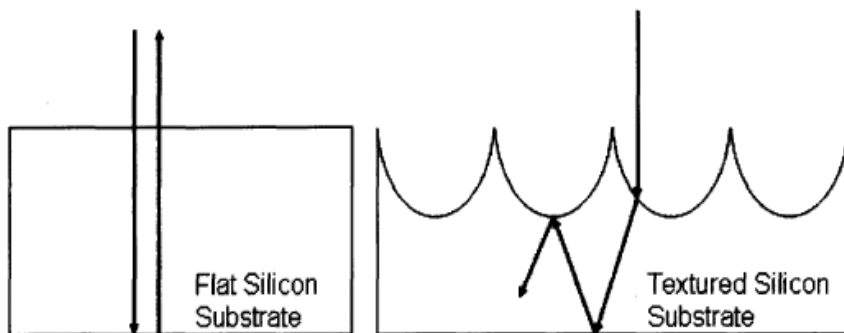


Figure 1.9: Light path lengthening due to surface texturing. When light rays enter a silicon substrate, they travel until they are absorbed by the silicon. If rays take a longer path within the silicon, they have a greater chance of being absorbed. A textured silicon substrate helps trap rays better, by providing inclined surfaces which make it harder for a ray to strike at an angle less than the critical angle (10)

1.4.1 Random pyramids:

Nowadays, “upright random pyramids are the most popular texture in [...] single-crystalline silicon photovoltaics, and the process usually adopts the high efficiency and cost-effectiveness alkaline etching.” (11) The texturing process consists of using an alkaline etch (e.g. KOH) to etch a collection of randomly placed pyramids with a given size distribution (11). Alkaline etches have a convenient directionality due to etch rates differences between the different Silicon crystal planes $\{111\}$, $\{110\}$ and $\{100\}$ resulting in anisotropic etching processes. In 100-Silicon, a KOH solution etches preferably in the 100 direction and slower in the 111 direction, therefore resulting in surfaces that are typically inclined in a 54.7 degree angle from the horizontal which enhance the absorption of incident light into the substrate as shown in Figure 1.8.

The process of formation of these random pyramids has many hypotheses. The most prevalent of them is one where the hydrogen bubbles formed in the etching reaction would cause micro-masking locations, randomly distributed in location and size, that would lead to the formation of the pyramids as described above (12). This method would explain the different sizes of pyramids encountered and their random distribution.

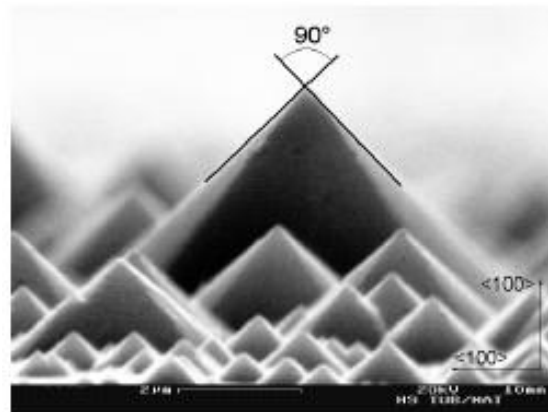


Figure 1.10: SEM micrograph of Random Pyramids Fabricated Using KOH Etch (12)

1.4.2 Texturing of multi-Si:

As pyramidal structures are conveniently etched in single crystalline Silicon due to the predictable alkaline etch behavior on the crystallographic planes, the same cannot be said for multi-crystalline Silicon. The random orientation of the grains in the substrate make it very difficult to use

anisotropic etches (or etches that are more selective in some crystallographic planes than others) since the resulting features will have a non-uniformity that follows grain structure. Other methods, less sensitive to grain orientation, must be employed. Among the most common of them are Reactive Ion Etching (RIE) and isotropic wet acidic etching (13).

RIE consists of a plasma etching of Silicon using SF_6 and O_2 as typical etching species. Its main advantage is the ability to etch high aspect ratio features independently of the crystal orientation of the grains being etched through the use of a bias voltage that accelerates the etching species. Thus, the direction of the etching process can be influenced to become anisotropic without being dependent on the crystallographic structure of the silicon substrate (14). This process requires expensive equipment that employ high vacuum processes alternated with slow etching processing making the viability of RIE in industrial mass production of solar cells a questionable process (15). An RIE process combined with additional microwave plasma using microwave downstream etching allows the tuning of the degree of isotropy of the etch and results in ellipsoidal features known to have low reflectance (12%) as shown in Figure 1.11.

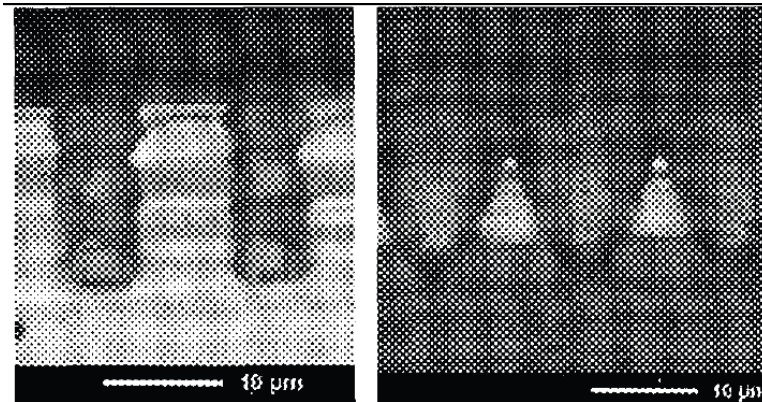


Figure 1.11: Microwave Enhanced RIE resulting in ellipsoidal features with low reflectance.(14)

A cheaper and faster method of surface texturing of multi-crystalline silicon consists of using acidic wet etching to achieve features that enhance light trapping. Wet acidic texturing performed with solutions containing $\text{HF-HNO}_3\text{-H}_2\text{O}$ and HF-HNO_3 , which have a tendency to etch isotropically, can result in features with rounded surfaces rather than flat-sided as is the case with anisotropic etching. These curved surfaces can have advantageous anti-reflective properties (15). A simple etching of multi-

crystalline silicon wafer in an HF-HNO₃-H₂O etch followed by a HF-HNO₃ etch results in the texture showed in Figure 1.12. These features significantly lower the reflectivity of the surface of the substrate and enhance light trapping.

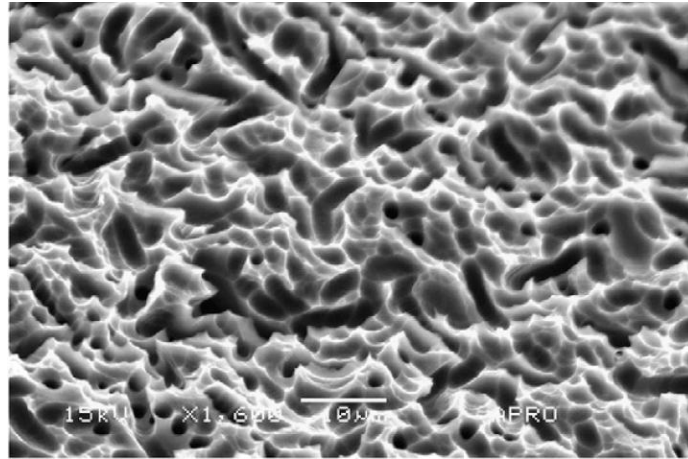


Figure 1.12: Isotropic texturing of multi-crystalline Silicon using acidic etching(15). Acidic etching methods are used on the surface of multi-crystalline silicon to generate randomly etched feature which increase the light trapping ability of the cell.

However, texturing the surface of a solar cell using isotropic etching methods can present some disadvantages. First, the isotropic process is difficult to control due to the sensitivity of etch rates to the thermal gradients and species concentrations in the etch bath. Since the overall etching reaction is exothermic, the knowledge of the temperature profile is critical to controlling the etching process and scaling it to industrial applications. Also, as the reaction products impact the concentration of reactant species as well as the reaction mechanisms, the chemical composition of the bath must be constantly monitored and retuned in order to maintain proper control over the etching process. Additionally, the chemical composition of the etch bath must also be adapted to different incoming wafers as they have different saw damage characteristics. Finally, although the resulting texture on the surface of the cell has favorable light trapping ability, it however increases the surface area of the cell and attacks its grain boundaries, which increases the recombination effect at the surface of the cell thus undermining its performance.

Chapter 2 - This work's approach

The work involved in this thesis contributes to the goal of developing industrial processes for light trapping features in the surface of multi-crystalline silicon photovoltaic cells. As a commercially viable and low-cost option, acidic wet etching is the selected process for developing the desired features that Professor Emanuel Sachs and Dr. James Brecht have designed (16) which consists of grooves or trenches of parabolic cross-section that enable lower incident light reflectivity as well as facilitates other processing steps.

2.1 Theoretical Determination of Ideal Cross-section Shape

According to previous work done on modeling the optimal cross-sectional shape of the desired light trapping features, multiple trench shapes have been tested to determine the optimal one. The different shapes of parabolas tested are shown in Figure 2.1. They range from aspect ratio of 0.25 to 2 and have constant width. Using Zemax ray tracing software, it was determined that light trapping ability increases with aspect ratio. It appears, that at a parabola with an aspect ratio of 1.0, the light trapping begins to plateau, thus making any higher aspect ratio features only insignificantly advantageous Figure 2.2 (10). Given the difficulty of achieving high aspect ratio feature using wet etching, reaching features of aspect ratio of 1 would be ideal in this case.

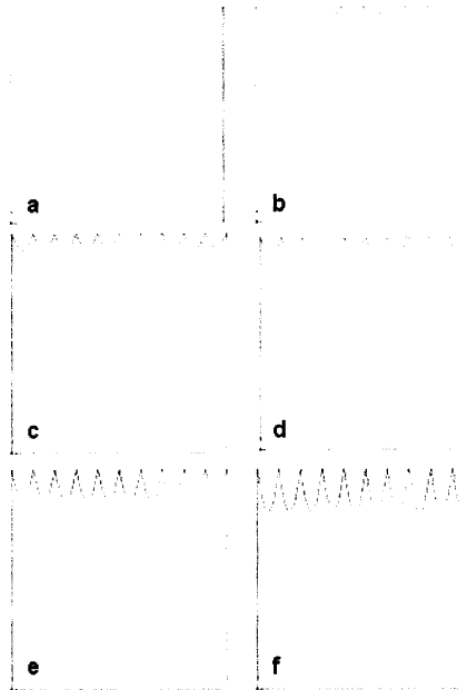


Figure 2.1: Cross-section of each parabola that was tested a) 1/4 aspect ratio parabola, b) 1/2 aspect ratio parabola, c) 3/4 aspect ratio parabola, d) 1 aspect ratio parabola, e) 1.5 aspect ratio and f) 2 aspect ratio parabola (10)

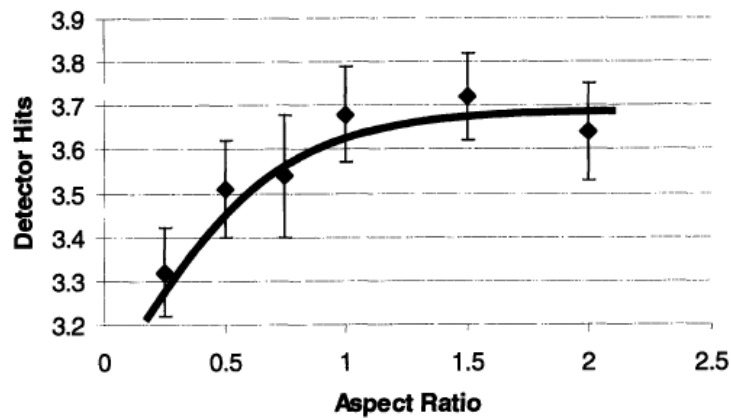


Figure 2.2: Graph of the number of detector hits versus the aspect ratio of the parabola. The optimum Parabola has a unit aspect ratio (10)

In conclusion, it was previously determined that the ideal cross-section shape for the desired light trapping features is a parabola with aspect ratio of unity. Achieving such a shape in multi-crystalline silicon excludes the use of anisotropic wet etching methods given the random disposition of grain

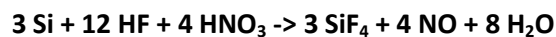
orientation in the substrate. Reactive Ion Etching (RIE) methods are too slow of the desired scalability of the manufacturing process we aspire to achieve. We are therefore left with isotropic wet etching methods controlled for a desired anisotropy as the ideal method for achieving a parabola of aspect ratio of 1.

2.2 Isotropic etching with high Aspect Ratio

Isotropic etching is typically conducted using a mixture of hydrofluoric acid (HF) and nitric acid (HNO₃) diluted in water or acetic acid (HC₂H₃O₂). The etching process in this system has been determined to be a multiple reaction process influenced by the chemical species concentration, mass transfer effects and thermal effects. The HF-HNO₃-H₂O and HF-HNO₃-HC₂H₃O₂ systems have been extensively studied by Robbins and Schwartz, who have determined etch rates and various rate limiting factors for a range of chemical species concentrations(17)(18)

2.2.1 The H-N-A etching system:

A mixture of hydrofluoric, nitric and acetic acids (HNA) is the choice combination for this research work. HF and HNO₃ dilution in HC₂H₃O₂ has more tolerance for the diluent concentration than the water diluted system (18), it is therefore more favorable for an industrial process. Robbins and Schwartz have assumed the overall etching reaction to be (17):



Others, such as Kulkarni and Shimura (19)(20), view the global reaction guiding the etching of Silicon in the HNA system as a two step reaction: oxidation and dissolution (19).

The oxidation step is guided by the following reaction:



While the dissolution step follows:



Also, other forms of the oxidation and dissolution reactions have been reported (21) ,



As can be noticed in the above reaction equations, SiO_2 is a product of the oxidation step and is formed on the surface of the silicon substrate. It is then removed from the substrate in the second reaction where HF is a reactant. As this dissolution reaction reaches steady state, its products ($\text{H}_2\text{SiF}_6 + 2\text{H}_2\text{O}$) accumulate near the surface of the substrates, yielding a diffusion barrier for HF to reach the SiO_2 on the surface of the substrate. The chemical species NO_2 , also a product of the oxidation reaction is considered by Robbins and Schwartz as a potential autocatalytic species which modifies the diffusion limited supply of reagent to the silicon surface. Additionally, H_2SiF_6 is also viewed as a reaction product that influences the morphology of the substrate during the reaction. Weinreich (22) discusses how H_2SiF_6 was found to be a source of anisotropy in the HNA system and therefore contributes to the dynamics of the global reaction. In all, one of the most important factors in this reaction is the formation of a diffusion boundary layer that acts as a diffusion barrier to reactants. The etch rates are therefore diffusion controlled (17), although they can also be influenced by the agitation of the etching bath.

This work focuses on taking advantage of the existence of this diffusion barrier layer in order to physically influence the isotropic etching process to etch preferentially in the vertical direction in the goal of achieving features with parabolic cross-sectional shape of aspect ratio of 1.

2.2.2 Boundary layer removal

In order to achieve high aspect ratio features in silicon, it is necessary to create an etch rate increase in the vertical direction relative to the horizontal direction. One way to achieve this goal is to remove or reduce the thickness of the diffusion boundary layer existing at the surface of the silicon during isotropic etching. The product of the dissolution reaction creates a diffusion barrier to the reactants, slowing their diffusion to the surface of the substrate for reaction. Removing or reducing the diffusion layer thickness selectively can cause an acceleration of the etch rate at that location which

would lead to directionally controlled etching when the removal of the boundary layer is properly controlled.

The illustration in Figure 2.3 shows how the products of the first reaction (i.e. the oxidation reaction) build up near the surface of the substrate and constitute a barrier for the reactant of the dissolution reaction in etching away the silicon dioxide from the surface of the substrate. As Schwartz and Robbins discuss, the reaction rate is significantly dependent on the presence of this diffusion barrier combined with a postulate that the heat of reaction sets up a thermal gradient near the surface of the substrate causing the diffusion coefficient to become a function of the distance from the reaction surface(17). This indicates that reducing the thickness of the diffusion barrier will enhance the reaction rate locally since the diffusion distance would be smaller and the diffusion coefficient would be greater. Figure 2.4 is a depiction of a diffusion barrier with locally reduced thickness in the bottom of the trench. As described above, a thinner diffusion barrier allows for a small diffusion distance between the reactants and the surface of the substrate while increasing the diffusion coefficient due to the heat of reaction. This indicates that the etch rate should increase in the region of thin diffusion barrier which would lead to the desired result of preferential (or directional) etching.

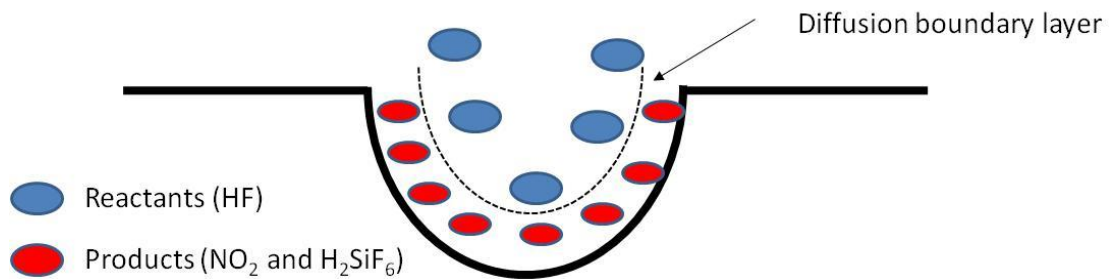


Figure 2.3: Diffusion Barrier: the reactants for the dissolution reaction are limited by the presence of the products of the oxidation reaction which creates a diffusion barrier

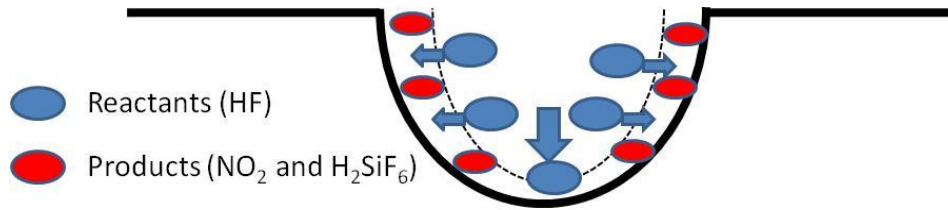


Figure 2.4: Diffusion Barrier preferentially reduced to enable faster etching in the vertical direction

In addition to the diffusion barrier that affects the reaction rates, fluid boundary layers can also play a role in the reaction especially because etching baths are often agitated. As the etching fluid passes above the surface of the substrate, a fluid boundary layer takes place. Fluid trapped between the surface and the boundary layer has a velocity near zero, which indicates that etchant from outside the boundary layer has to diffuse across the boundary layer first then through the diffusion barrier then reach the surface.

Since the thickness of the boundary layer is a function of the fluid velocity as described by the equation below, one can reduce the thickness of the boundary layer by increasing the fluid velocity around it as Figure 2.5 shows. Furthermore, at the start of the fluid boundary layer, its thickness is smallest, which indicates the smallest diffusion distance for reactants. Additionally, this small boundary layer thickness would be complemented by a diffusion layer thickness contained within the fluid boundary layer, thus we can reduce the thickness of the diffusion layer by reducing the thickness of the associated fluid boundary layer. This leads to the conclusion that it is highly favorable to seek the point of thinnest fluid boundary layer or significantly reduce its thickness at the location that we seek to etch at a higher rate. This indicates that we should research methods of mechanically interfering with the etch batch to break the fluid boundary layer and the diffusion layer.

$$\delta = \frac{5.0}{U_{\infty}/\nu x} = \frac{5x}{\sqrt{Re_x}}$$

The equation above (23) describes the boundary layer thickness (δ) for a moving fluid over a flat plate. U_{∞} is the bulk fluid velocity away from the surface, ν is its dynamic viscosity, x is the distance from the edge of the flat plate and Re_x is the Reynolds number in the x -direction. We use this relationship to

evaluate the order of magnitude of fluid boundary layer thickness that would take place in our experiments. Knowing that feature size in our experiments is in the order of $10\ \mu\text{m}$, we plot the fluid boundary layer thickness as a function of distance as seen in Figure 2.5.

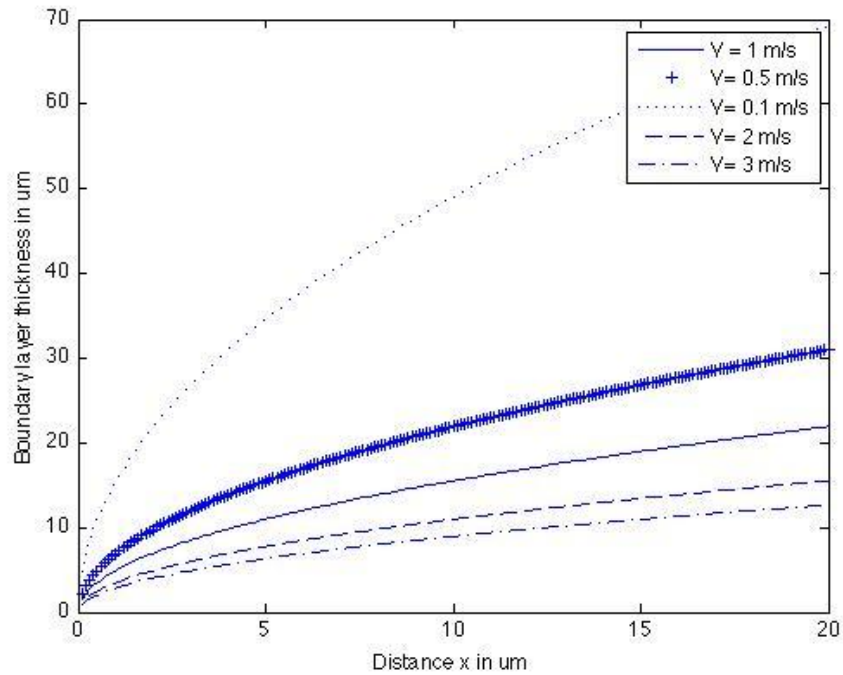


Figure 2.5: Fluid Boundary Layer Thickness: As fluid velocity increases, the thickness decreases and the start of the boundary layer has the smallest thickness.

We observe the expected trend of boundary layer thickness decreasing as the fluid velocity increases. However, we note that for feature sizes in the order of $10\ \mu\text{m}$ fluid velocities have to be at least $2\ \text{m/s}$ for the boundary layer thickness to be smaller than the feature size. This indicates that if hydrodynamic methods are used in our goal of high aspect ratio etching, they would have to involve fluid velocities of $2\ \text{m/s}$ or higher.

We conclude that in order to locally increase the etching rate of an agitated HNA system, we must remove or reduce the thickness of the fluid boundary layer associated with the etching fluid velocity. One way to verify this hypothesis is to conduct an experiment where the fluid boundary layer is mechanically removed or reduced and observe its effect on etch rates.

2.3 Magnetic particle etching

In order to test our hypothesis that removing or reducing the diffusion layer between reactants of the dissolution reaction and products of the oxidation reaction would result in faster etching rates, we devised the following experiment. A steel spherical particle of diameter between 20 to 100 μm is deposited on the surface of the sample to be etched. Then we bring a magnet to close proximity to the bottom of container which is holding the sample such that the distance between the steel particle and the magnet is in the range of 2 to 4 mm. We then actuate the magnet such that it moves following a circular path of diameter of about 1 cm. The concept behind using magnetic particles in motion in an isotropic etching bath is to locally remove the diffusion barrier thus enabling reactants to reach the surface of the silicon. As depicted in Figure 2.6, oxidation reaction products, shown as red elliptical icons, gather at the surface of the sample consequently obstructing the reactants of the dissolution reaction depicted as blue icons. Now, as the steel particle moves on the surface of the sample, it causes a rupture of the diffusion barrier allowing fresh etchant to access the surface of the sample. Since the point where the particle is in contact with the sample represents the location where the diffusion barrier is nil, then the location trailing the magnetic particle is the smallest thickness of a new diffusion barrier arising from continued etching.

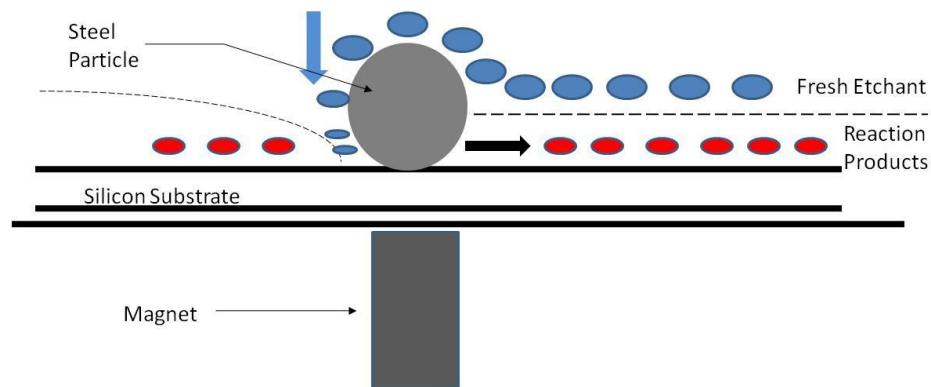


Figure 2.6: Magnetic Etching Theory. As the steel particle brushes the surface of the sample it breaks the diffusion barrier, allowing fresh etchant to enter in contact with the surface of the sample.

The magnet is placed on a rod which is coupled with the shaft of a motor as shown in Figure 2.7. A rotational velocity of 4 revolutions per second is the chosen speed for this experiment. The magnet is

brought in very close proximity with the sample holder, resulting in the very short distance between the particle and the magnet.

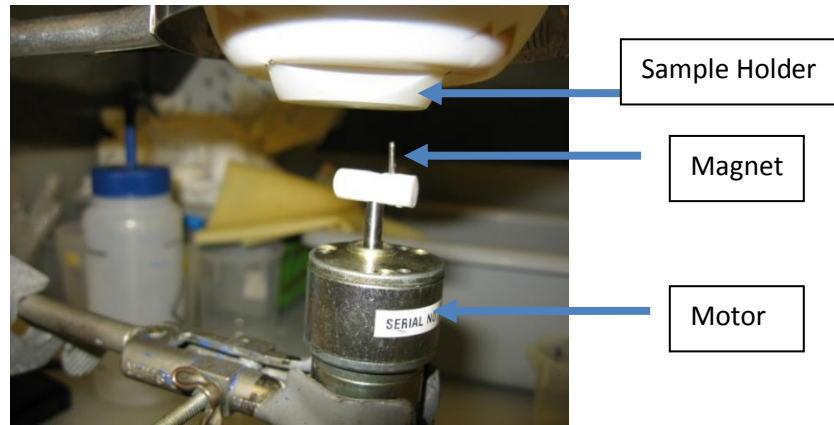


Figure 2.7: Magnetic Etching Apparatus

After running an experiment for 3 min and using the HNA etchant 6:1:1¹ we obtained the result shown in Figure 2.8. We can distinguish with the naked eye the features caused by the magnetic particles' circular path. This indicates that an etch rate difference occurs at the location where the particle are in contact with the sample. To further analyze the shape of the resulting feature, we scan the surface of this sample on a contact tip profilometer to better quantify the effect of the particle motion. The profilometer data is shown in Figure 2.9

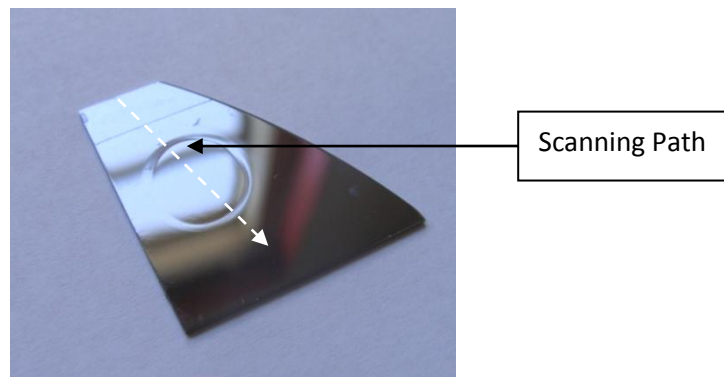


Figure 2.8: Magnetic Etching Sample. The etching pattern of the steel particle's motion on the surface of the sample is shown as the circular pattern on this picture.

¹ We used 6:1:1 since it was recognized at the time as the etchant with the highest degree of isotropy.

As can be seen in the figure below, locations where the magnetic particle interacted with the surface of the sample show greater etch rates than any other location on the sample. We can determine from the profilometer data that the etch depth in these locations is about 6.5 μm . We can compare this value to the etch step showing the distance between a masked surface in the sample and its etched surface. This etch step depth is about 3 μm . This leads to the conclusion that areas in contact with the particle are etched 2.15 times faster than areas away from it.

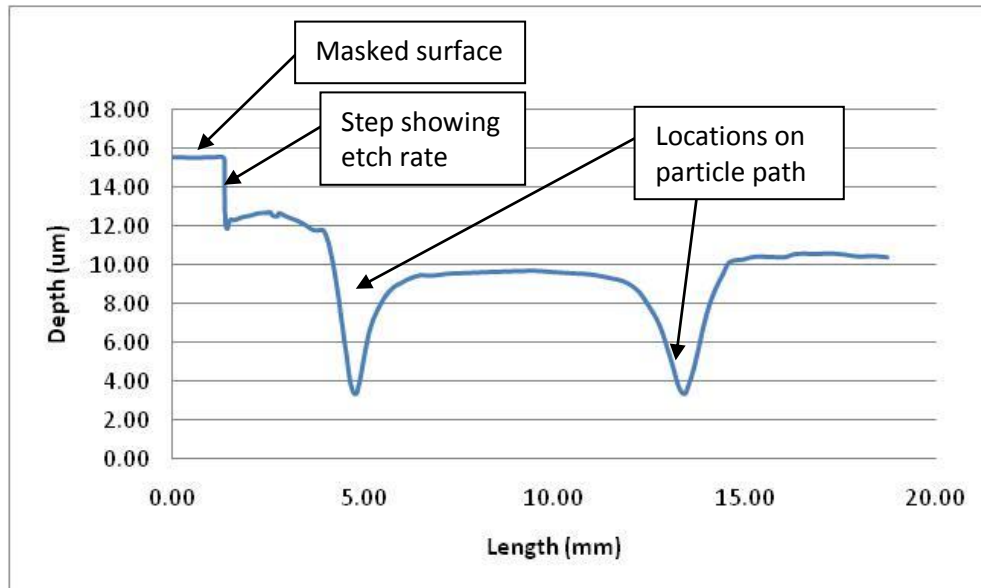


Figure 2.9: Trench Profile - Profilometer Data

Considering that the chosen particle material does not have a catalytic effect on the reaction, we can deduce that the motion of the particle on the surface of the sample has caused a mechanical effect that is favorable to localized preferential etching.

In conclusion, we can state that magnetic particle etching does locally increase the etch rate in the vicinity of the particle paths, by acting as a brush on the surface of the sample. This shows that the removal of the diffusion boundary layer and the fluid dynamics resulting from a moving particle on the surface of the sample do indeed increase the local etch rate in a desirable direction. However in this case, we were not able to achieve a significant difference between vertical and horizontal etch rates in the areas where the particles were moving. The resulting aspect ratios in this experiment are in the order of 0.005. These low aspect ratios are due to the fact that the magnetic particle did not follow a narrow circular path but was rather contained between two concentric circular bounds defined by the

diameter of the magnet used². Additional experiments were conducted using a magnet that was machined down to a smaller diameter but they did not yield better results. Clearly, the aspect ratios are not high enough to reach the desired aspect ratio of 1.

Therefore, magnetic etching confirms the hypothesis that removing or reducing the diffusion layer will increase the etching rate. However this particular method is not well suited for etching the desired trenches since it yields very low aspect ratios. Additionally, we observed that the particles used were slowly dissolving in the etch chemistry thus leading to modification of their size and a resulting etch chemistry modification. Finally, we note that the particles did not follow the magnet in a narrow path but instead they were swirling as they followed the magnet. We therefore turn to another method for high aspect ratio trench etching: the Jet Etching method.

² The magnet used in this experiment was cylindrical in shape. As the magnetic field is stronger on the edges of the magnet, the particles were attracted to the circumference of the magnet and therefore traced a path similar in width to the diameter of the magnet.

Chapter 3 - Jet Etching

3.1 Jet Etching introduction

Jet etching consists of using the etching fluid under hydrodynamic conditions that generate a local jet effect near the feature we would like to achieve. Jet etching consists in using a mask as orifice and impinging the etchant at relatively high velocity to generate a local jet effect. Using a mask layer on the top of the Si sample, we can force the etchant through its opening. As the fluid etches away through the mask opening and undercuts it, the remaining over hanging mask can act as a local jet opening that would force the etchant towards the bottom of the trench therefore causing a local removal of the diffusion boundary layer at the bottom of the trench primarily. This in turn would cause a local etch rate increase and a directional selectivity in the isotropic etch as depicted in Figure 3.1. Additionally, fresh etchant would be supplied to the bottom of the trench first and would flow out through the sidewalls of the trenches as it depletes. Since etching rates decrease with the depletion of reactants, the resulting effect would be higher etching rates in the bottom of the trench and lower ones in the sidewalls. This further contributes to the directional etching effect that we seek to achieve.

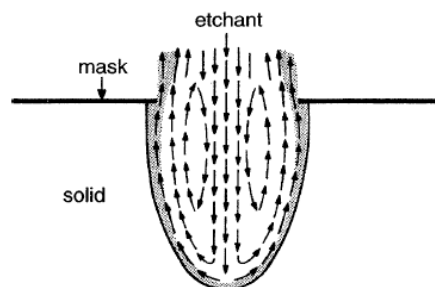


Figure 3.1: Schematic of jet etching process for large trenches.(24) Fresh etchant enters through the mask opening, reaches the bottom of the trench first at higher etch rates then as the etchant is depleted it etches the sidewalls at slower etch rates. This results in high aspect ratio features.

In order to verify this hypothesis, a flow simulation was conducted. The goal of the simulation is to obtain a first order analysis of the behavior of the flow in the geometrical configuration of the

trenches we are hoping to achieve. We investigate the required impinging flow velocity necessary to generate the local jet effect, evaluate the behavior of the flow at the mask opening (orifice) and at the base of the trench. We also evaluate the effect of the impinging jet angle on the local jet effect.

3.2 Jet Etching Simulation

3.2.1 Description of Simulation Method

The fluid simulation was conducted using “FloWorks” which is the computational fluid dynamics modeling software offered by SolidWorks Corp. We first would like to confirm the hypothesis of the presence of a local jet effect by conducting the following simulation. A three dimensional model of the trenches we are attempting to achieve was constructed using SolidWorks. We intentionally design the 3D trenches with a smaller diameter than the final desired result, as a way to evaluate an intermediate stage in the etching process. The final diameter of the desired trench is $D_{\text{final}} = 20 \mu\text{m}$, the simulated 3-D trenches have an intermediate diameter of $D_{\text{intermed}} = 14 \mu\text{m}$. Additionally, the modeled trench have a mask opening of $5 \mu\text{m}$ with a mask thickness of $2 \mu\text{m}$ as seen in Figure 3.3.

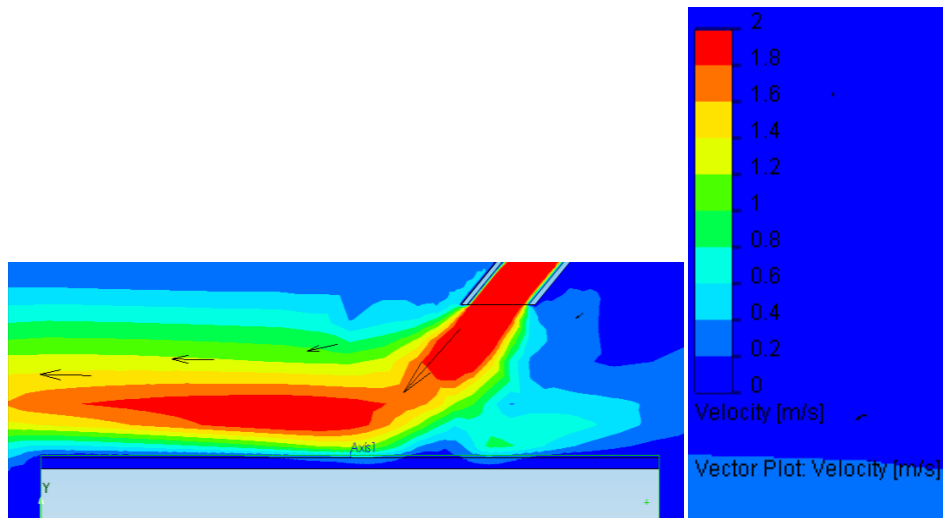


Figure 3.2: CFD simulation - Side View 3m/s , T = 25C. The jetted etchant enters the trench at a velocity of about 0.6m/s indicating the presence of local jet effect at the entrance of the trench.

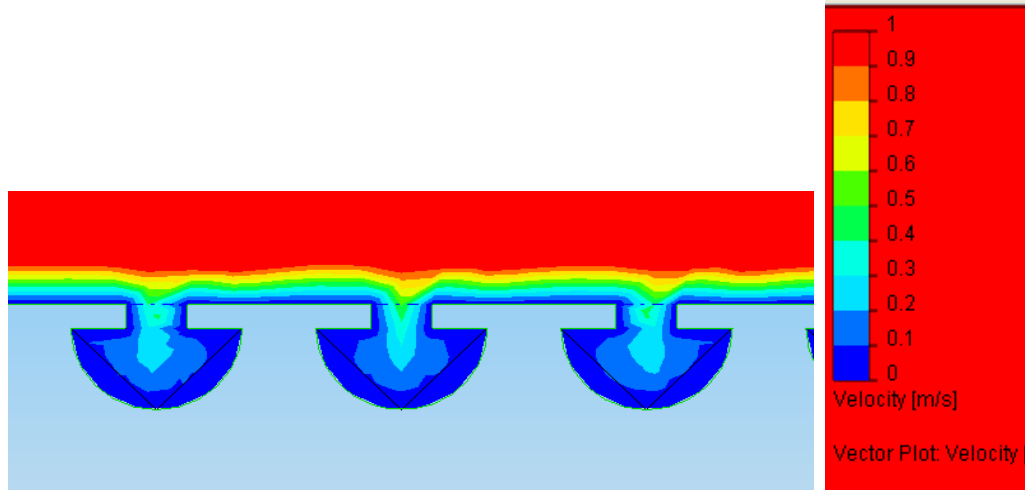


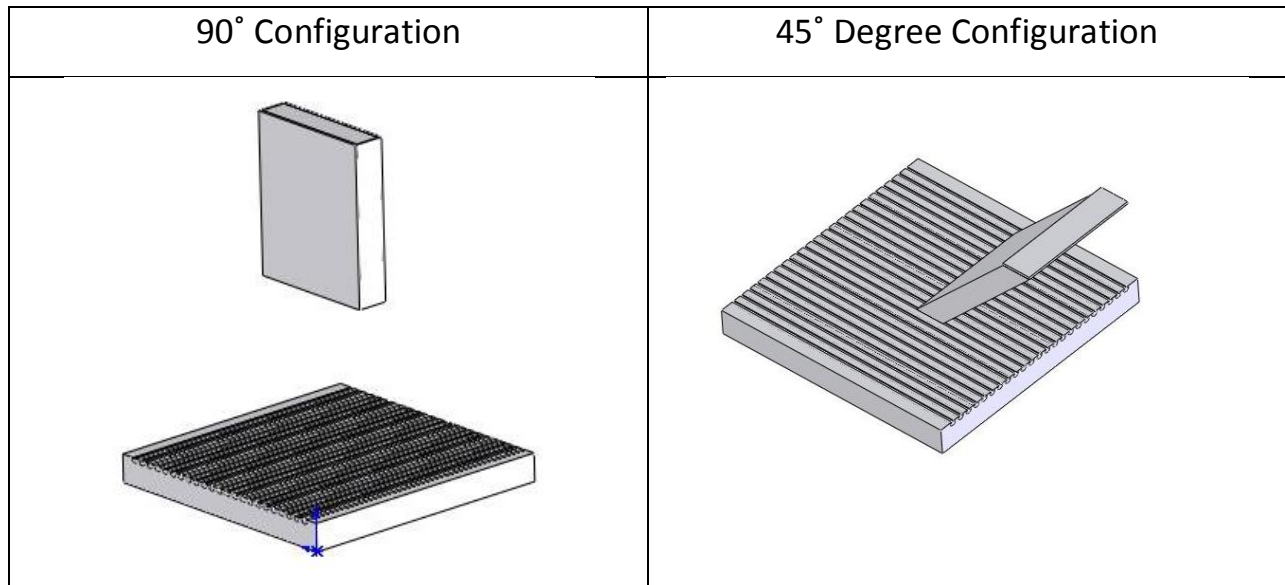
Figure 3.3: CFD simulation 3m/s at T =25 C

The flow source was modeled as a nozzle with rectangular opening ($240 \times 50 \mu\text{m}$) at a distance $H = 100 \mu\text{m}$ from the surface of the sample and inclined 45° as shown in Figure 3.2. The simulated fluid was taken as pure H_2O at $T = 25^\circ\text{C}$. Since the etching solution is mostly aqueous we can assume that its behavior would be similar to an H_2O solution at the same temperature.

Results for a simulation of fluid jetting at 3m/s from the nozzle onto the sample are shown in Figure 3.2 and Figure 3.3 above. Velocity contours show the magnitude of the jet velocity before, during and after entering the trench. The side view illustrated in Figure 3.2, shows that impinging jet velocity is significantly reduced as it approaches the surface of the sample (from 2m/s to about 0.8 m/s) which is depicted by a thin line on top of the bulk of the sample (light blue solid rectangle). We can however notice that the fluid entering the trench does so at a velocity of about 0.6 m/s which indicates the presence of significant fluid flow past the mask opening into the trench. Flow velocities halfway between the top and bottom of the trench reach about 0.3 m/s in the location where the jet is most forcefully impinging. This shows that the jet has the effect of forcing etchant into the trenches. It is important to note that downstream from the location of impingement, flow velocities in the trench are close to 0 m/s. This indicates that a fluid boundary layer exists and has a thickness large enough to include the entire depth of the trench. The effect of this boundary layer is to increase the distance between the reactants and the surface of reaction thus causing slower etch rates downstream from the jet. This also suggests that at the jet location, where fluid is forced into the trench, etch rates would tend to be higher. This finding is corroborated by later experimental results which show that jet etch rates are about 4 times higher than non-jet etch rates.

Additionally, Figure 3.3 shows a cross-section of the fluid flow at the location where the jet most penetrates the trenches. We can observe that in the sidewalls of the trenches flow velocities are low or close to zero, while flow velocities in the center of the trench reach 0.2 to 0.3 m/s. We can also see that at the mask opening there is a constraining of the flow which results in an increase in its velocity. This is more easily observed by the dipping of the velocity contour lines into the mask openings. We can therefore conclude that the jet has the ability to increase fluid flow into the trench and accelerate etch rates by reducing the fluid boundary layer thickness in the trench. However, with the simulation results above, it is difficult to conclude that the local jet effect penetrates to the base of the trench and etches preferentially at that specific location.

In order to further investigate the effect of the jet on the trenches, we conduct a deeper analysis. We simulate two jet impingement angles scenarios 90° and 45° as shown in Figure 3.4



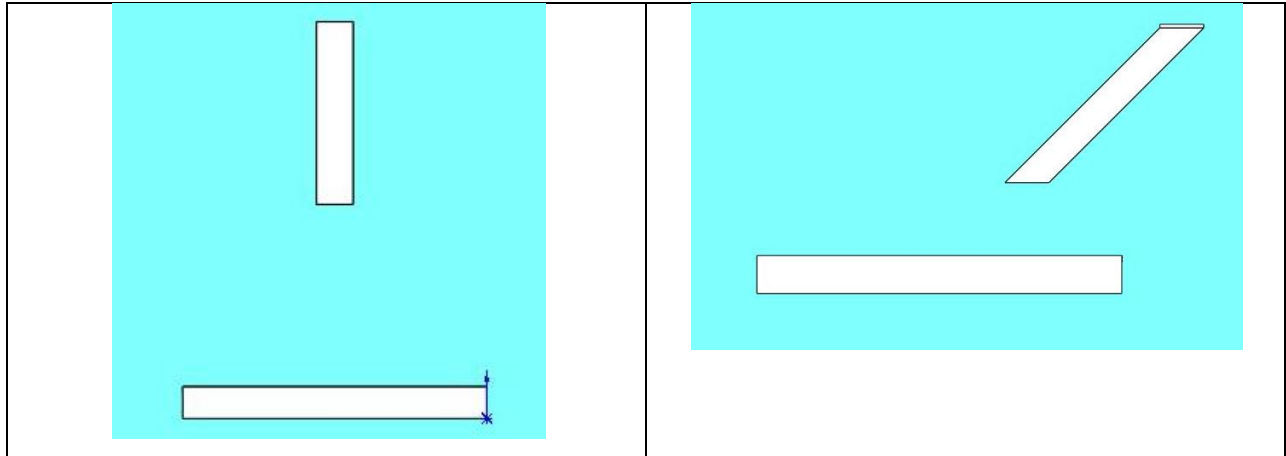


Figure 3.4: 90° and 45° jet impingement angle (SHOW 3-D for 90 and 45 deg)

3.2.2 Jet Velocity

We perform simulations in the goal of determining the effect of jet velocity on the local penetration of the jet into the trenches. Three case scenarios were considered: impinging jet velocities of 3, 5 and 10 m/s. The velocity vectors with magnitude equal to the velocities indicated are normal to the surface of the jet nozzle. Furthermore, particle trajectories (streamlines) were traced in order to observe more clearly the penetration behavior of the jet. We consider each velocity simulation for three different trench openings with diameters $D_{\text{initial}} = 10 \mu\text{m}$, $D_{\text{intermed}} = 14 \mu\text{m}$ and $D_{\text{final}} = 20 \mu\text{m}$. This allows for a better observation of the jet behavior as the trenches are etched open to their final diameter of $D_{\text{final}} = 20 \mu\text{m}$. Finally, we run simulations for two different jet impingement angles: 90° and 45°.

Jet Velocity = 3 m/s , Angle 90°		
D = 10 μm	D = 14 μm	D = 20 μm

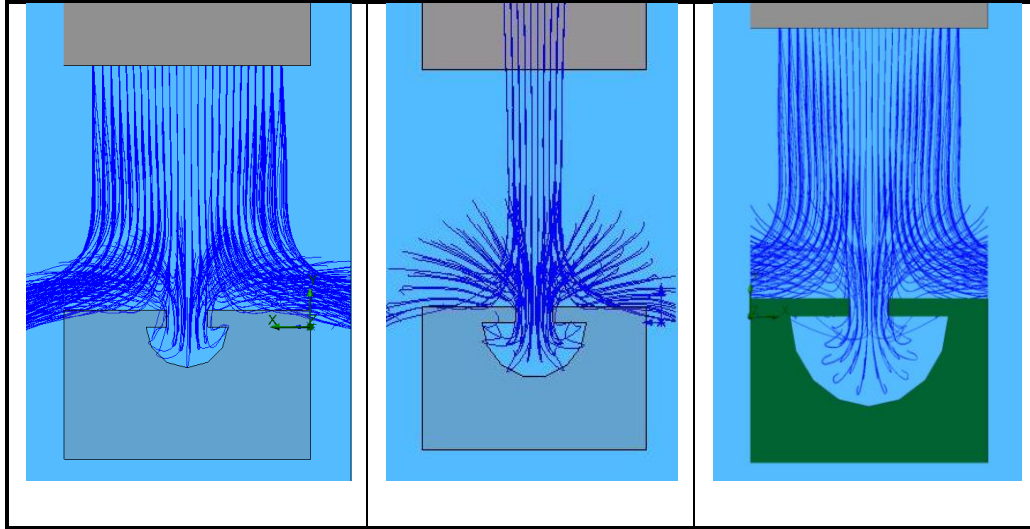


Figure 3.5: Jet velocity simulation results - 3m/s (Cross-section view). As the trenches cross-section widens the jet is less capable of reaching the bottom of the trench.

Figure 3.5 and Figure 3.6 show the trajectory of particles as they leave the jet nozzle and penetrate the trenches. First we can observe that the jet is successful at penetrating the trenches. This is represented by the blue trajectory lines reaching below the opening of the mask. We further notice the constraining of streamlines at the mask opening indicating a jetting effect that results in a relatively high speed flow at the mask opening which allows the etching fluid to enter deeper into the trench.

Second, we can see that as the trenches become wider and deeper, the quantity of trajectory lines reaching the base of the trenches decreases significantly. This indicates that a 3m/s jet velocity, the jet has more difficulty reaching the bottom of the trenches as they get deeper. This will in turn weaken the ability of the local jet in reducing the thickness of the fluid boundary layer and the diffusion layer at the surface of the trench's base. In other words, for a fixed impinging jet speed, as trenches get deeper the local jet is less effective in etching preferentially in the vertical direction.

Jet Velocity = 3 m/s, Angle 90°

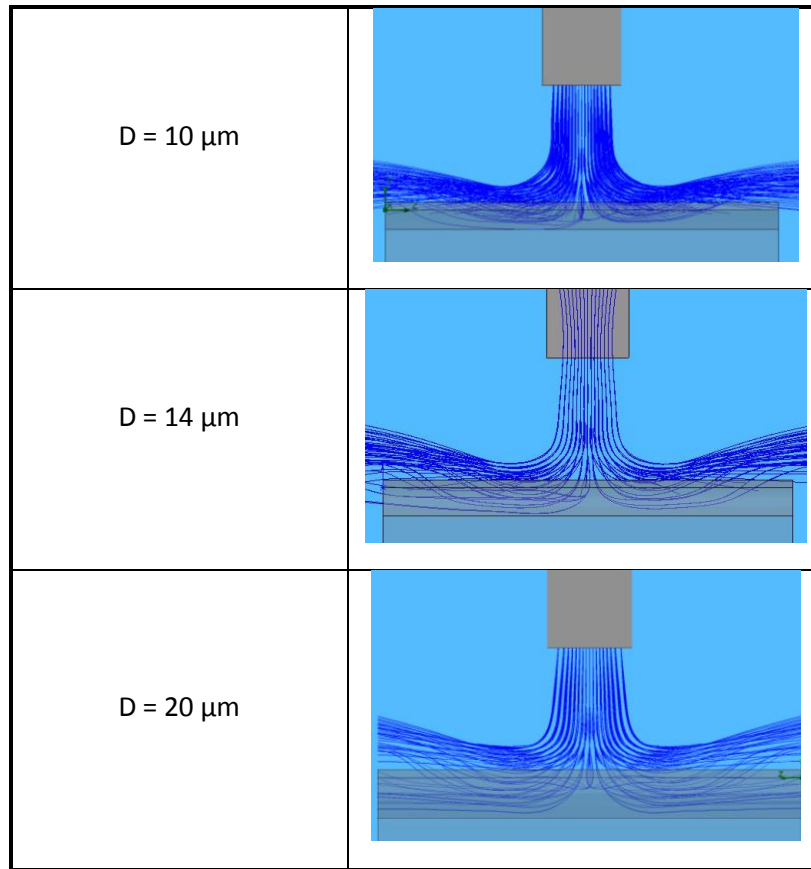


Figure 3.6: Jet velocity simulation results: 3 m/s (side view)

Also, when the trench is in an early opening stage and still has a small diameter ($D_{\text{initial}} = 10$), the particle tracing lines are much closer to the bottom of the trench than the for $D_{\text{intermed}} = 14$ or $D_{\text{final}} = 20 \mu\text{m}$. This suggests that the jet has a stronger effect in the early stages of the etching process and less so as the trench size increases. It is therefore of great importance that the jet etching process starts early in the overall etching process; if the sample is to be inserted in a bath of acid before jetting, this operation must be done quickly to avoid that the acid in the bath etches through the opening before the jet does so.

In addition, as the trenches widen, the trajectory of the traced particles becomes less vertical, indicating that the jet is no longer focused in a downward direction further undermining its ability to etch preferentially in the vertical direction. The diffusion layer at the bottom of the trench would become increasingly more difficult to remove as the trench becomes deeper. This undesirable behavior at 3 m/s could potentially be removed if the jet velocity were increased. The next simulation scenario attempts to answer this question.

Figure 3.7 and Figure 3.8 below show cross-sections and side views of the trenches at different opening diameter for an impinging jet velocity of 5 m/s.

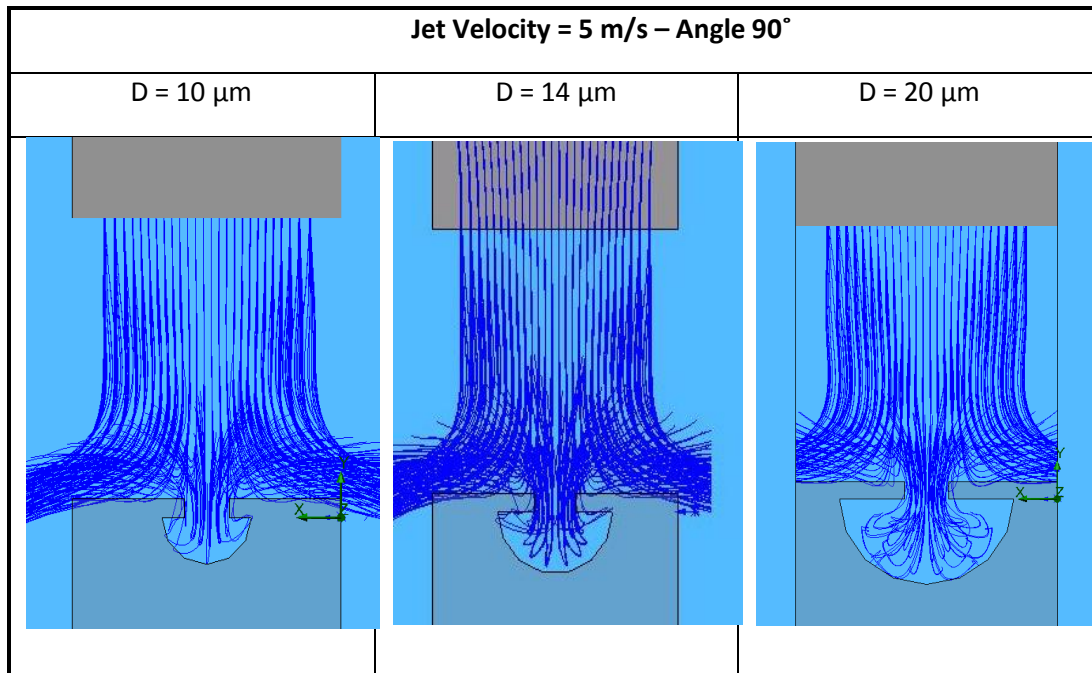


Figure 3.7: Jet velocity simulation results: 5 m/s (cross-section view). At 5 m/s the jet reaches deeper into the trench than at 3m/s even when the trench cross-section is widening.

We can observe that in this case the jet is able to penetrate deeper into the trench as it widens, indicating that a higher jet velocity could result in a better way to break the diffusion barrier at the bottom of the trench thus serving the purpose of higher aspect ratio etching. This behavior is consistent across all diameters. We can also observe that trajectory lines remain more vertical than in the 3 m/s case, which indicates that a higher jet velocity would support the preferential vertical etching process that we seek to achieve. However, as suggested in the 3 m/s case, when the trench widens to its final diameter ($D_{final} = 20 \mu\text{m}$), the trajectory lines become less vertical and get diverted towards the sidewalls of the trench rather than its base. This counter productive behavior indicates that the later stages of jet etching, the effect of the jet is less beneficial than the beginning.

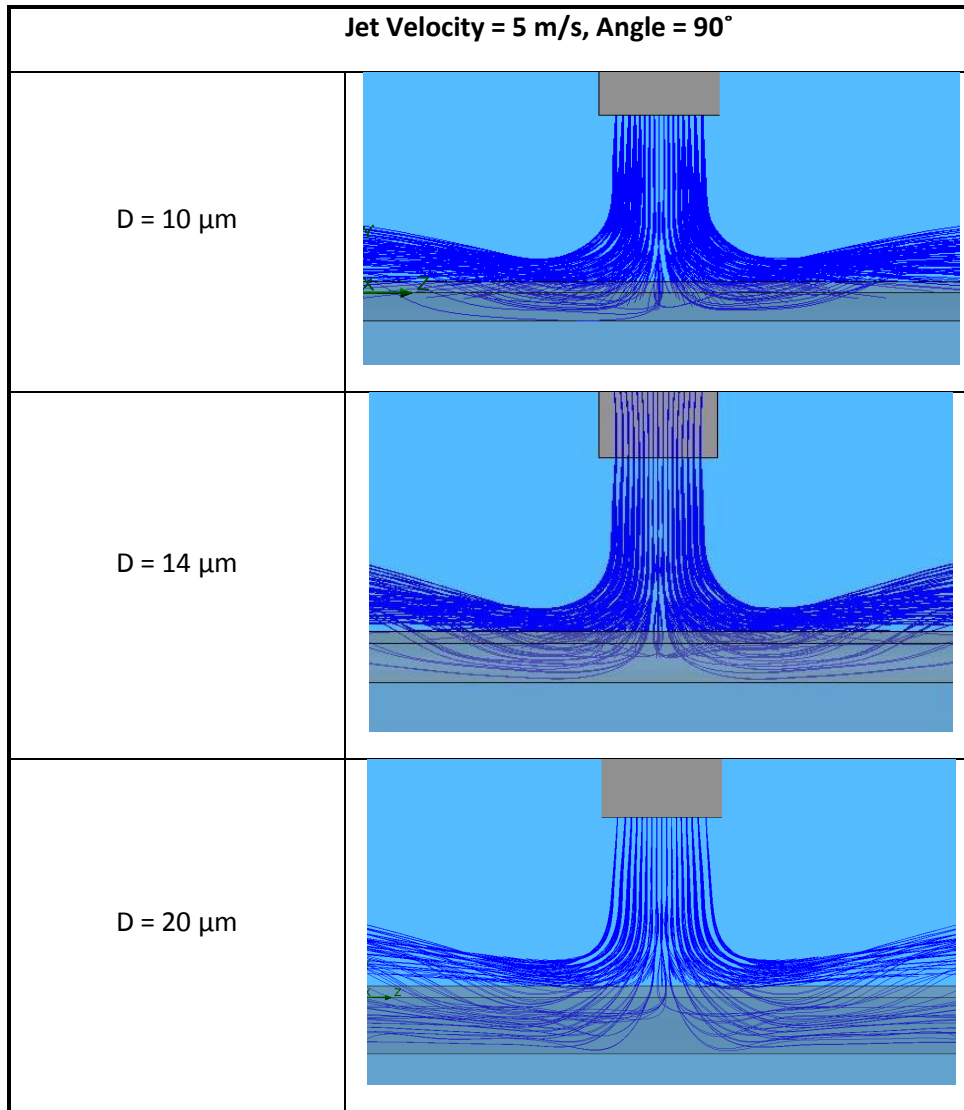


Figure 3.8: Jet velocity simulation results: 5 m/s (side view)

Increasing the velocity of the jet further, corroborates the findings above. At a jet velocity of 10 m/s the jet penetration is even more pronounced, further supporting the hypothesis of the necessity of a higher jet velocity for deeper penetration of the local jet into the trenches. Figure 3.9 above, shows that particle trajectories are able to penetrate deeper into trenches of diameter $D = 20 \mu\text{m}$ than in the case of jet velocities of 3 and 5 m/s. They reach all the way to the surface of the substrate (i.e. the base of the trench) . A similar observation can be made for trenches of diameter $D = 14 \mu\text{m}$.

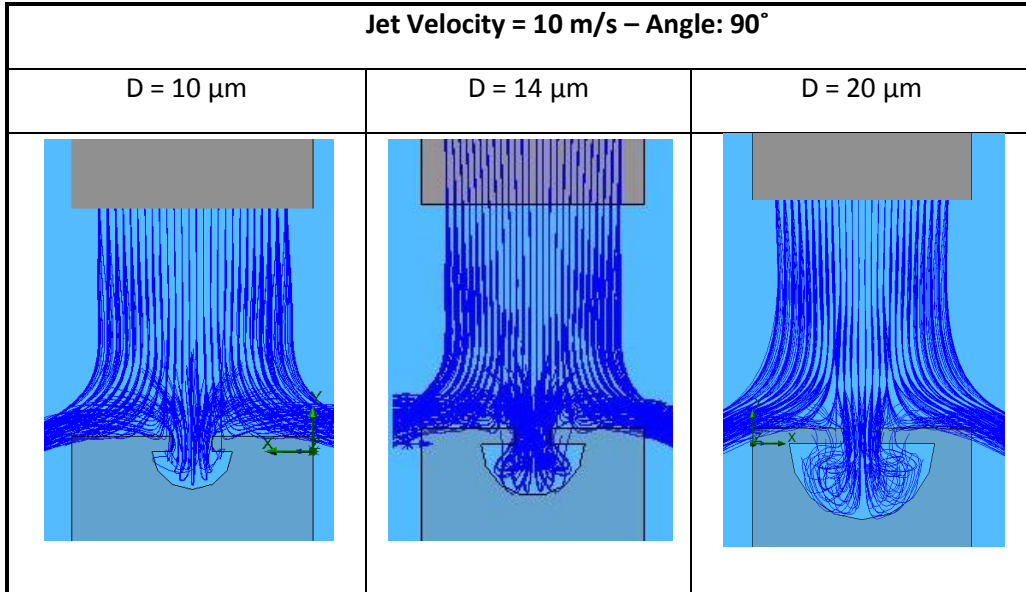


Figure 3.9: Jet velocity simulation results: 10 m/s (cross-section view). At 10m/s the jet penetrates even deeper into the trench than at 5 m/s indicating that higher jet velocities are desirable for the jet etching process.

Again, we notice that as the trench increases in size, the penetrating jet is increasingly directed at sidewalls located at a 45° angle from the vertical. This hints at the fact that the vertical preferential etching is reduced with trench size. However, we can see that in the case of $D = 20 \mu\text{m}$, the trajectory lines become more vertical as the velocity of the jet increases as can be seen in Figure 3.10. This indicates that a higher velocity jet would result in higher aspect ratio features.

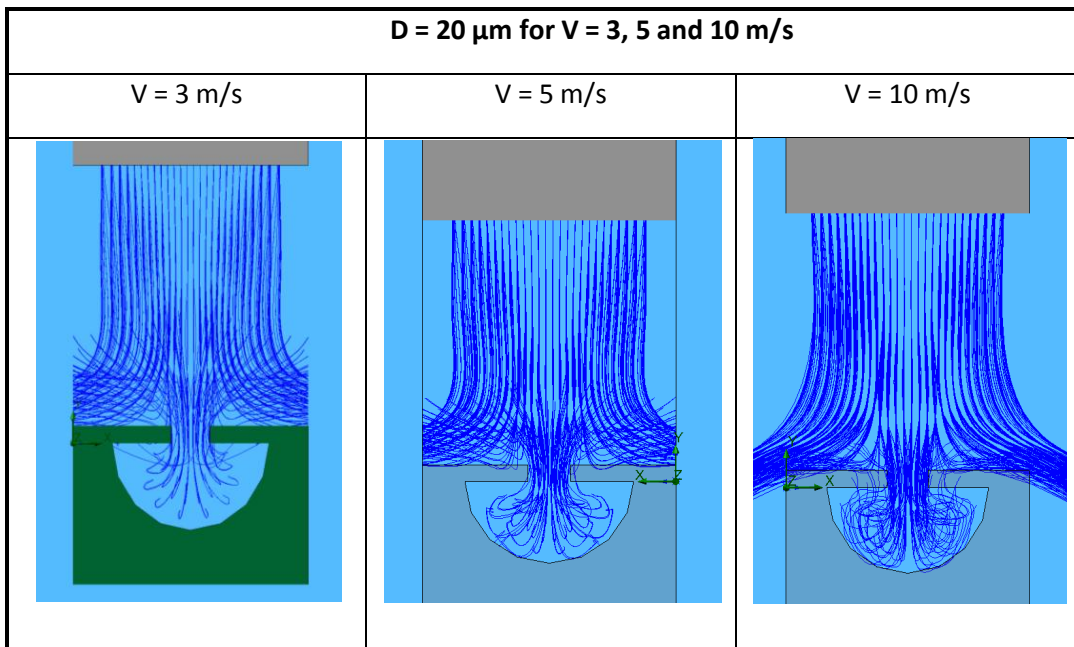


Figure 3.10: Penetration of the impinging jet as a function of speed. As jet velocity increases the etchant penetrates deeper into the trenches.

It is important to note that at this high velocity the trajectory lines suggest a swirling motion of the flow, hinting at a mixing scenario that could work against controlled preferential etching. Additionally, we can observe that at a 90° jet, a splitting of the impinging flow occurs. As can be seen in the side-view figures, the flow splits at an early stage, far above the trench, therefore causing an early diversion of the flow, which reduces its ability to penetrate the trench. This suggests that other jet etching angles should be simulated to observe the effect of jetting angle on the local jet effect.

3.2.3 Impinging Jet at 45 degree Angle.

The figures below summarize simulation results for a jet velocity of 3 m/s and the jet angle for 45 degrees at different trench sizes.

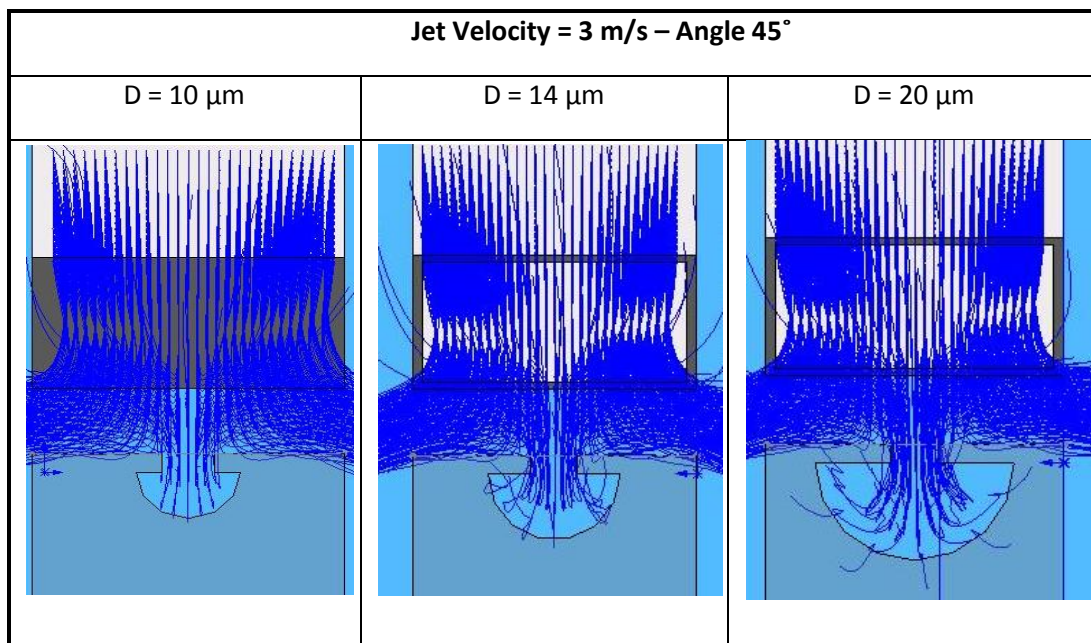
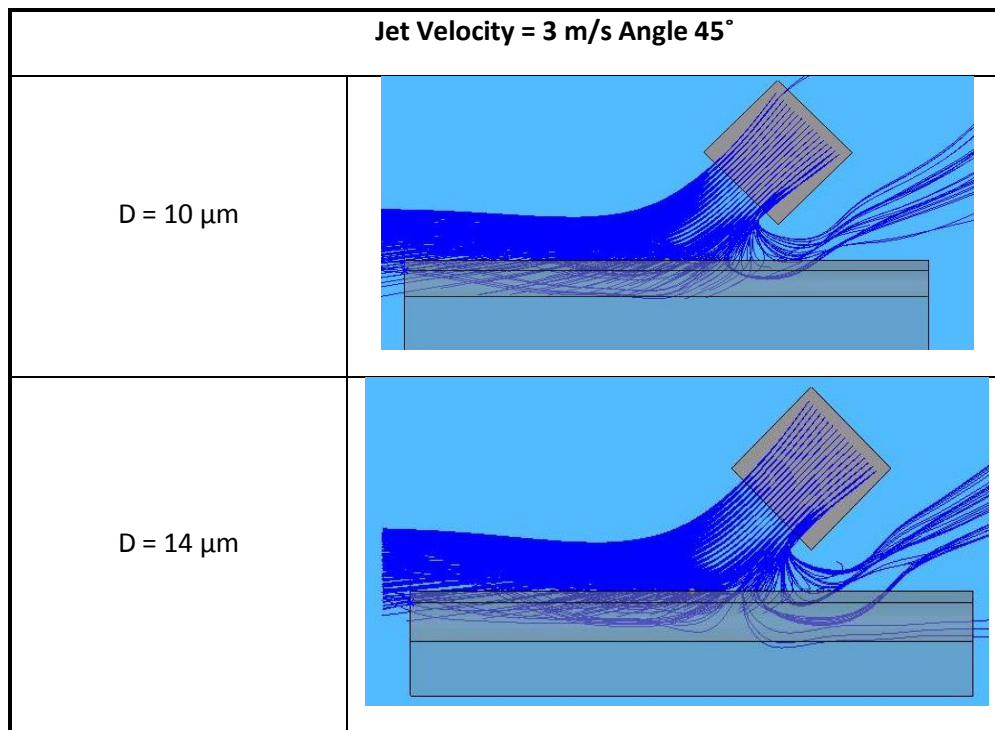


Figure 3.11: Simulation results for jet velocity 3 m/s and angle of 45° (cross-section view). At 45°, the jet enters deeper into the trench than a 90° jet for the same jet velocity.

Figure 3.11 shows that the local jet effect at 3m/s and 45 degree enters deeper into the trench than the jet at 90 degrees (Figure 3.5). This is indicated by trajectory lines that reach deeper into the trench and closer to wall surfaces. Side views of the simulation, summarized in Figure 3.12 illustrate the situation more clearly.

First we see that in the case of $D = 10 \mu\text{m}$, the trajectory lines come in contact with the surface of the substrate at the bottom of the trench. This strongly suggests that this flow configuration is capable of significantly reducing the thickness of both the fluid boundary layer at the bottom of the trench and the diffusion layer between reactants and the surface of the substrate. The fact that multiple trajectory lines terminate at the surface of the substrate is a strong indicator that this flow configuration is advantageous to high aspect ratio etching.

However, as the trench is etched deeper, the ability of the jet to penetrate all the way to the bottom of the trench is reduced. The trajectory lines downstream from the nozzle (at its left) do not reach to bottom of the trench, corroborating previous finding for this jet velocity and trench size. Nonetheless, the 45 degree jet position gives a slight advantage in this case: particle trajectory lines pointing upstream from the nozzle (to the right) are now penetrating deeper into the trench as its size increases. We therefore find that for small trench size, the flow downstream from the nozzle exerts the highest influence on etching preferentially vertically, and as the trench widens, the flow upstream from the nozzle becomes for influent. This result was not existent in the 90 degree case.



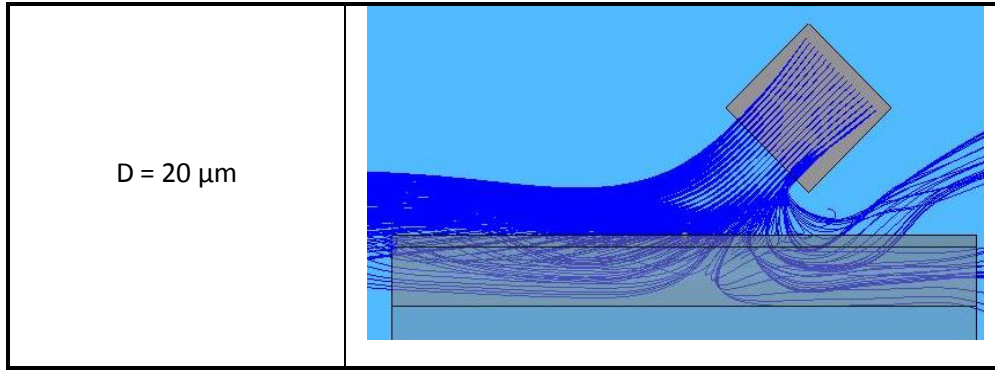


Figure 3.12: Simulation results for jet velocity 3 m/s and angle of 45 degrees (side view).

Results from a simulation of jet speed at 5 m/s and 45 degrees corroborate the findings above. Figure 3.13 and Figure 3.14 show flow lines that reach deeper into the trench than the 3 m/s case. Again, the higher jet velocity leads to a stronger local jet effect, while the 45 degree configuration forces flow lines even deeper. It is important to note that in the $D = 10 \mu\text{m}$ case, we find deep flow lines pointing upstream from the nozzle (to the right) which differs from results found in the 3 m/s case. This indicates that the high flow velocity is forcing more fluid into the trench. In addition, for the flow to reverse its direction and go upstream, it would have to reach deep in the trench. Views in Figure 3.14 for $D = 10 \mu\text{m}$, illustrate this scenario.

Again, we find that as the trench is etched deeper, the amount of flow that becomes reversed in direction increases. Consequently, there is more flow that reaches deeper in the trench, as desired.

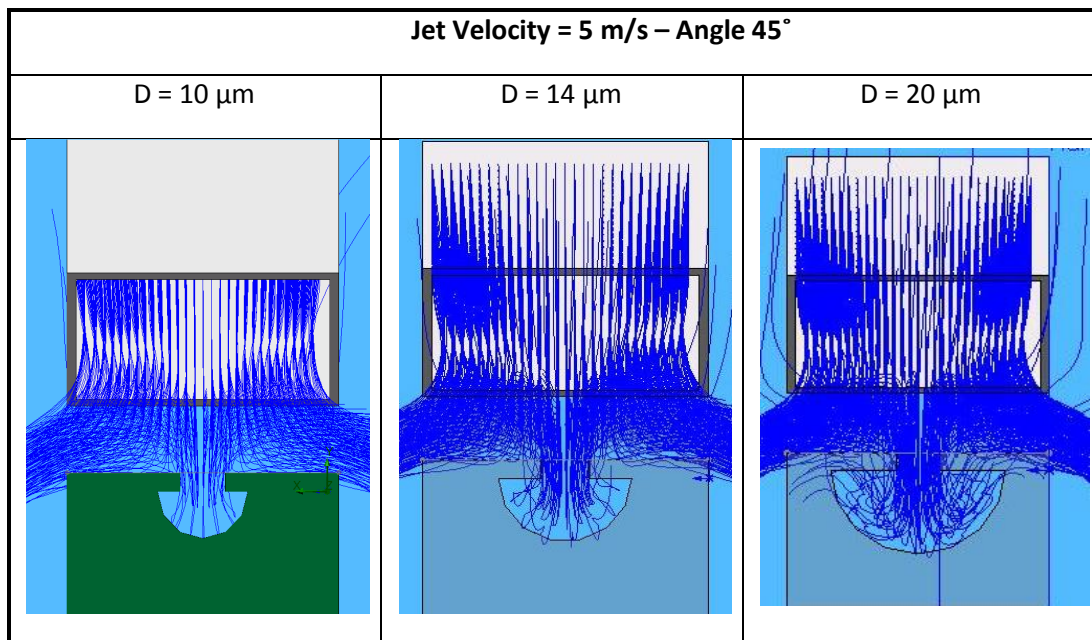


Figure 3.13: Simulation results for jet velocity 5 m/s and angle of 45 degrees (cross-section view).

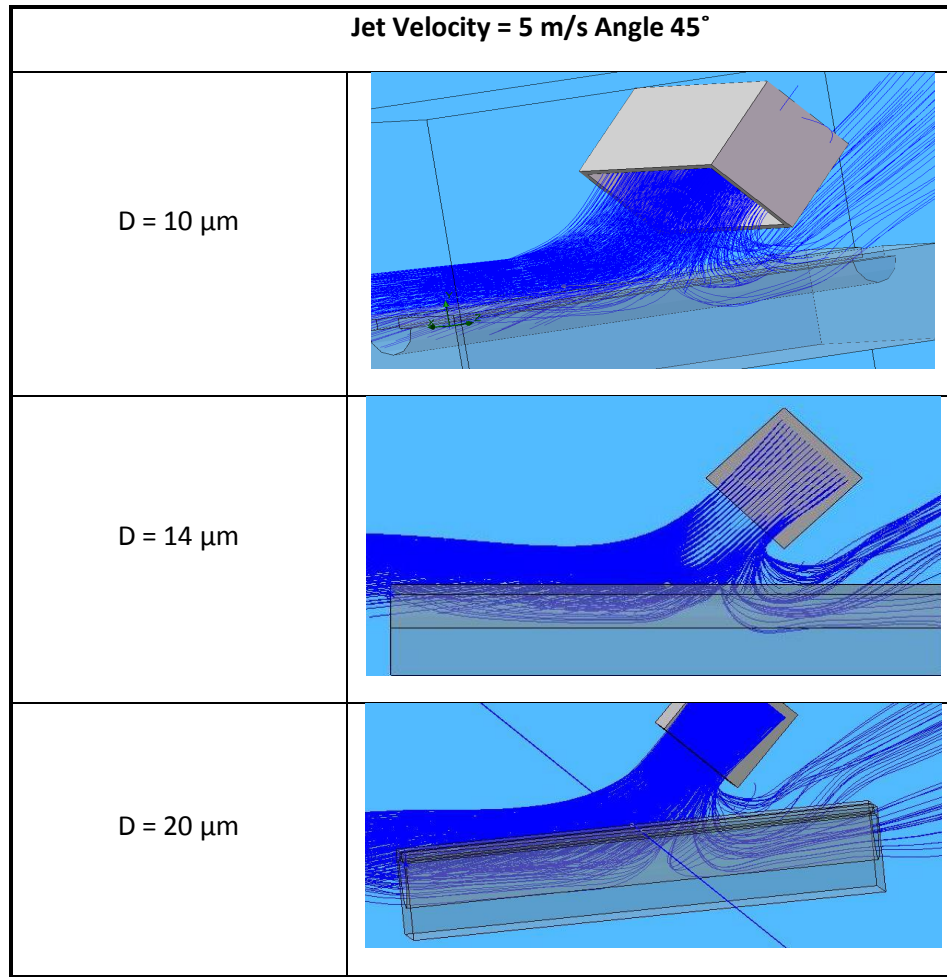


Figure 3.14: Simulation results for jet velocity 5 m/s and angle of 45 degrees (side view)

Finally, the simulation for a jet velocity of 10 m/s further confirms the results above (Figure 3.15).

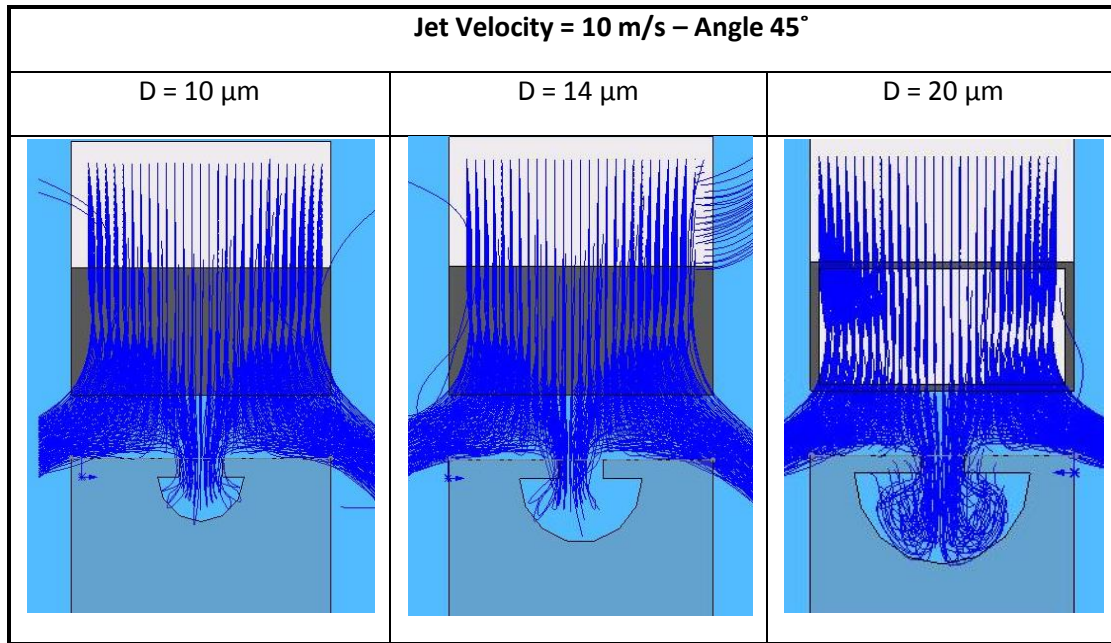


Figure 3.15: Simulation results for jet velocity 10 m/s and angle of 45 degrees (cross-section view)

3.3 Conclusion:

In addition to the effect of jet velocity we considered the effect of impinging jet angle on the jet penetration into the trenches. We have found that increased jet velocity resulted in deeper jet penetration for all scenarios considered. Additionally, at the 45° impingement angle, the flow lines appear to penetrate deeper than in the 90° case, especially the flow lines exiting upstream from the nozzle (at the right hand side) of the jet. In all velocity cases, 3, 5 and 10 m/s at 45° jet, this behavior can be noted. This indicates that using an angle of 45° for jet penetration could result in higher aspect ratio features. We will therefore conduct etching experiment using a 45° angle jet. The jet velocity used in the experiments will be at least 3 m/s and is also limited by safety concerns involved with reaching higher jet velocities.

Chapter 4 - Methodology for Evaluating Trench Cross-section Quality

In order to investigate the effect of the jet on the etching process, we have developed a method of evaluating the quality of the cross-sections resulting from each experiment. The goal of the desired features is to trap incident light into the bulk of the photovoltaic cell. Therefore our defining criterion is the amount of light successfully trapped relative to the amount of light incident on the surface of the cell. We first make use of the Total Internal Reflection (TIR) ability of glass to determine the maximum angle of light reflected from the surface that can be recaptured due to TIR. We then use this measure to determine if the trench cross-sectional shape of a given experiment is well suited for trapping light given the assumption of TIR.

4.1 Total Internal Reflection:

$$\sin \theta_c = \frac{n_2}{n_1}$$

The equation above describes the relationship between the critical angle θ_c , and the refractive index of the two media at the interface (n_1 and n_2) (25). The critical angle is defined as the angle above which total internal reflection occurs. In Figure 4.1, if θ_2 is the critical angle, any incident light at an angle larger or equal to it will get reflected and any light incident at angles below it will be split as is the case of the light ray with angle of incidence of θ_1 . The refractive index n_1 refers to the more optically dense medium (glass) while n_2 refers to the less optically dense medium (air).

Using refractive indexes for glass and air as $n_1 = 1.50$ and $n_2 = 1.00$ respectively, we get the following value for critical angle:

$$\theta_c = \sin^{-1}\left(\frac{n_2}{n_1}\right) = \sin^{-1}\left(\frac{1.00}{1.50}\right) = 41.8^\circ$$

Therefore the critical value of the angle necessary for TIR between glass and air is: $\theta_c = 41.8^\circ$.

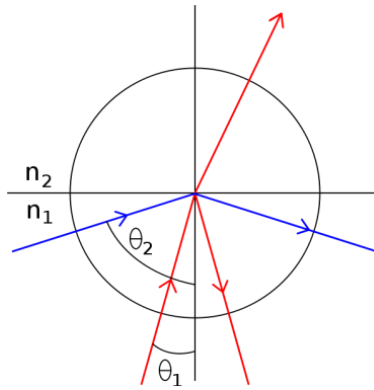


Figure 4.1: Total Internal Reflection (26). A ray of light that is incident of the interface at an angle greater than the critical angle is reflected.

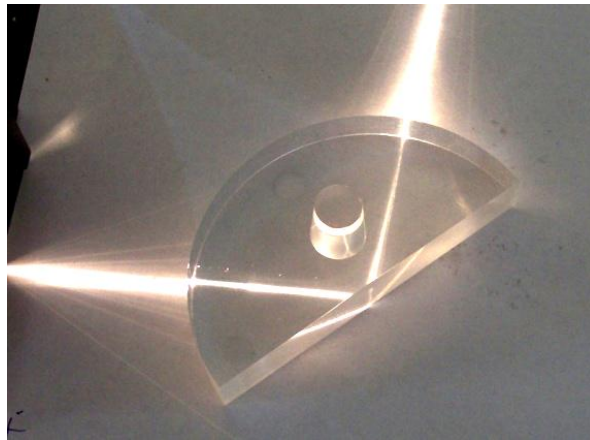


Figure 4.2: Total Internal Reflection (27)

4.2 Q-Factor Definition:

Light incident on the surface of a semicircular trench will be partially absorbed and partially reflected. Reflected light rays will either bounce back into the substrate when they “hit” the surface at high enough trench profile slope (green light ray in Figure 4.3), or reflect out of the trench when they “hit” at a low slopes (blue light ray). There is however a range of slopes at which light bounces out of the trench but is recaptured by the TIR effect of the glass on top of the cell. The light ray depicted in red describes this situation. In this case, the minimum slope of the trench that results in light bouncing at an angle subject to TIR is the one corresponding to a tangent that is at angle of $\theta_c / 2$ from the horizontal as depicted in Figure 4.3.

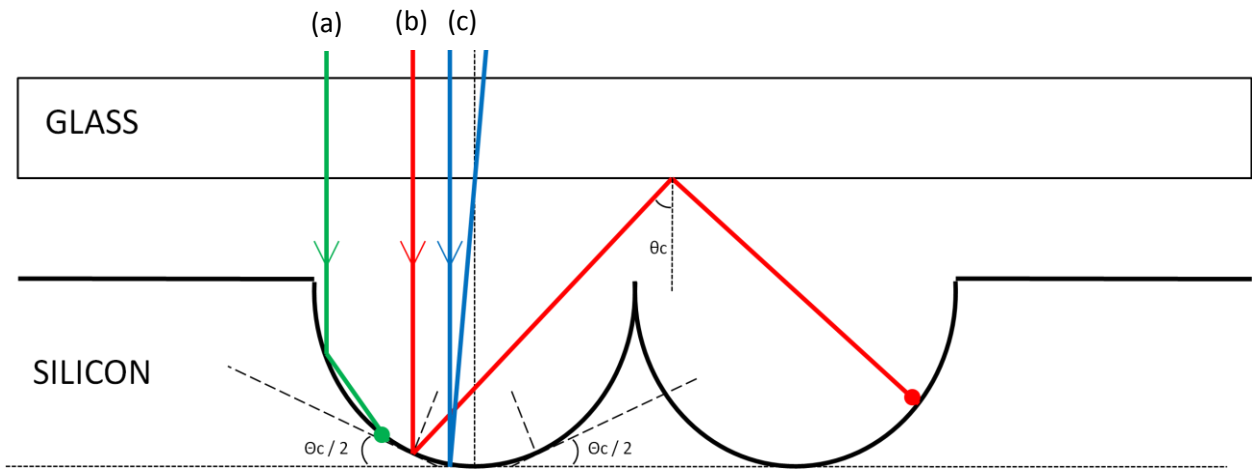


Figure 4.3: Light Bouncing on Surface of Trench. Incident light at locations with slopes higher than $\theta_c / 2$ are absorbed immediately by the substrate (a), the ones incident at slope about $\theta_c / 2$ are reflected out of the trench but recaptured by the glass (b). Finally incident light at slopes lower than $\theta_c / 2$ is reflected of the trench and escapes through the glass.

This indicates that locations on the trench profile that have a tangent forming an angle of less than $\theta^* = 20.9^\circ$ with the horizontal will result in reflecting light with no recapture (or with no double bounce). Assuming the trenches are etched in a symmetric fashion, we can define 2 points between which the reflected light will not be recaptured. Let's define the linear distance between these 2 points as the "distance of no double bounce" as depicted in Figure 4.4. We then define the no light recapture factor, or "Q-factor": "Q" as:

$$Q = \frac{\text{Distance of no double bounce}}{\text{Width of the trench}}$$

It is important to note that as the distance of no double bounce decreases the value of the Q-factor also decreases. The smaller this distance is, the less light escapes the trench and the glass, making the trench profile more desirable. It is therefore more desirable to have a low Q-factor than a high one.

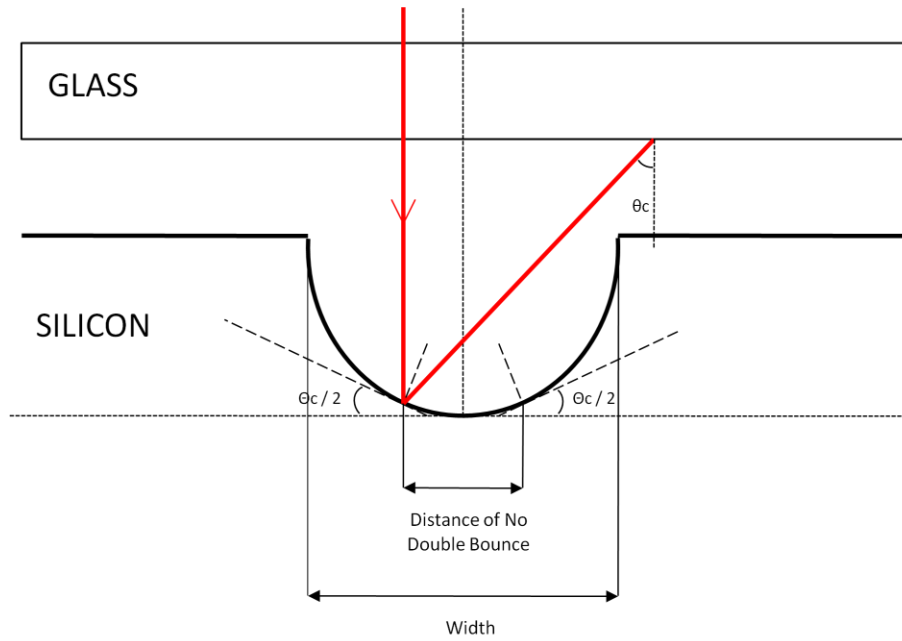


Figure 4.4: Illustration of trench quality

4.3 Aspect Ratio Definition:

Next we define another measure that has an impact on the light trapping ability of the trench profile achieved. The depth of a trench can generate situations where light bouncing on the surface of the trench at angles higher than what is required for TIR would still be trapped just because the side walls of the trench are high enough to obstruct the path of the light ray out of the trench. Figure 4.5 illustrates this scenario by showing that a light ray that would have escaped the trench depicted in Figure 4.4, is now captured by the side walls because the trench in Figure 4.5 has higher depth for the same width. This leads us to define the aspect ratio (AR) of a trench profile as the ratio of its depth to its width.

$$AR = \frac{\text{Depth of Trench Profile}}{\text{Width of Trench Opening}} = \frac{d}{w}$$

In the case of a trench that is etching from a narrow mask opening of ideal opening distance close to 0 μm , we the trench profile would be a semi-circle of aspect ratio ($AR_{\text{isotropic}}$):

$$AR_{\text{isotropic}} = \frac{\text{depth}}{\text{width}} = \frac{r}{2r} = \frac{1}{2}$$

Where the depth of an ideally isotropic trench is equal to the radius “r” of the trench and its width is equal to the diameter “2r”.

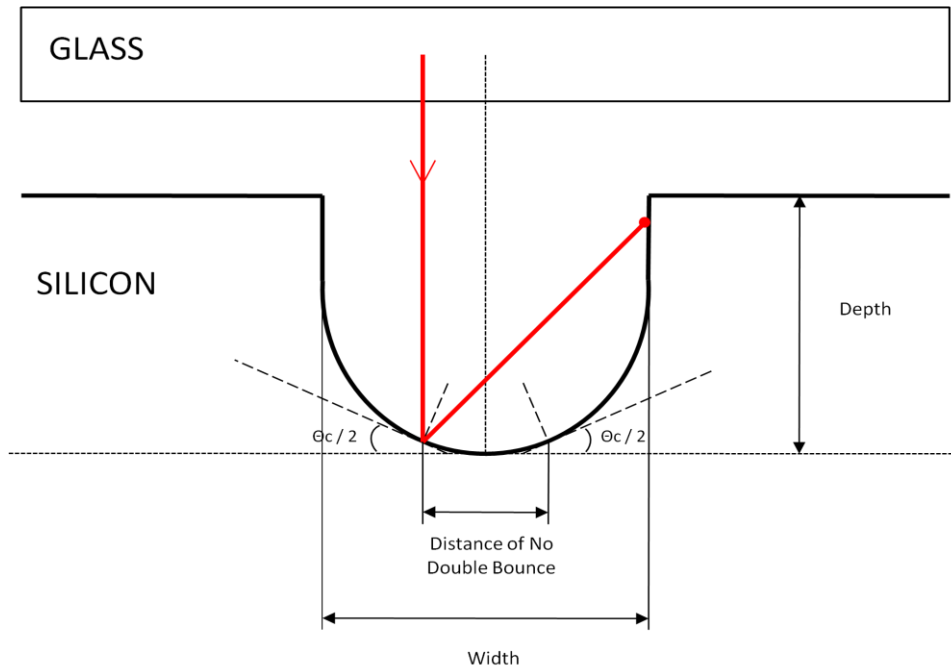


Figure 4.5: High Aspect Ratio Trench. When the aspect ratio of a trench increases, it becomes capable of trapping light that would have escaped at lower aspect ratios.

4.4 Theoretical Limits:

From the above discussion, one can conclude there is a limit for the Q-factor method for trench quality evaluation. When trench profile aspect ratios are too high the light bouncing at $\theta^* = 20.9^\circ$, which would be normally reflected from the trench and recaptured by the TIR effect of the glass, is now recaptured by the sidewalls of the trench. This indicates that the Q-factor method established above would not be valid at high aspect ratios. We therefore set out to determine the maximum aspect ratio at which the Q-factor method is still valid. Once we determine this value, we can compare it to the AR values obtained from experimental results; if they are lower than the maximum AR value, the Q-factor method will hold.

To further illustrate the issue, we developed Matlab models that enable us to find the maximum aspect ratio for which the Q-factor method will hold. We assume that the trench cross-sections are parabolas with constant width but varying aspect ratios and following an equation of the type:

$$y = c \cdot x^2$$

The “c” coefficient will vary depending on the aspect ratio of the parabola under study. We first model a parabola of aspect ratio of 0.5 as shown in Figure 4.6. The solid line represents the trench profile and follows the equation above. We model the shape of the trench over a range of 20 μm in the x-axis, consistent with the desire to model trenches with a fixed opening of 20 μm . Next we plotted on the same figure the tangent to the parabola at an angle equal to $\theta^* = 20.9^\circ$ and its orthogonal at the tangent point in order to define the axis of symmetry relevant to light reflection. Finally, the dotted line represents a vertically incident light ray after it bounces off the surface of the trench.

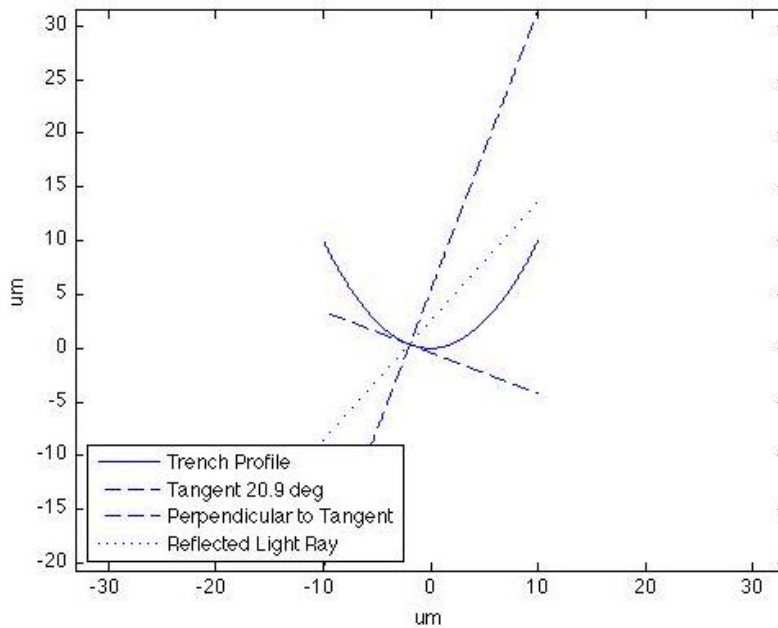


Figure 4.6: Parabola of aspect ratio of ½. Light incident at 20.9° escapes the trench but is captured by the glass through TIR.

We can see in Figure 4.6 that at an aspect ratio of 0.5 light can be reflected off the trench surface, escape the trench and get recaptured by the glass at TIR. For this configuration the Q-factor method will hold.

Next, we model a parabola of aspect ratio equal to unity, keeping the top width of the parabola at 20 μm . Figure 4.7 shows the result of the model and indicates that for a trench of aspect ratio 1, light being reflected at $\theta^* = 20.9^\circ$ will be trapped in the trench. This means that the angle of tangents at which the light escapes the trench in this case is smaller than θ^* and the distance of no double bounce region is smaller in this case. Therefore, the Q-factor method developed earlier cannot be used to evaluate the quality of the trench.

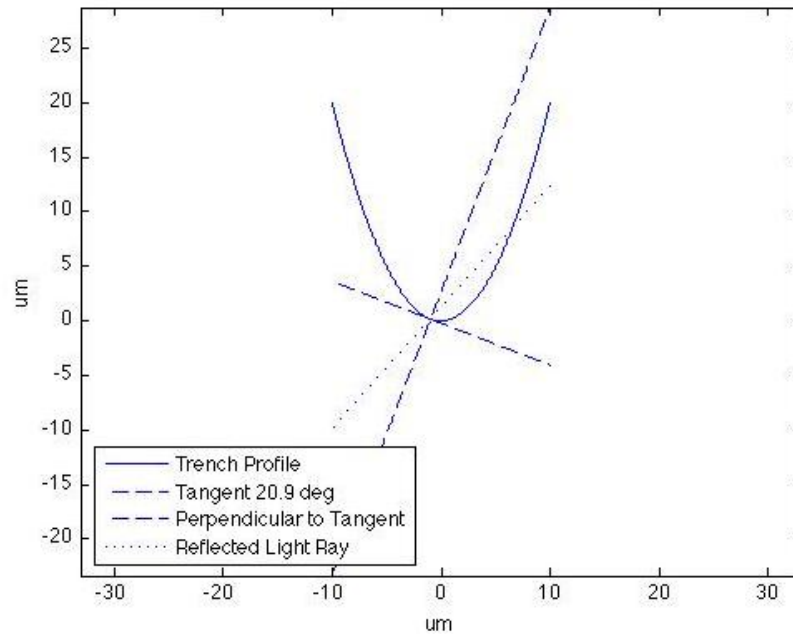


Figure 4.7: Parabola of Aspect Ratio 1. Light incident at 20.9° is captured by the sidewalls of the trench of aspect ratio 1.

Finally, we determine the maximum aspect ratio for which the Q-factor method works. This would be limiting scenario where the light that bounces at $\theta^* = 20.9^\circ$ coincides with the edge of the trench opening as shown in Figure 4.8. In this case, light reflected from the surface of the trench at exactly θ^* will start to be trapped in the trench. At aspect ratios higher than this limiting aspect ratio, the light will be trapped and at lower aspect ratios the light will escape. We find this aspect ratio to be equal to $AR_{\text{max}} = 0.65$.

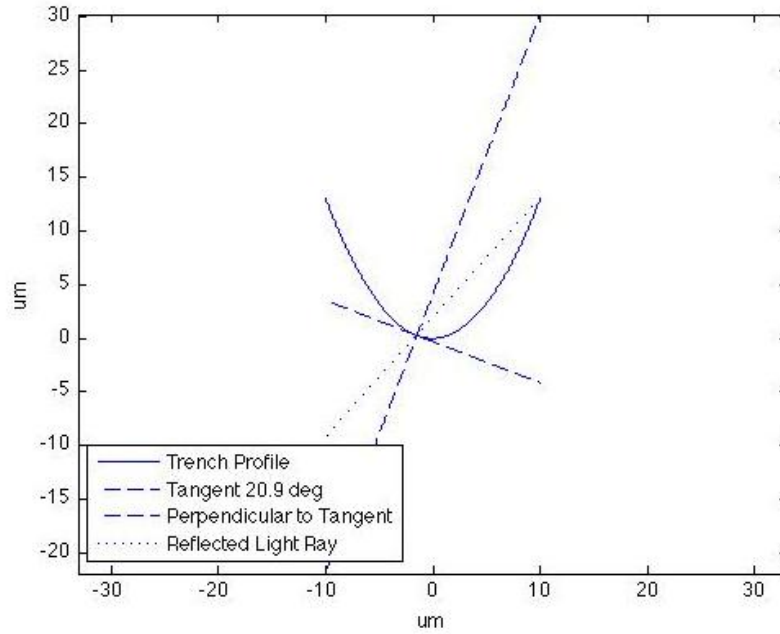


Figure 4.8: Parabola of aspect ratio 0.65 (limiting case). At this aspect ratio incident light at 20.9° is absorbed by the top of the trench and is the limiting aspect ratio for the Q-factor method to be used

In addition, using the model in Figure 4.8 we can define a theoretical maximum value for the Q-factor method used. Since the “distance of no double bounce” in this case would be the smallest distance possible for this evaluation method, we can define the ideal Q-factor as:

$$Q - factor_{ideal} = \frac{\text{Distance of no double bounce region for } (AR_{max} = 0.65)}{\text{Width of trench opening}}$$

Taking the x-coordinate of the point where the tangent at $\theta^* = 20.9^\circ$ intersects the parabola and multiplying it by a factor of 2 to account for symmetry will give the distance of no double bounce region in this ideal case:

$$\text{Distance of no double bounce region for } (AR_{max} = 0.65) = 2.953\mu m$$

Therefore:

$$Q - factor_{ideal} = \frac{2.953}{20} = 0.1476$$

In conclusion, the Q-factor method, which evaluates the quality of a trench shape based on its ability to trap light and reflect it such that it will be recaptured through TIR, is only valid when the aspect

ratio of the trench being evaluated is less than $AR_{\max} = 0.65$. We measure aspect ratios for every trench evaluated and compare it to this standard. Although our efforts were in the goal of achieving a trench profile of aspect ratio close to 1, we do not achieve aspect ratios higher than 0.65. This allows us to use the Q-factor method for evaluating all trench profiles resulting from our experiments. In addition, we will note that Q-factor values approaching values of $Q\text{-factor}_{\text{ideal}} = 0.1476$ are very desirable and represent a high quality trench profile.

4.5 Measurement Method

After conducting an etching experiment, we imaged the cross-section of the resulting trenches by breaking the sample along a direction orthogonal to the trench longitudinal axis. We then observe the trench cross-sectional profiles under microscope and take electronic images of the profiles of interest. We then use an imaging software that allows us to superimpose the trench profile image with other layers on which we draw lines of interest. The most relevant lines we use are the ones that form an angle of 20.9° with the horizontal of shown in Figure 4.9. These lines will be used to determine the points of intersection between the trench profile and the 20.9° tangent. These points will be in turn used to measure the distance between them, which is also the distance of no double bounce region (NDB). We also measure the distance between two points at the trench opening and the depth of the trench. All distances are measured in pixels, but it is of little relevance however since our defined metrics are ratios of the same dimension and are therefore unit-less (distance/distance).

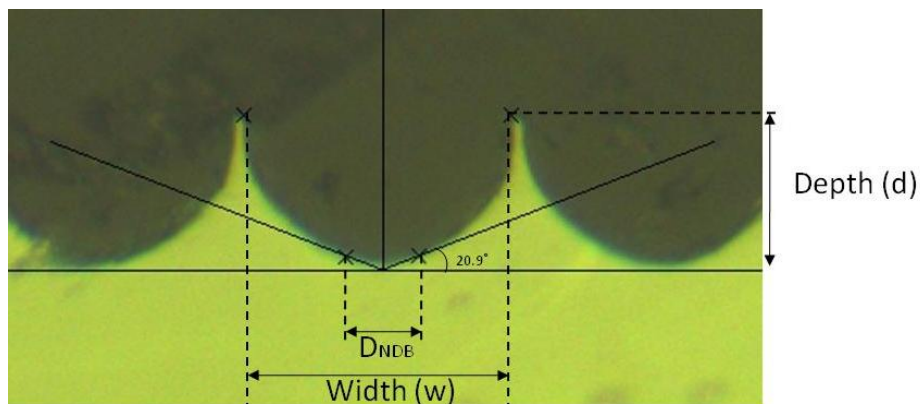


Figure 4.9: Illustration of method used to measure Q-factor and Aspect Ratio. The No Double Bounce region is the ratio of non-absorbing area over the width of the trench.

Using measurement in pixel units for D_{NDB} , Width (w) and Depth (d), we can deduce the aspect ratio (AR) and Q-factor as follows:

$$AR = \frac{d}{w}$$

And

$$Q - factor = \frac{D_{NDB}}{w}$$

We apply the imaging method described above to all experiments performed in this work and report Q-factor values as “Q” and aspect ratio values as “AR”.

Chapter 5 - Jet Etching Experimental Set Up and Hardware:

5.1 Etching Solution used

Previous work was conducted by colleagues to determine the ideal solution to be used for high aspect ratio etching. As explained in section 2.3.1 the Hydrofluoric, Nitric and Acetic acid system was used to yield an etchant solution that suits the goal of isotropic etching. This research work was conducted by testing numerous compositions in the HNA system that best conduct the process of isotropic etching in single crystal silicon of <100> orientation. The solution with highest degree of isotropy in <100> Si that was tested is a solution of 11:2:4 (Nitric: Acetic: HF) by volume, using the following acid concentrations: 48% for HF, 70% Nitric acid and 99% for acetic acid.

We will use this etching composition for all jet etching experiments conducted hereafter.

5.2 Stationary Jet Apparatus Description

In order to confirm the jet behavior suggested by the simulations, we conducted a series of experiments using a jet etching apparatus Figure 5.1. It consists of a reservoir of etchant solution (HNA 11:2:4) elevated at a distance $h = 19$ in from the surface of the sample. The solution is channeled from the reservoir through a Teflon tube to a nozzle located in proximity of the sample to be jet etched. The distance between the sample and the exit of the nozzle is about $l = 0.5$ mm. The nozzle consists of a flattened tube extremity that has been thermo formed into a rectangular-shaped opening with dimensions $w = 0.84$ mm and $L = 5.0$ mm. The etching fluid is allowed to flow down the Teflon tube when the valve is opened and gravity supplies the necessary energy to pressurize the fluid resulting in a jet velocity of about $v = 3$ m/s according to the calculations below.

We can estimate the velocity of the jet using a Bernoulli equation approximation of the fluid speed that the exit of the jet. Bernoulli's equation states that:

$$\frac{P}{\rho} + \frac{v^2}{2} + gz = \text{constant}$$
$$\frac{P_1}{\rho} + \frac{v_1^2}{2} + gz_1 = \frac{P_2}{\rho} + \frac{v_2^2}{2} + gz_2$$

Where,

P_1 , P_2 are the pressures exerted on the location 1 and 2 of the fluid. Since both are at atmospheric pressure, then $P_1 = P_2 = P_{atm}$

v_1 , v_2 are the velocities of the fluid at locations 1 and 2, where $v_1 = 0$ m/s

z_1 and z_2 are the height of locations 1 and 2, where z_2 is taken as reference height at $z_2 = 0$ and therefore $z_1 = 19$ in as shown in Figure 5.1.

After further manipulation:

$$v_2 = \sqrt{2gz_1}$$

$$v_2 = 3.07 \text{ m/s}$$

We therefore estimate the velocity of the fluid exiting the nozzle at $v = 3$ m/s. All experiments will be conducted using this jet velocity.

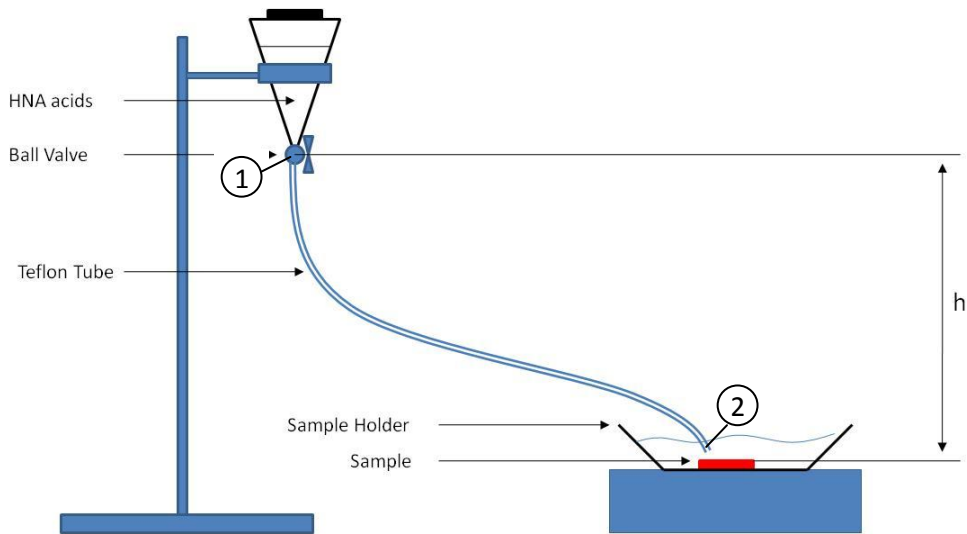


Figure 5.1: Stationary Etch Apparatus

The estimated velocity is a lower bound in our calculation since we picked the lowest point in the reservoir for our calculations. When the reservoir is full the fluid drops from a higher distance, resulting in a higher theoretical velocity.

The apparatus described in Figure 5.1 is only capable of producing a stationary jet of HNA acids. In other words, this apparatus is not equipped with elements that enable it to scan the surface of the sample back and forth as is the case for the apparatus described in section 5.3. This stationary apparatus was used in the order to conduct preliminary tests for jet etching and observe the jetting effect in the goal of determining if further investigation is desirable. Having observed encouraging results described in chapter 6, we construct a more sophisticated apparatus, fitted with the moving jet nozzle features, and allowing for more accurate experimentation. The following section is a description of this apparatus.

5.3 Moving Jet Apparatus Description

In the goal of conducting further experiments with jet etching, we have designed and built a jet etching apparatus with moving jet nozzle ability as well as additional features described below. The core parts of this device are the sample holder which is designed to securely hold the sample to be etched; the etch bath container, designed to hold the sample holder and contain fluid overflowing from its, and finally, the revolving mechanism which serves the purpose of enabling a back and forth scanning motion of the jet nozzle.

5.3.1 The Sample Holder:

As one of the most critical components of the entire apparatus, the sample holder serves the role of housing the sample while it is being jet etched. Important characteristics of this part is that it should enable securely attaching, easily detaching a sample, quick removal from an etch bath in order to stop etching at the desired time and allow the jet nozzle to span distances greater than the sample dimensions.

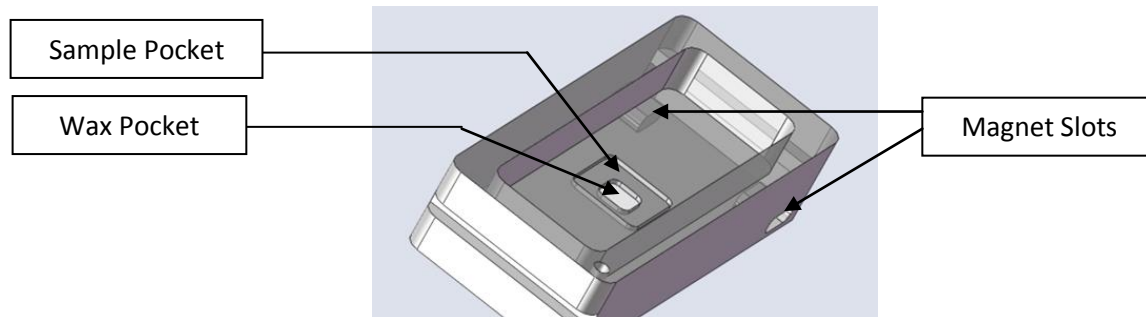


Figure 5.2: 3-D model of sample holder

In order to attach a sample in a secure fashion, we have designed a recessed pocket under the surface holding the sample, which we fill with wax. Before placing the sample, we heat it up using a low temperature heat source such as a heat gun and then place the heated sample in the “sample pocket” as seen in Figure 5.2. The wax in the pocket under the sample holder melts on the back surface of the sample and later solidifies as the sample and wax cool down. This provides a strong enough bond between the sample and the wax to go through experiments with the sample remaining securely in place. Figure 5.3 shows dimension of the wax pocket described above.

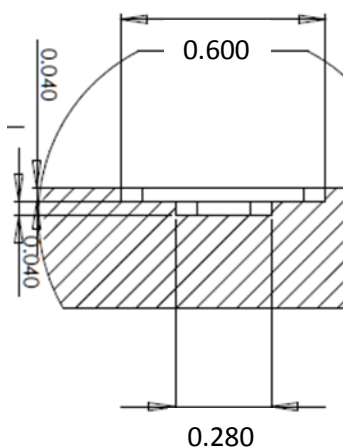


Figure 5.3: Wax Pocket and Sample Pocket Dimensions in Inches

The “sample pocket” is designed to have a surface area large enough to hold a square silicon sample with dimension of 0.5”x 0.5”. Therefore, we designed this feature to be 0.6”x 0.6” with a depth of 0.040 in (1mm), which is about twice the dimension of the thickest silicon sample tested (500 μ m). This depth was also chosen to provide clearance between the jet nozzle and the top surface of the sample while keeping the jet nozzle close to the surface of the sample for an optimum jet effect.

Additionally, the overall dimensions of the sample holder are rectangular in nature to accommodate for the need of the jet nozzle to span a distance larger than the sample dimension itself. Given that we have a circular rotor and a crank shaft assembly, the resulting linear motion of the jet nozzle will follow a close to sinusoidal velocity profile. Its highest velocity will be at positions of $\pi/2$ and $3\pi/2$ of the rotor (corresponding to position where the jet nozzle is on top of the sample), considering that at angular positions of the rotor at 0 and π the jet nozzle is the furthest away from the sample on each side of it. Figure 5.4 shows the effect of the relationship between the rotor wheel dimensions, crank arm dimensions on the angular and linear positions of the jet nozzle. We can see that at a rotor of diameter 5 cm and crank arm length $L = 11$ cm, the jet nozzle has a relatively constant velocity over the sample region indicated by a constant slope of the near- sinusoid in that region. As the relative change in linear position is equal to the relative change in angular position, the linear velocity of the nozzle is constant which is the desired condition for the jet etching process.

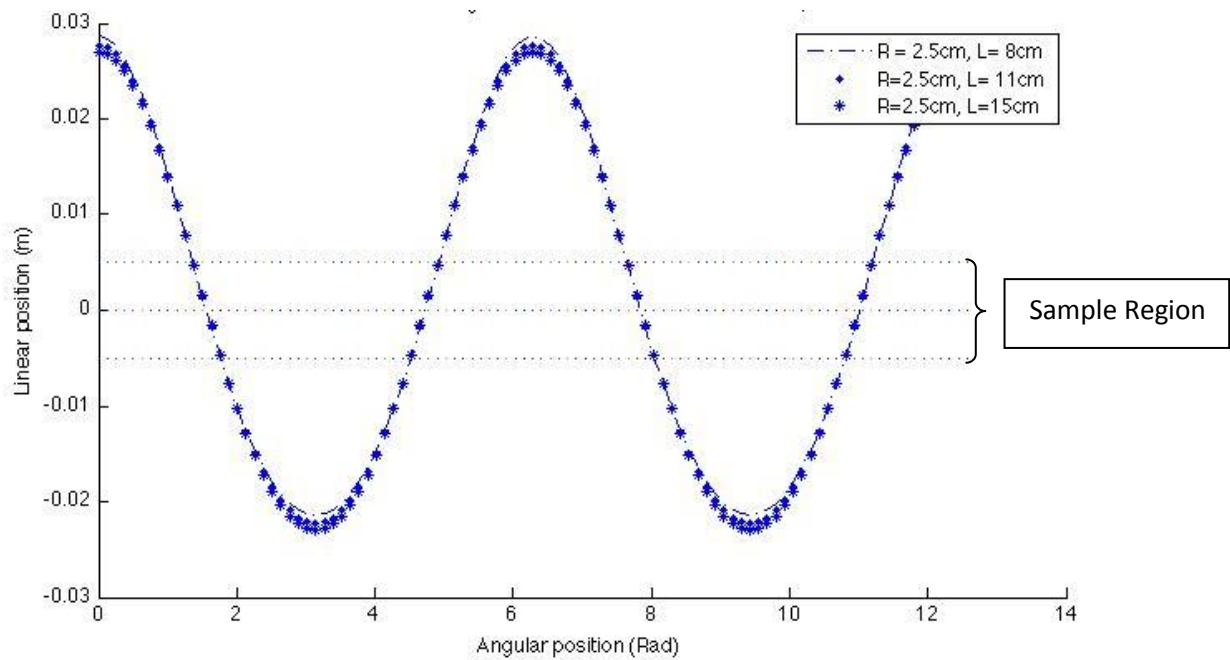


Figure 5.4: Linear Position vs Angular Position. Over the sample region the jet nozzle has a constant linear velocity.

An additional issue to consider with the design of the sample holder is the fact that it has to be quickly removable in order to remove the sample from the etch bath at the desired etch time. In addition, we have to be able to place the sample back in its original position, at the appropriate location under the jet nozzle. This led us to the design of a slot in the etch batch container where the sample

holder fits and is then secured down using magnetic force. We place four magnets in each corner of the base of the sample holder in the slots shown in Figure 5.5, which are then attracted to magnets placed on the etch bath container shown in Figure 5.11. The magnets offer the advantage of an attractive force between the sample holder and the etch bath container that is strong enough for secure attachment, yet weak enough to allow for a quick removal of the sample holder when needed.

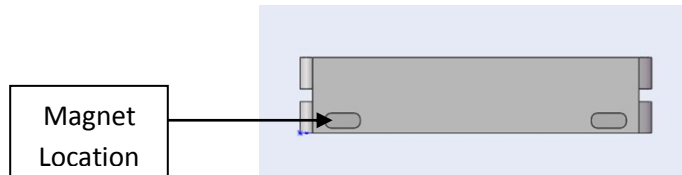


Figure 5.5: Side-view of sample holder

Finally, the material used for the construction of this part is Noryl. It is a hard plastic, resistant to acid and easily machinable.

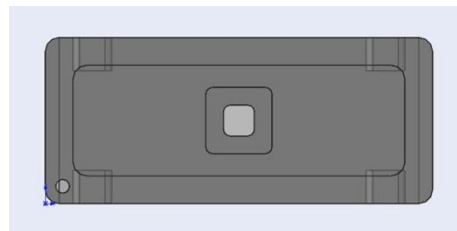


Figure 5.6: Top view of sample holder.

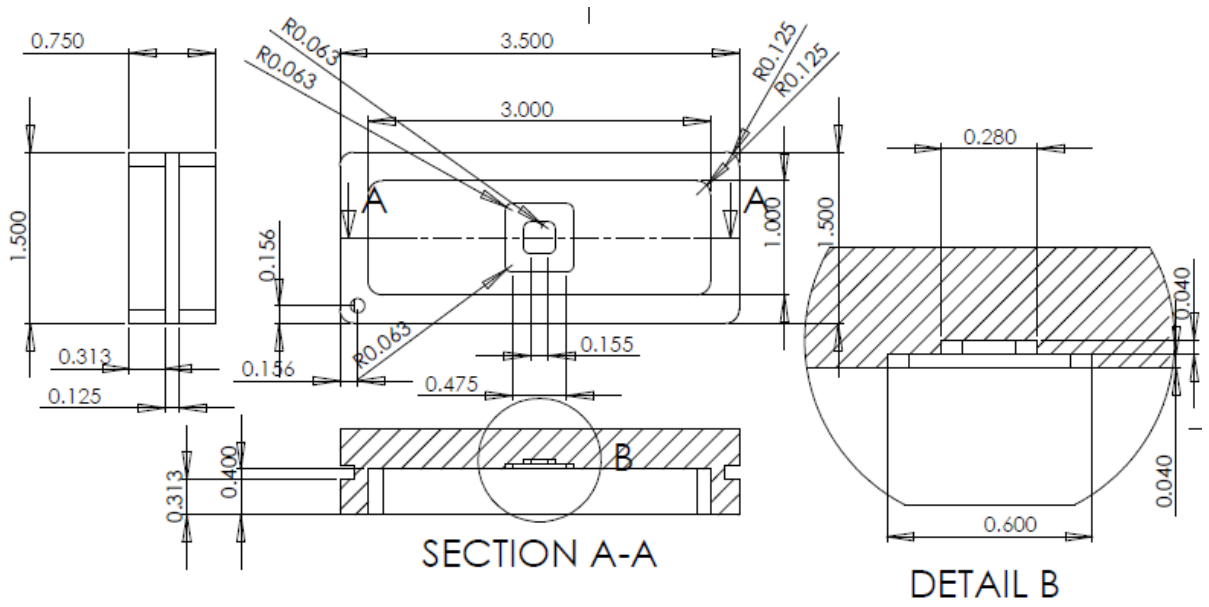


Figure 5.7: Dimension details for Sample holder

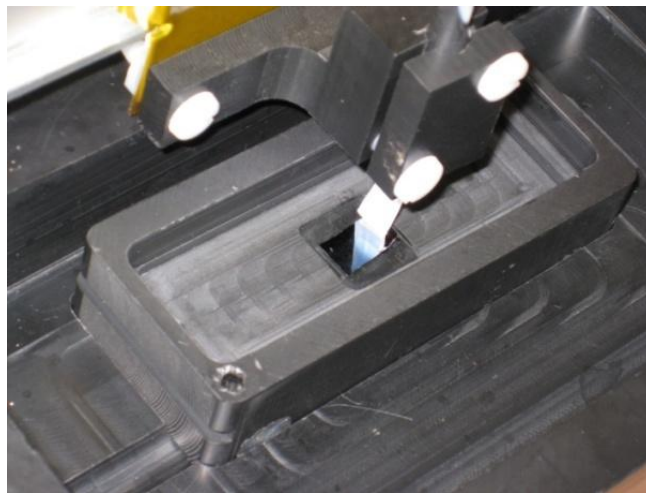


Figure 5.8: Sample Holder Picture

5.3.2 The Etch bath Over-Flow Container:

The sample holder described above is placed in a container that serves primarily the function of capturing etching bath over-flow. As the etchant is jetted on the surface of the sample, the additional fluid being added to the bath from the reservoir causes the bath to overflow. The overflow container then captures the excess fluid which is then drained into a beaker for further re-use. This container also serves the purpose of capturing overflowing fluid from the quenching process. When the jet etching

process is complete, we stop the flow of the jet by closing the valve on the reservoir shown in Figure 5.1. However, the etching reaction continues in the stationary bath. It is therefore extremely critical to stop this reaction through the quick addition of a large amount of diluting solution, water in this case. The added volume of fluid from the quenching process causes the etch bath in the sample holder to spill over into the overflow container and then drain to a second beaker through a diverting valve. This diluted etchant is then properly disposed of.

An important characteristic of this part is its inclined bottom surface combined with a flat surface for the sample holder to rest. The inclined bottom surface, as shown best in Figure 5.13, serves as a height difference for draining fluid out of the container through the drain hole located at the lowest point of the surface. The sample holder surface is horizontal in order to keep alignment between the jet nozzle sweeping motion and the rest of the parts. We also design the sample holder surface as a recessed surface with respect to the bottom of the over-flow container in order to provide a slot for the sample holder to fit into as shown in Figure 5.12. This allows for the easy and precise placement of the sample holder.

In addition, we insert magnets in the bulk of the over-flow container such that they are positioned in close proximity to the flat surface supporting the sample holder. These magnets exert an attractive force on the ones contained in the sample holder and provide a force securing the sample holder to the overflow container. Finally, we make this part out of Noryl as well for its ease in machining and resistance to acids.



Figure 5.9: Overflow container - Side View



Figure 5.10: Over-flow container top view

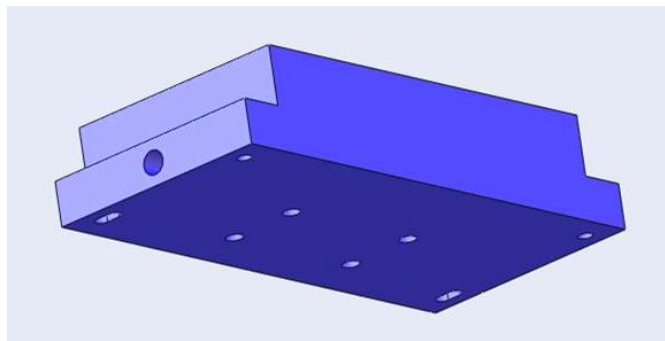


Figure 5.11: Etch Bath Container (view showing magnet locations)

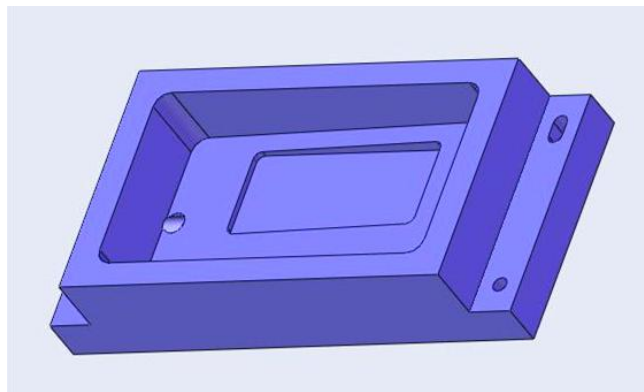


Figure 5.12: Over-flow container 3D view

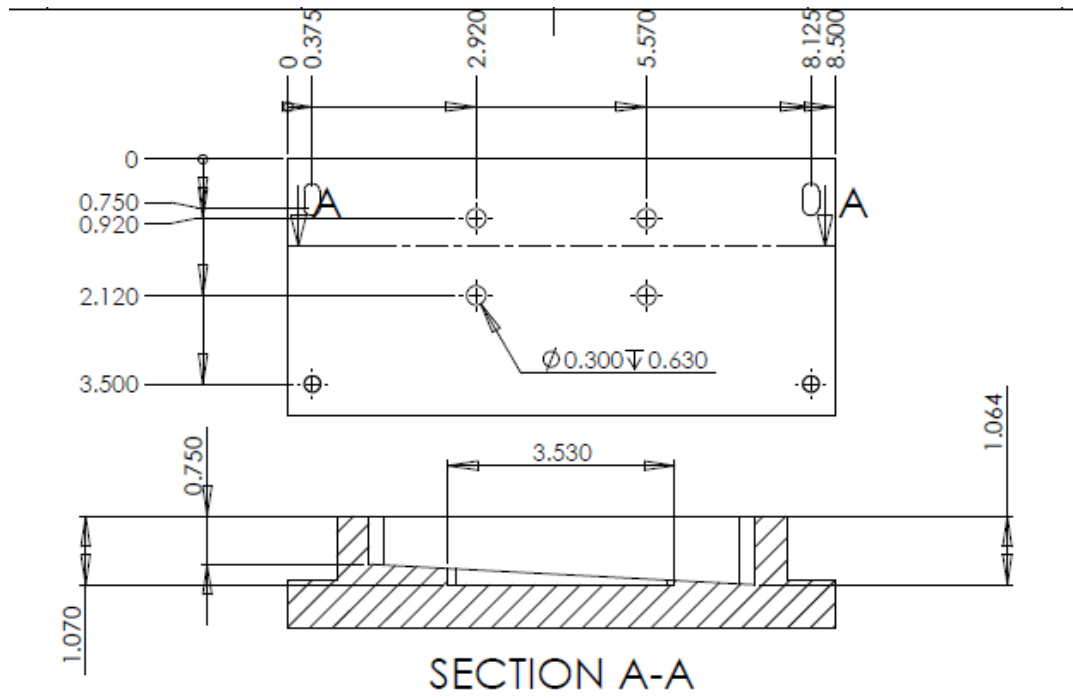


Figure 5.13: Over-flow container Dimensions

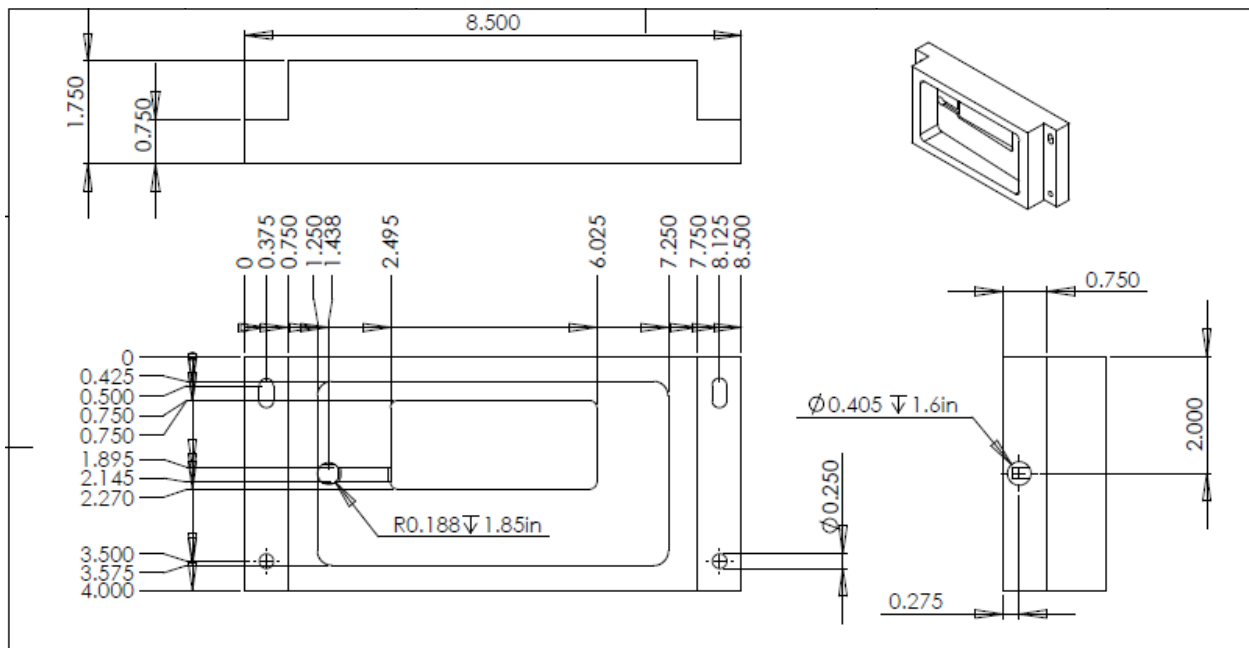


Figure 5.14: Over-flow container 3D view

5.3.3 The Jet Nozzle Holder

The jet nozzle holder is the part that connects to the nozzle of the tube coming from the reservoir. It allows for adjustment in the distance between the jet nozzle and the surface of the sample and secures the nozzle during the scanning motion.

First the jet nozzle holder has to be secured to the slider that allows for the linear motion of the nozzle. This is done by attaching it with acid resistant plastic screws fit through the clearance-holes on the jet nozzle holder and connected to threaded-holes on the slider as shown in Figure 5.15. Then we place the tube leading to the nozzle on the 45° track and secure it using the clamp and thumb screws going through the clearance holes on the clamp and threading into the base of the nozzle holder. The clamping mechanism prevents the tube from twisting or sliding on the track and provides a secure hold. This part is also made out of Noryl and is designed to have a minimum volume in order to reduce its weight.

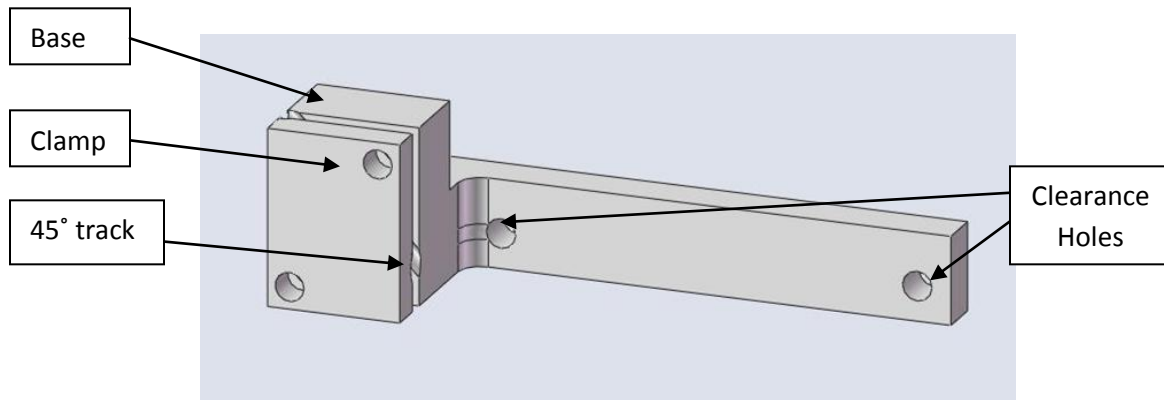


Figure 5.15: Jet nozzle holder 45°

In addition to a 45 degree track nozzle holder, we have also designed and machined a 90° track nozzle holder as seen in Figure 5.16 and Figure 5.17. We use it for potential testing of 90° jet experiments and also as a counterweight device for the revolving mechanism described below.

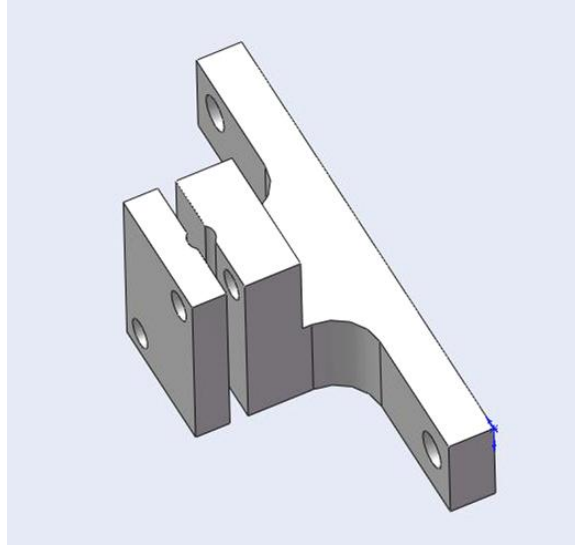


Figure 5.16: Jet Nozzle Holder 90°

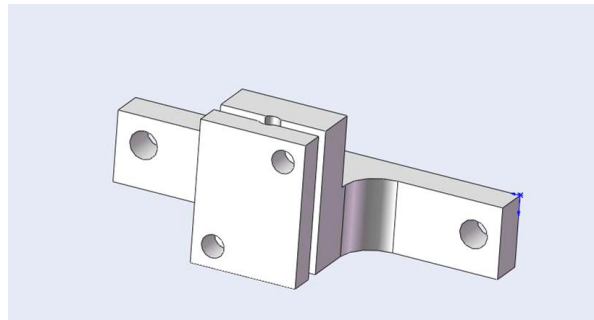


Figure 5.17: Jet Nozzle Holder 90°

5.3.4 The Revolving Mechanism

As a central piece of the jet etching apparatus, the revolving mechanism allows for the back and forth sweeping motion of the jet nozzle. As shown in Figure 5.18, the mechanism is composed of a rotating wheel attached to an electrical motor. The rotating wheel is connected through pins and flange bearings to two arms which drive the sliders on their track. As the slider moves, the jet nozzle holder nozzle moves accordingly, thus generating a linear motion of the jet nozzle relative to the sample.

The reason behind utilizing two sliders moving at the same time while we only use one at a time for jet etching purposes is to reduce vibrations on the system. As one slider moves to the right, the other moves to the left and vice-versa, this generates a symmetrical motion that results in counter acting

forces and moments which lead to a greater stability of the mechanism. Stability and vibration dampening is an important aspect of the mechanism from an experimental safety perspective. Since the acids involved in our experiment are considered hazardous chemicals, it is critical that we design a mechanical system that minimizes vibrations in order to prevent fluid from being ejected out of its designated container.

The moving parts of the system that will be seeing most stress are the arms, bearings, the wheel and the sliders. These parts are therefore machined out of metal in order to provide parts with high enough tensile strength and stiffness to withstand motion of the system. These parts are then covered with acid-resistant tape in order to prevent acid corrosion from acid vapors emerging from the acid bath.

The critical dimensions of the system are the radial distance of the pins connected to the wheel which are at a distance $r = 2.5\text{cm}$ from the center of the motor shaft and the length of the arms which is $L=11\text{ cm}$. The radial dimension of 2.5 cm was chosen to supply a total jet sweeping distance of 5 cm for a sample of maximum length of 1cm. The arm length of 11 cm was chosen as the corresponding arm length that offers a constant velocity of jet nozzle when it passes over the sample which corresponds to pin radial positions of $\pi/2$ and $3\pi/2$ as explained in Figure 5.4 in section 5.3.1.

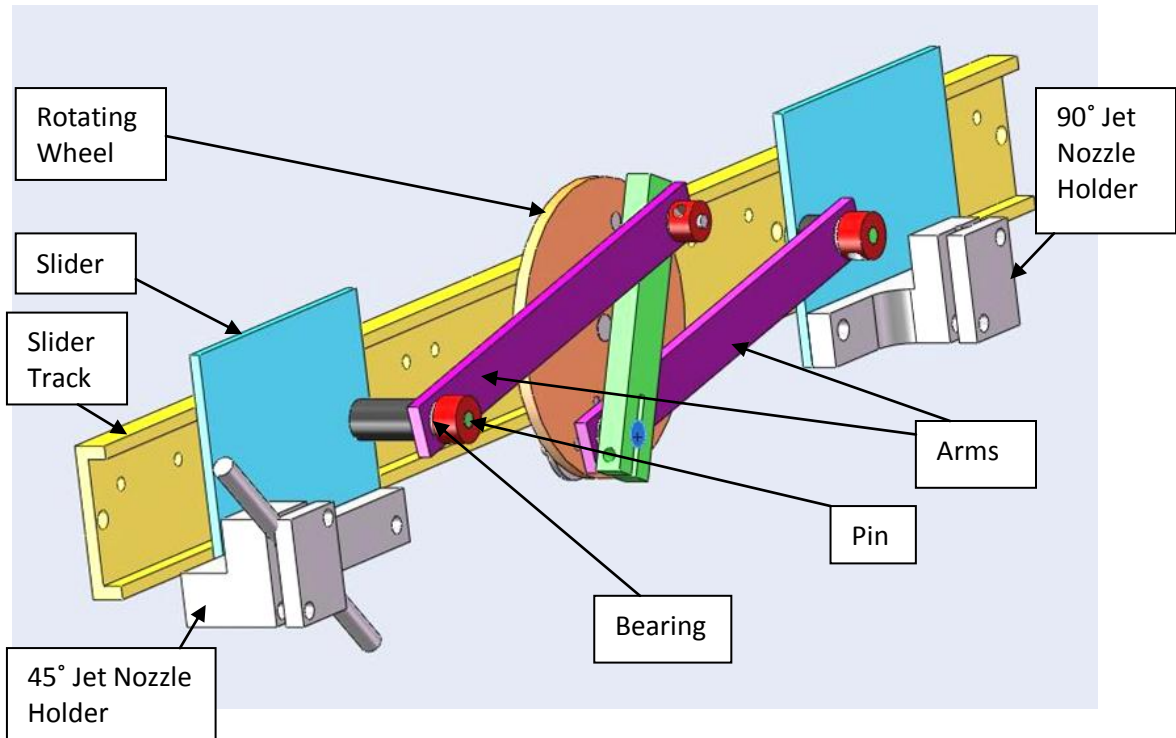


Figure 5.18: Revolving Mechanism

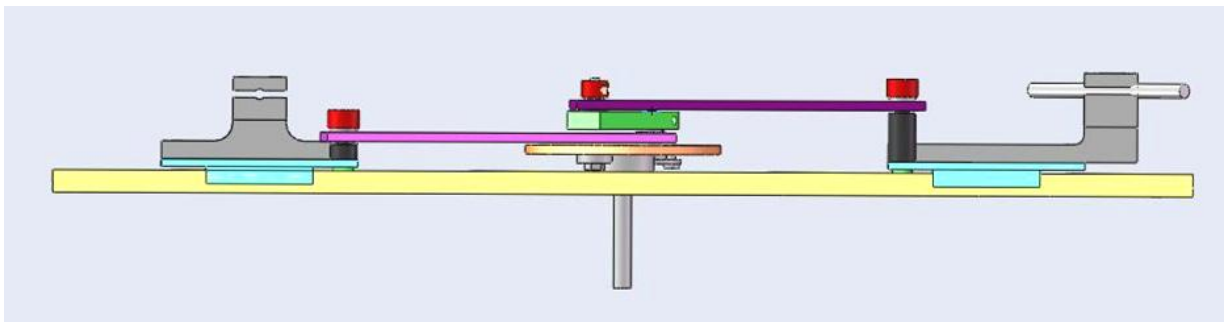


Figure 5.19: Revolving Mechanism – Top View

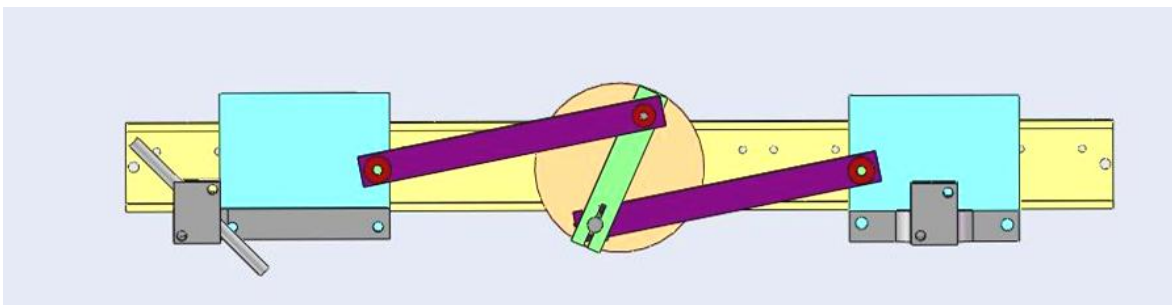


Figure 5.20: Revolving Mechanism – Front View

The revolving assembly is then affixed to the apparatus by attaching the slider to a back plate which serves both the purpose of holding the revolving mechanism in its appropriate location and providing a plenum for an air flow screen that prevent acid fumes from reaching and corroding the metal parts. Figure 5.21 shows a front view of the entire apparatus assembly. In this view, we can see the inclined bottom surface of the over-flow containers allowing to drain the fluid to the left side of the apparatus into a beaker. The back plate and plenum is more clearly shown in Figure 5.22. The plenum, shown in red, is covered with a flat plate of Noryl machined to hold a fitting leading to a compressed air feed.

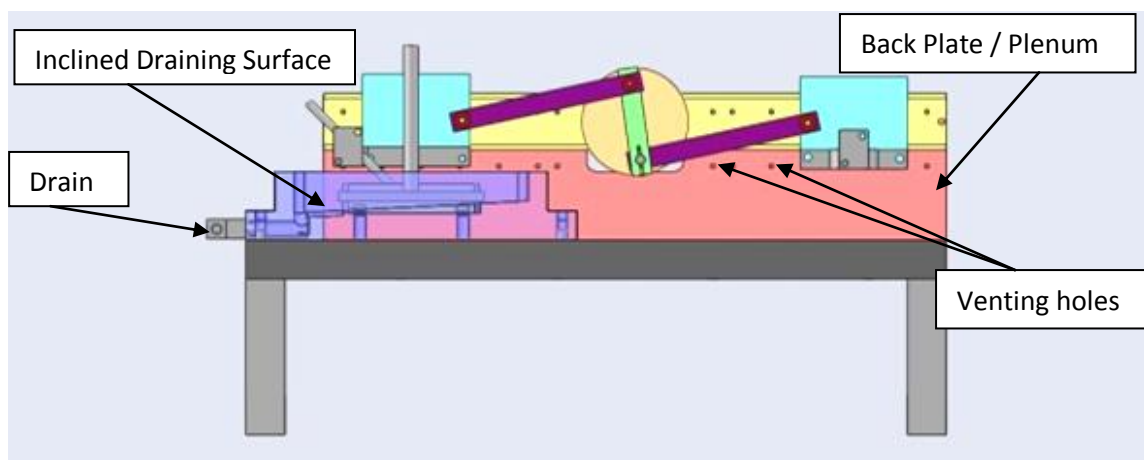


Figure 5.21: Apparatus Assembly

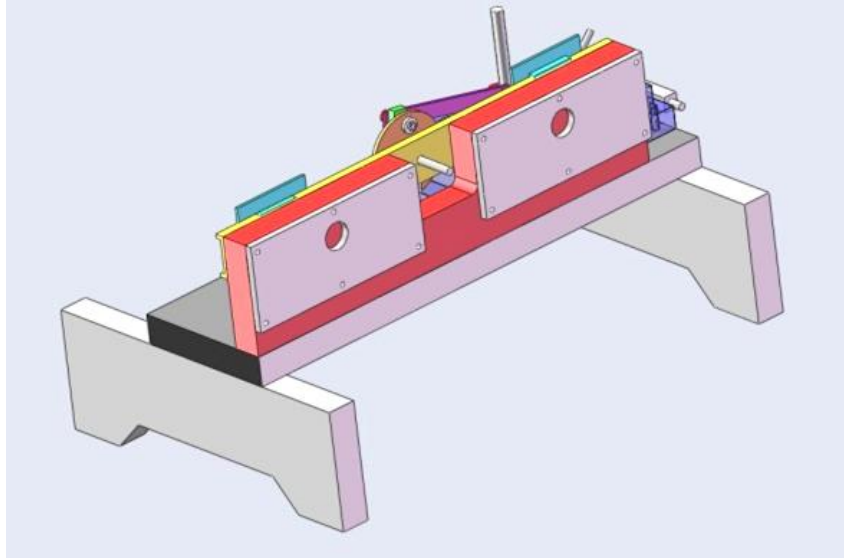


Figure 5.22: Apparatus Assembly - back view

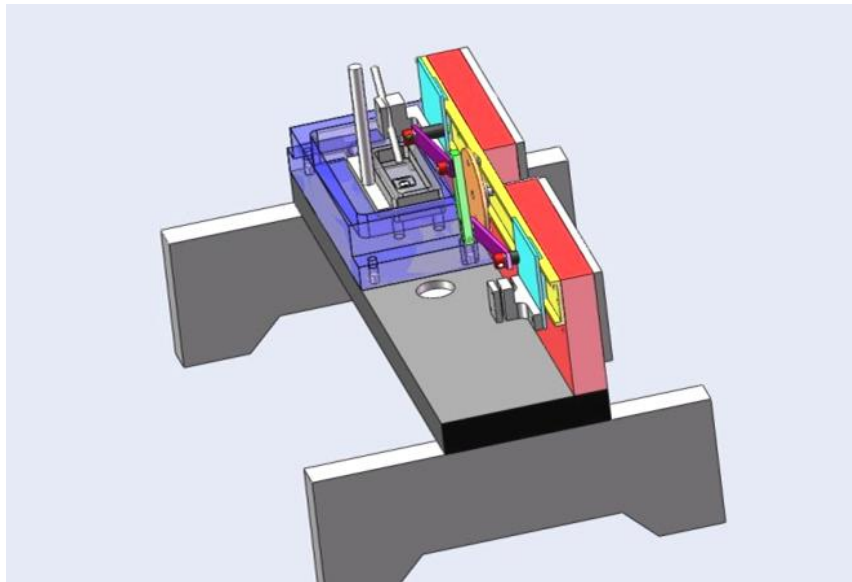


Figure 5.23: Apparatus Assembly

The cavity machined in the back of the plenum, as shown in Figure 5.24, is recessed 0.5 in from the back surface of the part. It is used to provide a chamber for the compressed air fed in through the fitting opening to reach an even pressure distribution before leaving the chamber through the venting holes. The back cover shown in Figure 5.26 seals the air chambers and provides a location for the air fitting.

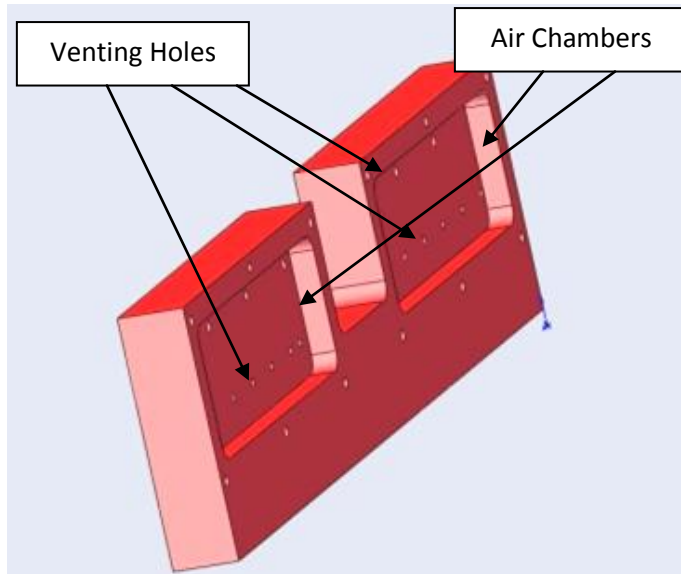


Figure 5.24: Back Plate / Plenum - Back View

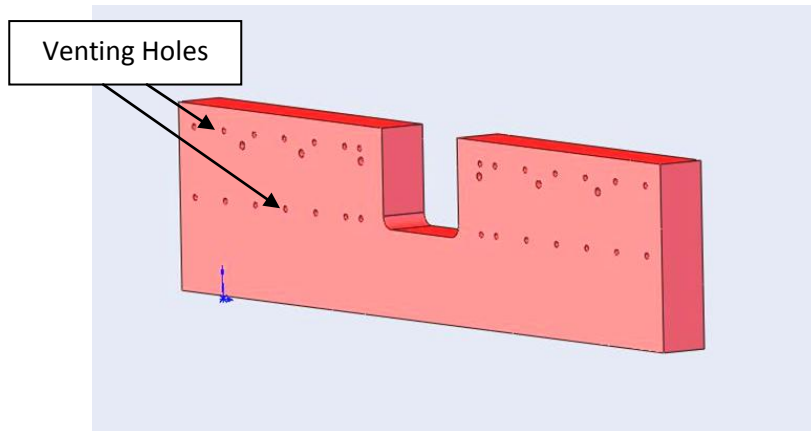


Figure 5.25: Back Plate / Plenum - Front View

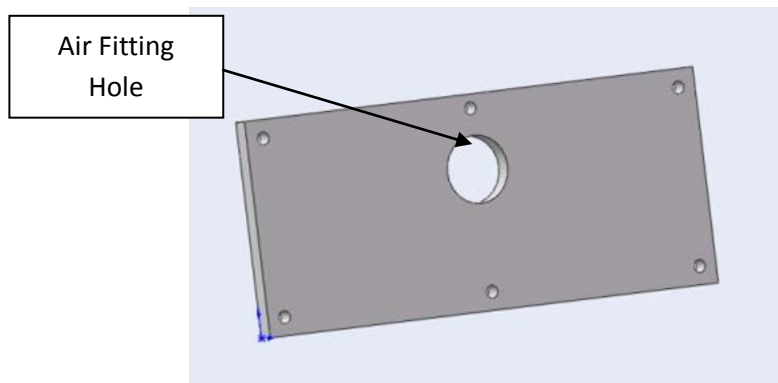


Figure 5.26: Plenum Back Cover

5.4 Technical Information on the Apparatus Operation

The motor driving the apparatus is a DC motor that has a rotational velocity of 6000 rpm at 24V. Using a gear head with ratio of 11.5 to 1, we calculate that the shaft driving the wheel spins at 521 rpm. The rotational velocity translates to a frequency of 8.7 Hz indicating that the jet nozzle would complete 8.7 cycles per second, where a cycle is defined as a back and forth linear motion. During each jet nozzle cycle, the nozzle scans the surface of the sample twice and therefore the sample experiences a jet etching effect with a frequency of 17.4 Hz. We should note that we powered the motor at a voltage $V = 12V$ thus yielding a frequency of 8.7 Hz on the sample. This corresponds to the order of magnitude of time that it takes for the diffusion layer to reach a thickness of the order of the feature size we are seeking to achieve. The equation below relates the characteristic length of diffusion to the time of diffusion of the chemical species present in the HNA system

$$l^* = \sqrt{Dt}$$

Where: l^* is the characteristic length of diffusion, D is the diffusivity coefficient (in the order of $10^{-9} \text{ m}^2/\text{s}$) and t is the time of diffusion.

Noting that the characteristic length of the features we seek to achieve are in the order of $l^* = 10 \mu\text{m}$, we calculate an approximate diffusion time of $t = 0.1\text{s}$. This can be approximated to the time it takes for the diffusion barrier to reach a thickness of the order of the characteristic length l^* . Since the scan frequency of the jet is 8.7 Hz which corresponds to a period of $t_{\text{scan}} = 1/8.7 = 0.115\text{s}$, we can deduce that the jet nozzle scanning frequency is well matched to the time of build up of the diffusion barrier of the surface of the sample.



Figure 5.27: Apparatus Picture

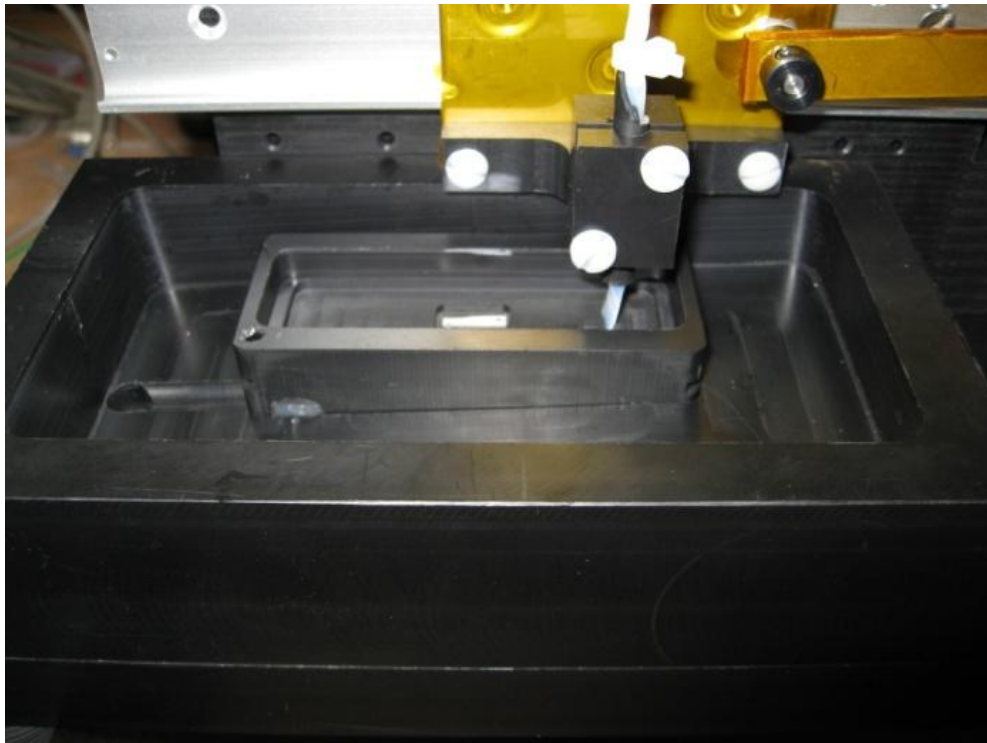


Figure 5.28: Apparatus Picture (view of sample holder and over-flow container)

Chapter 6 - Experiments and Results

Using the apparatus described in Chapter 5, we conduct experiments to determine the effect of jet etching on our desired light trapping features. In this chapter we present our results and discuss their meanings. We considered experiments using silicon substrates of $\langle 100 \rangle$, $\langle 110 \rangle$, $\langle 111 \rangle$ orientation and multi-crystalline silicon. We used different types of masking material and trench opening methods to adapt to various concerns as they arose. We used the same jet velocity for all experiments as discussed in section 5.2, where the jet velocity is about $V = 3$ m/s. The dimension of the nozzle opening are 5.0mm by 0.84mm.

6.1 Single Crystalline Silicon and Photo-Resist Mask.

6.1.1 Single Si $\langle 100 \rangle$ + Photo-Resist + Stationary Jet

In this experiment, we evaluate the effect of a stationary jet on a sample of $\langle 100 \rangle$ mono-crystalline silicon, coated with a $2 \mu\text{m}$ thick layer of Shipley 1827 photo-resist as shown in Figure 6.1. In addition to masking the desired surfaces, the function of the photo-resist is to provide a narrow opening through which the impinging fluid is constrained which raises its velocity at the opening and generates a local jet -effect.

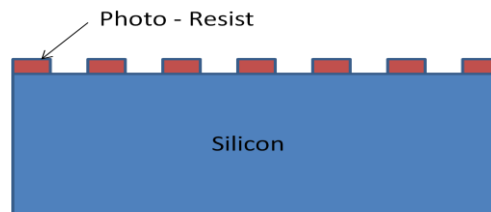


Figure 6.1: Silicon sample covered with a pattern photo-resist mask.

The sample was etched with the following specifications:

Process Description	Process Characteristic
Jet Etch	Yes

Photo-Resist	Shipley 1827, t= 2um
Etchant	11-2-4
Jet Angle	45 degree
Etching time	15s

Table 6.1: Experiment Condition for a jet etched <100> Si + PR sample

The etchant used in this experiment: 11:2:4, has been determined to be the acid composition that achieves the highest degree of isotropy in <100> silicon as discussed in section 5.1. The etch time was determined by etching similar samples for different etch times. The etch time yielding an adequate etch (neither over-etched nor under-etched) was the one selected. This is the case for all experiments performed in this section.

The theoretical aspect ratio for isotropic etching is A.R. = 0.5, which is a result of perfect semicircular features. Therefore any aspect ratio higher than 0.5 can be attributed, directly or indirectly, to the effect of the jet. In this experiment, aspect ratios up to 0.54 were achieved, indicating the positive effect of the jet (see Figure 6.2).

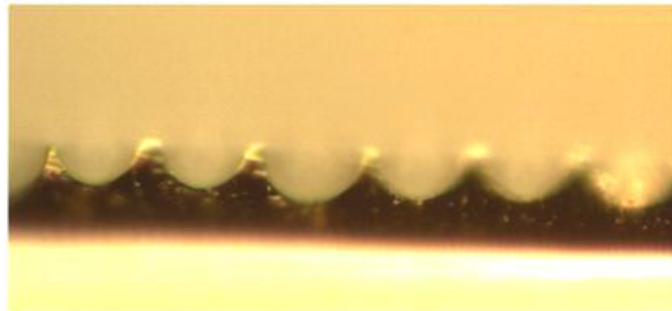


Figure 6.2: Si <100> + PR + Jet etch (AR = 0.62, Q = 0.277)

According to our trench cross-section evaluation method, the quality of the light trapping features is evaluated based on its aspect ratio and the quality of its curvature. In this experiment, the achieved aspect ratio is 0.62 and the quality is Q =0.277. This indicates that the jet resulted in an increase in aspect ratio and compared to a sample that is not etched with a jet.

A control experiment was conducted in order to confirm the effect of the jet. It consists of etching a sample of <100> coated with a Shipley 1827 photo-resist mask in a bath of 11:2:4 acids of the same composition with no jet and no agitation as summarized in the table below:

Process Description	Process Characteristic
---------------------	------------------------

Jet Etch	No
Photo-Resist	Shipley 1827, t = 2 μm
Etchant	11-2-4
Jet Angle	N/A
Etching time	39s

Table 6.2: Experiment Conditions for an Si sample of <100> orientation etched with no jet.

The agitation time has been determined by etching multiple samples of Shipley-coated <100> Silicon sample at increasing etch times and observing under microscope the extent of the completion of the etch. The etch time associated with an adequately etched sample was the one used for the control experiment. The resulting aspect ratio and quality from this experiments are A.R. = 0.359 and Q = 0.3356 as shown in Figure 6.3. Clearly, the aspect ratio in the control sample is lower than the one in the jet etched sample and its quality is lower (smaller Q is better) as summarized in the table below:

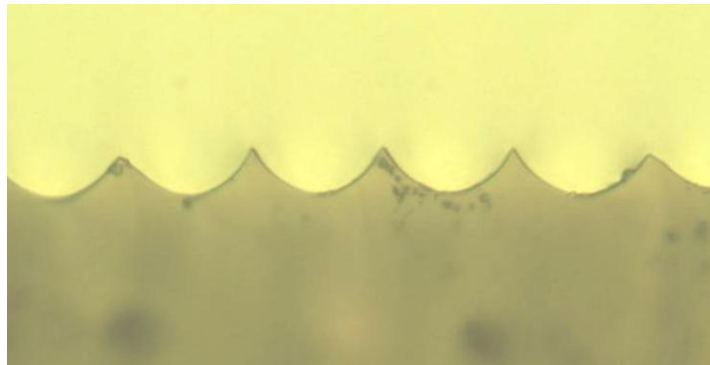


Figure 6.3: <100> Si + PR control experiment (AR = 0.359, Q = 0.3356)

	<100> Q	<100> AR
Control	0.3356	0.359
Jet	0.277	0.62
Quantitative Comparison	17.46%	50.4178%

Table 6.3: Experiment Result Summary for <100> Si+PR

This first attempt of jet etching, using a stationary nozzle jet apparatus, suggests that the jet is capable of increased aspect ratios, which increases the light trapping ability of the trenches according to the detector hits chart in Figure 2.2.

Observations from this series of experiments indicate that the PR mask lifts off prematurely (i.e. before the completion of the etching process) due to the relatively high jet velocity impinging on it. This undermines the etching process since the masked surfaces are etched and the desired morphology is compromised. To address this issue, we investigate next the jet behavior with the presence of a hard mask.

Additionally, we observe the presence of an increased etch rate at the location where the jet enters in contact with the sample. This leads to an over-etching of the portion of the sample that is situated in proximity of the jet. To compensate for this event, we use the moving jet apparatus in which the jet nozzle moves parallel to the surface of the sample in a back and forth sweeping motion as Figure 6.4 below shows.



Figure 6.4: Moving Jet Nozzle Apparatus

6.2 Silicon + Oxide mask + Photo-Resist

This set of experiments was performed using an oxide mask as a complement to a photo-resist mask to compensate for photo-resist mask lift off. When the mask is lifted off early (within the first few seconds of the etching process), the local jet effect is no longer achieved and the resulting features are not desirable. Adding a hard mask between the substrate and the photo-resist will maintain the shape of the mask opening and further help determine the effect of the jet on the trench etching.

The process of forming the silicon oxide layer (SiO_2) consists of growing it from the silicon substrate through oxidation in high temperature (1100 C) in air or water vapor (dry or wet oxide) for a period of about 18hr for dry SiO_2 and 11hr for wet SiO_2 . The resulting oxide layer was measured to be $1.5 \mu\text{m} < t_{\text{SiO}_2} < 1.8 \mu\text{m}$.

Next, we pattern a Shipley 1827 photo-resist mask on the SiO_2 layer as shown in Figure 6.5, which serves to duplicate the desired pattern on the SiO_2 layer itself. Doing so requires etching the silicon oxide exposed through the photo-resist mask opening without etching the silicon substrate under it. For this purpose we use a 1:1 hydrofluoric acid and water solution with a concentration of 49% which etches away the oxide layer without affecting the silicon layer underneath. Figure 6.6 shows the resulting pattern with an opened layer of oxide covered with photo-resist. This sample is then etched in the HNA solution selected above (11:2:4).



Figure 6.5: Diagram of silicon substrate covered with hard SiO_2 mask and patterned photo-resist layer

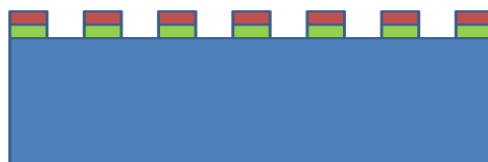


Figure 6.6: Diagram of Silicon substrate covered with hard SiO_2 and Photo-Resist after opening

6.2.1 Single Si + Photo-Resist + Oxide <100>

In order to verify the effect of the oxide mask, we first duplicate the experiment of etching a <100> silicon sample without a jet (control) and then with a jet. The experiment conditions are summarized in Table 6.4 and Table 6.5 below.

Process Description	Process Characteristic
Jet Etch	No
Mask	Shipley 1827 + SiO ₂
Etchant	11-2-4
Hard Mask Opening Solution	HF: H ₂ O (1:1)
Jet Angle	N/A
Etching time	2 min 30s ³

Table 6.4: Experiment conditions for <100> + SiO₂ + PR – No jet

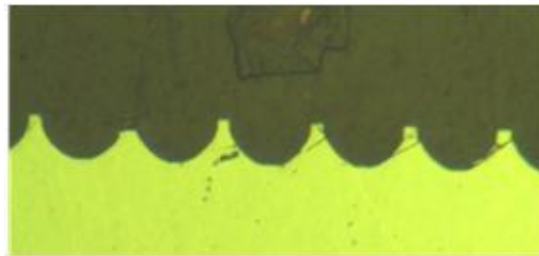


Figure 6.7: Control Experiment for <100> + SiO₂ + PR (AR = 0.49, Q = 0.3152)

Process Description	Process Characteristic
Jet Etch	Yes - Moving
Mask	Shipley 1827 + SiO ₂
Hard Mask Opening Solution	HF : H ₂ O (1:1)
Etchant	11:2:4
Jet Angle	45 degree
Etching time	10s

Table 6.5: Experiment conditions for <100> + SiO₂ + PR – with jet

³ The extended etch time of 2min30s is much longer than the required etch time of 45s in this case. This can be explained by the fact that the 1:1 HF:H₂O solution does not fully open the oxide mask sometimes. Therefore longer etch times are needed for the 11:2:4 etching solution to open the remaining oxide layer, then etch through the silicon as desired.

After the opening the SiO₂ mask with HF:H₂O (1:1), the sample was placed under the moving jet apparatus and jet etched for 10s. The picture below shows the resulting trench shape, which has an aspect ratio: AR = 0.5465 and a quality of 0.2731.

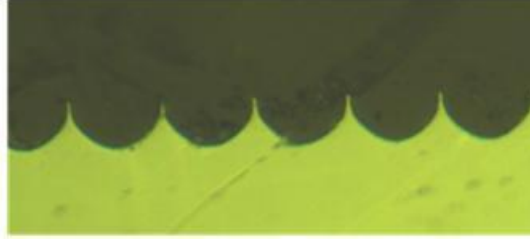


Figure 6.8: <100> + SiO₂+PR Jet etched (AR = 0.54, Q = 0.273)

	<100> Q	<100> AR
Si+ SiO ₂ + PR	Q	AR
Control	0.3152	0.49
Jet	0.2731	0.54
Quantitative Comparison	-0.133566	0.102041

Table 6.6: Experiment Result Summary for Si + SiO₂ + PR

Comparing the two experiments conducted above and summarized in Table 6.6, we can conclude that the jet has the effect of increasing the aspect ratio of the parabolic feature beyond the control sample aspect ratio (0.49) and especially beyond the theoretical aspect ratio of an isotropic etch which is an aspect ratio of 0.5. Additionally, the quality of the achieved trenches is improved as well by about 13% suggesting that the jet results in features with improved light trapping ability. This complementary dual effect of the jet is desirable in our main goal of achieving higher light trapping capability in the surface of the solar cell.

The effect of the hard mask is dual fold. First, we can see that the SiO₂ mask does not lift off and therefore successfully serves the role of providing a fixed opening for the local jet effect. Indications of the local jet effect lie in the fact that the aspect ratios achieved are higher than 0.5 which means that the etching fluid is etching preferentially down the vertical direction and fresh etchant is reaching the bottom of the trench in priority. This indicates that the local jet effect does take place. Second, the mask remaining in place is providing a resilient mask for surfaces that we would like to keep masked.

Additionally, the fact that the mask is composed of SiO₂ could potentially have an effect on the etch behavior regardless of the jet. As stated in section 2.3.1, the etching reaction involves two steps, oxidation and dissolution. Since the SiO₂ layer offers a reactant species for the dissolution reaction,

there could be a depletion of HF which would react with the SiO₂ in the mask rather than the SiO₂ in the trench. This local depletion of HF could potentially reduce the etch rate in the proximity of the mask while maintaining an elevated etch rate away from it. According to Robbins and Schwartz (18), the chemical composition 11:2:4 (by volume HNO₃:HC₂H₃O₂:HF) should etch at about 86 μm per minute, however our experiments show that it actually etches at about 15 μm per minute. If we assume the vicinity of the oxide mask to be the arc distance of trench that is as long as the over hang distance of the mask and which starts at the intersection of the mask and the trench, then the quantity of etchant located in this region would have to react with the bottom of the mask and the region of the trench in the vicinity of the mask. This would deplete the quantity of HF available in the etchant by a factor of 2, which would decrease the etch rate by a factor of 1.7 according to Robbins and Schwartz. A lower etch rate in the vicinity of the mask would result in close to vertical side walls. This would explain why the control experiment in this case has a much higher aspect ratio than the control experiment without the oxide mask (0.49 vs 0.359), since the trenches top opening would etch slower than the rest as Figure 6.9 suggest. Also the resulting vertical walls also indicate that the etch rate is slower closer to the mask than further away from it. For vertical sidewall to result from a horizontal opening, etch rates have to increase as we move away vertically from the top surface towards the bottom, which indicates that in the SiO₂ mask's vicinity the etch rates are lower.

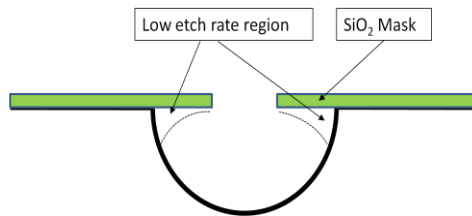


Figure 6.9: SiO₂ Mask effect on local etching. Regions in the vicinity of the mask are etched slower which result in more vertical side-wall.

Having obtained positive results with a sample of single crystalline silicon of orientation <100>, we move on to evaluate the effect of the jet on other orientations such as <111> and <110>, in order to further investigate the jet etching effect on other crystal orientations.

6.2.2 Single Si <111> + Photo-Resist + Oxide

As mentioned in section 5.1, the process of selecting an HNA composition with the highest degree of isotropy has been conducted using single crystalline sample with <100> orientation. The

composition yielding a trench cross-section that is the closest to a semi-circular shape was the selected composition of 11:2:4. We now evaluate the behavior of this solution and its jetting on <111> and <110> samples with an oxide mask.

We run similar experiments for single crystal silicon of orientation <111> and <110> as in the previous section. After growing a SiO₂ layer from the substrate surface through wet or dry oxidation at 1100°C, we pattern the oxide layer using a Shipley 1827 photo-resist mask and a concentrated solution of 1:1 HF: H₂O.

Process Description	Process Characteristic
Jet Etch	No
Mask	Shipley 1827 + SiO ₂
Hard Mask Opening Solution	HF : H ₂ O (1:1)
Etchant	11:2:4
Jet Angle	N/A
Etching time	35s

Table 6.7: Experiment Conditions for <111> Si + SiO₂+PR – Control

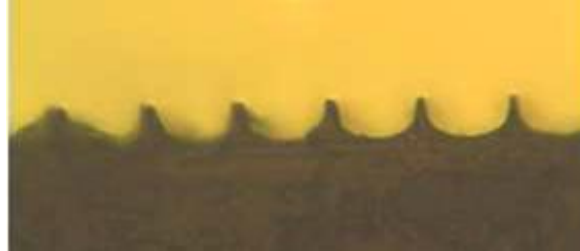


Figure 6.10: <111> Si + SiO₂ +PR – Control (AR = 0.479, Q = 0.5297)

Process Description	Process Characteristic
Jet Etch	Yes - moving
Mask	Shipley 1827 + SiO ₂
Hard Mask Opening Solution	HF : H ₂ O (1:1)
Etchant	11:2:4
Jet Angle	45
Etching time	10s

Table 6.8: Experiment Conditions for <111> Si + SiO₂ + PR - with Jet

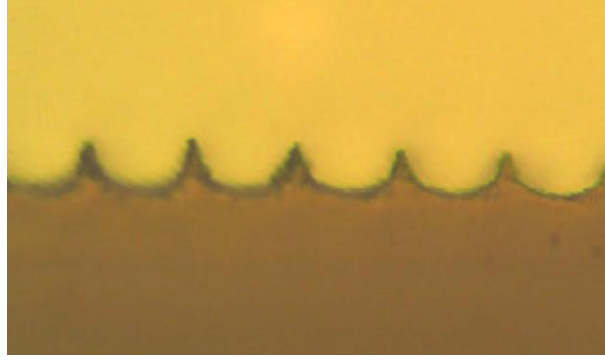


Figure 6.11: $\langle 111 \rangle$ Si + SiO₂ + PR - with jet (AR = 0.422, Q = 0.4598)

	$\langle 111 \rangle$	$\langle 111 \rangle$
Si+ SiO ₂ + PR	Q	AR
Control	0.5297	0.479
Jet 1	0.4598	0.422
Quantitative Comparison 1	-0.131961	-0.119

Table 6.9: Experiment Summary for $\langle 111 \rangle$ Si + SiO₂+PR

Results from this experiment show cross-sectional shapes that are not circular or parabolic in nature. This suggests that the etching fluid is not etching at the same rate in all directions. Figure 6.10, shows that the trenches have flat bottoms and steep vertical wall, which is not favored for light trapping. This indicates that the composition 11:2:4 is not suited for etching single Si with $\langle 111 \rangle$ orientation.

Nonetheless, we can still evaluate the impact of the jet on the etching process by observing that the trenches have overall better quality when jet etched, even if their aspect ratio deteriorates. Note the inconsistency of this result with previous experiments, which undermines the indication that jet etching results in higher quality light trapping features. However, the results are not to be taken as disqualifying since the etching solution is not optimized for this crystal orientation.

6.2.3 Single Si $\langle 110 \rangle$ + Photo-Resist + Oxide

We conduct similar experiments with $\langle 110 \rangle$ silicon as per the information below.

Process Description	Process Characteristic
---------------------	------------------------

Jet Etch	No
Mask	Shipley 1827 + SiO ₂
Hard Mask Opening Solution	HF : H ₂ O (1:1)
Etchant	11:2:4
Jet Angle	N/A
Etching time	30s

Table 6.10: Experiment Conditions for <110> Si + SiO₂ + PR – Control

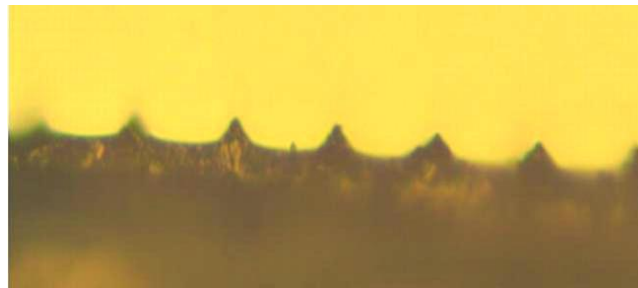


Figure 6.12: <110> Si + SiO₂ + PR – Control (AR = 0.2178, Q = 0.6247)

Process Description	Process Characteristic
Jet Etch	Yes - Moving
Mask	Shipley 1827 + SiO ₂
Hard Mask Opening Solution	HF : H ₂ O (1:1)
Etchant	11:2:4
Jet Angle	45°
Etching time	10s

Table 6.11: Experiment Conditions for <110> Si + SiO₂ + PR

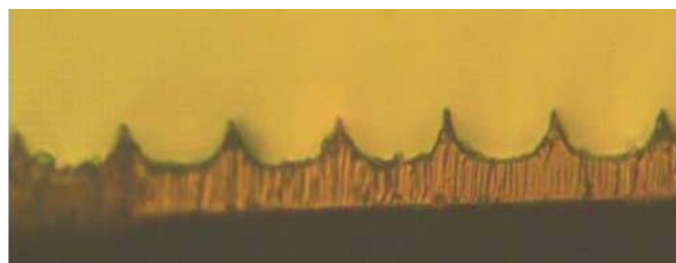


Figure 6.13: <110> Si + SiO₂ + PR - with Jet (AR = 0.3598, Q = 0.615)

	<110>	<110>
Si+ SiO ₂ + PR	Q	AR
Control	0.6247	0.2178
Jet	0.615	0.3598
Quantitative Comparison	-0.015527	0.651974

Table 6.12: Experiment Summary for <110> Si + SiO₂ + PR

For a single crystal silicon of orientation <110>, we observe a significant increase in aspect ratio and a small improvement in trench quality between the control sample and the jet etched one. This indicates that the jet can significantly increase aspect ratios in <110> silicon which is consistent with results in <100> silicon.

However, we can observe again by looking at Figure 6.12 and Figure 6.13 that the cross-sections of the trenches are not semi-circular or parabolic in nature. This further supports the observation that the 11:2:4 is not an isotropic etchant in crystal orientations other than <100>. Given this disadvantage, it becomes difficult to evaluate the effect of the jet in all crystal orientations. However, for experimentation consistency, we continue to use 11:2:4 for all experiments and attempt to evaluate the effect of jet etching on multi-crystalline silicon.

6.2.3 Multi Si + Photo-Resist + Oxide + Jet

Having investigated the effect of the jet on single crystal silicon substrates and having obtained encouraging indications of increased aspect ratios for the desired trench, we now investigate the effect of the jet on a substrate of multi-crystalline silicon using the same apparatus and the same etching solution.

Similarly to the single crystal silicon experiments above, the multi-crystalline experiment consists of a multi-crystalline silicon substrate that has been damage etched and processed for SiO₂ layer growth and then patterned in a photo-resist mask of a thickness of 2 μm enabling the desired features.

Again, we run a control sample consisting of etching in 11:2:4 without a jet for 45 seconds as shown in Figure 6.14 and a jetted sample shown in Figure 6.15. The etching time were determined by

etching samples for different times and observed the result under microscope. We selected the etch time of the sample with the most complete etch.

The process characteristics of the experiment are summarized in the table below.

Process Description	Process Characteristic
Jet Etch	No
Mask	Shipley 1827 + SiO ₂
Hard Mask Opening Solution	HF : H ₂ O (1:1)
Etchant	11:2:4
Jet Angle	N/A
Etching time	45s

Table 6.13: Experiment Conditions for multi-Si + SiO₂+ PR – Control

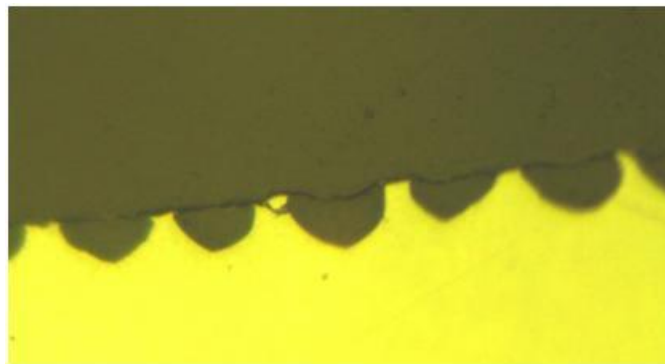


Figure 6.14: Multi-Si + SiO₂ + PR – Control (AR = 0.5722, Q = 0.1359)

The jet etching time was determined using the same method as above, an etch time of 10 seconds was found to be the most appropriate.

Process Description	Process Characteristic
Jet Etch	Yes - Moving
Mask	Shipley 1827 + SiO ₂
Hard Mask Opening Solution	HF : H ₂ O (1:1)
Etchant	11:2:4
Jet Angle	45
Etching time	10s

Table 6.14: Experiment Conditions for multi-Si + SiO₂+PR - with Jet

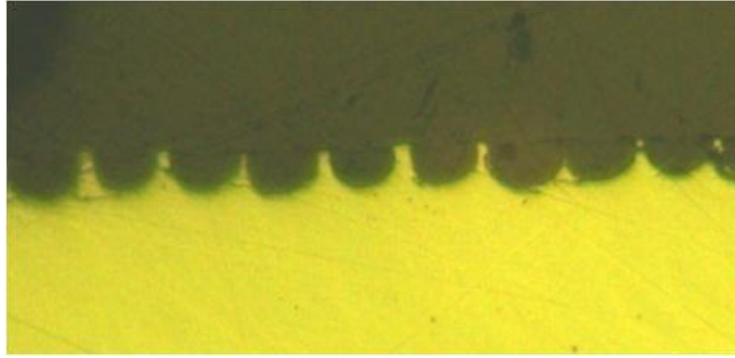


Figure 6.15: Multi-Si + SiO₂ + PR - with Jet (AR = 0.5316, Q = 0.4373)

	multi-Si	multi-Si
multi Si+ SiO ₂ + PR	Q	AR
Control	0.1359	0.5722
Jet	0.4373	0.5316
Quantitative Comparison	2.217	-0.070

Table 6.15: Experiment Summary for multi-Si + SiO₂+PR

We can see from Table 6.15: Experiment Summary for multi-Si + SiO₂+PR Table 6.15 above that the jet etching process does not have a positive impact on this sample of multi-crystalline silicon. The quality of the trenches worsens and the A.R. is reduced indicating that the jet has a negative effect on multi-silicon. However we notice that the jet increases the uniformity of the profiles of the trench. In Figure 6.14, we can see that the trenches are etched to different depths and with non uniform shapes. In contrast, Figure 6.15, which shows the jet etched sample, depicts a greater uniformity between the trenches. Finally, we noticed that the surface of the sample before etching in 11:2:4 was already patterned from the saw damage removal etch. The SiO₂ mask's shape shows the initial curvature of the surface of the substrate before etching. This surface curvature could have altered our results and could have increased the measured aspect ratios beyond what they could have been if the surface of the sample was flat. To verify this we perform the same experiment as above with a polished multi-crystalline wafer.

6.2.4 Polished multi-crystalline Silicon + Photo-Resist + SiO₂

Given that the results obtained from the previous experiment with multi-crystalline silicon were possibly altered by the saw damage removal etch pattern remaining on the surface of the sample. We perform the same experiment with polished multi.

Process Description	Process Characteristic
Jet Etch	No
Mask	Shipley 1827 + SiO ₂
Hard Mask Opening Solution	HF : H ₂ O (1:1)
Etchant	11:2:4
Jet Angle	N/A
Etching time	35s

Table 6.16: Experiment Conditions for Polished Multi Si + SiO₂ + PR

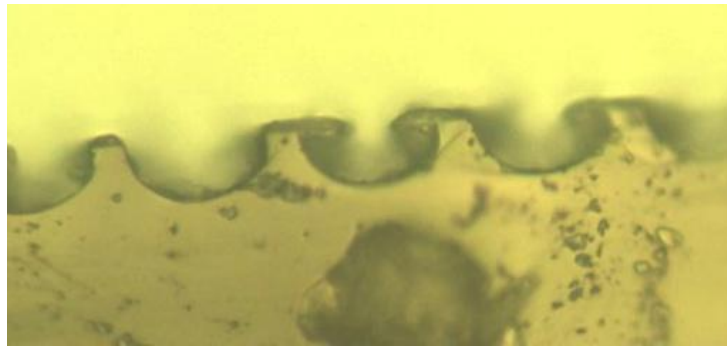


Figure 6.16: Polished Multi + SiO₂+ PR - Control (AR = 0.4398, Q = 0.4039)

Process Description	Process Characteristic
Jet Etch	Yes - Moving
Mask	Shipley 1827 + SiO ₂
Hard Mask Opening Solution	HF : H ₂ O (1:1)
Etchant	11:2:4
Jet Angle	45
Etching time	10s

Table 6.17: Experiment Conditions for Polished Multi + SiO₂ + PR - with Jet

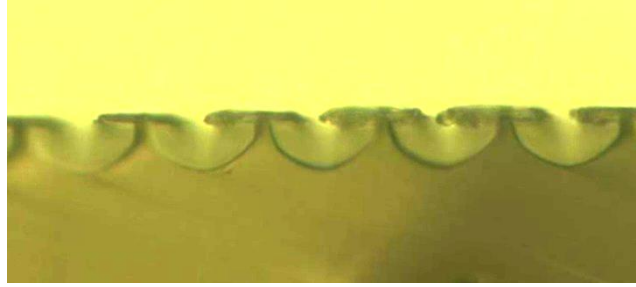


Figure 6.17: Polished Multi - Si + SiO₂ + PR + Jet (AR = 0.4796, Q = 0.3170)

	Polished multi-Si	Polished multi-Si
Polished multi Si+ SiO ₂ + PR	Q	AR
Control	0.4039	0.4398
Jet	0.3170	0.4796
Quantitative Comparison	-0.215	0.090

Table 6.18: Experiment Summary for Polished Multi-Si + SiO₂ + PR

The results obtained from the experiments with polished multi crystalline silicon sample are more aligned with previous results obtained previously for single crystal silicon. We can see in Table 6.18 that the jet increased the aspect ratio of the trenches as well as improved their quality (by decreasing the measured Q-factor). Given that a polished surface of multi-crystalline silicon is free of surface patterns that result from saw damage removal, we can consider the results obtained in this section as more reliable than the results we have observed in the non-polished multi crystalline silicon section. Once again we observe a positive effect from the jet which further confirms results obtained in previous experiments.

6.3 Silicon + Oxide mask + PR (BOE Opening)

A main concern about using a solution of HF:H₂O 1:1 is the fact that it caused an early lift off of the photo-resist mask during the process of opening the oxide layer. The duplication of the photo-resist mask pattern was therefore under the risk of being compromised. The concern is that the opening of the oxide layer mask would be larger than the PR mask due to early PR lift off. This would in turn cause a worsening of the trench quality since the initial flat region would have a tendency to remain flat during

the etching process. This would result in a larger portion of flat region in the bottom of the trench which is undesirable. Another concern is that the required etch time for the concentrated HF solution to etch through the thermally grown oxide was not consistent, which made it difficult to determine when the oxide layer was fully opened.

We turned to buffered oxide etch (BOE) for a better etch control. A 5:1 BOE solution etches at a rate of about 100 nm per min (28), which indicates that the oxide layer of thickness of about 2 μm would take about 20 minutes to etch. Our method of opening the oxide layer was done with progressive BOE etch and inspection: we first etch for 10 minutes then verify if the mask has opened by observation under microscope. Once the oxide mask is opened we proceed to etch the sample. Using BOE allows for the PR to remain in place and for the oxide mask to be a close duplicate of the PR pattern.

We proceed to etch samples of <100>, <110> and <111> with a thermally grown oxide layer opened using buffered oxide etch.

6.3.1 Silicon + Oxide + PR + BOE : <100> Si

Process Description	Process Characteristic
Jet Etch	No
Mask	ShIPLEY 1827 + SiO ₂
Hard Mask Opening Solution	BOE
Etchant	11:2:4
Jet Angle	N/A
Etching time	35s

Table 6.19: Experiment Conditions for <100> Si + SiO₂+PR + BOE - Control



Figure 6.18: <100> Si + SiO₂ + PR + BOE – Control (AR = 0.3059, Q = 0.2238)

Process Description	Process Characteristic
Jet Etch	Yes - Moving
Mask	ShIPLEY 1827 + SiO ₂

Hard Mask Opening Solution	BOE
Etchant	11-2-4
Jet Angle	45
Etching time	13s

Table 6.20: Experiment conditions for <100> Si + SiO₂+PR + BOE - with Jet

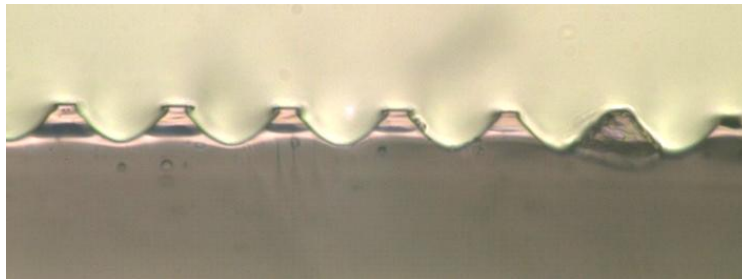


Figure 6.19: <100> Si + SiO₂ + PR + BOE - with Jet (AR = 0.4, Q = 0.228)

The resulting aspect ratios and quality factors are summarized below:

	<100>	<100>
Si+ SiO ₂ + PR + BOE	Q	AR
Control	0.2238	0.3059
Jet	0.228	0.4
Quantitative Comparison	0.0187	0.3076

Table 6.21: Experiment Summary for <100> Si + SiO₂+ PR+ BOE

Results from this experiment confirm that in <100> silicon the effect of the jet is to significantly improve the aspect ratio of the trenches. In this case it was improved by about 30.8%. Additionally, the quality of the trench, while it was not improved, remained at high quality compared to all other experiments ran and compared to a theoretical limit of Q = 0.1476. Additionally, the BOE offered more repeatable results than previous processes.

6.3.2 Silicon + Oxide + PR + BOE : <110> Si

We evaluate in this experiment the effect of jet etching on a silicon sample of <110> orientation. We conduct the same process as above.

Process Description	Process Characteristic
Jet Etch	No
Mask	Shipley 1827 + SiO ₂
Hard Mask Opening Solution	BOE
Etchant	11:2:4
Jet Angle	N/A
Etching time	40s

Table 6.22: Experiment conditions for <110> Si+ SiO₂+PR+BOE – Control

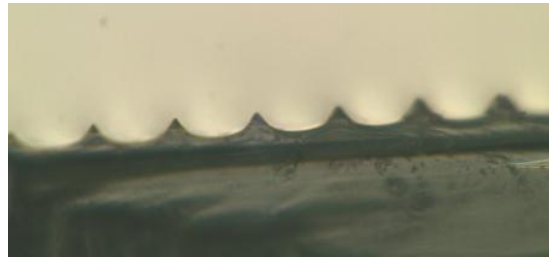


Figure 6.20: <110> Si + SiO₂+ PR + BOE – Control (AR = 0.2751, Q = 0.54)

Process Description	Process Characteristic
Jet Etch	Yes - Moving
Mask	Shipley 1827 + SiO ₂
Hard Mask Opening Solution	BOE
Etchant	11-2-4
Jet Angle	45°
Etching time	10s

Table 6.23: Experiment conditions for <110> Si + SiO₂+ PR+BOE - with Jet

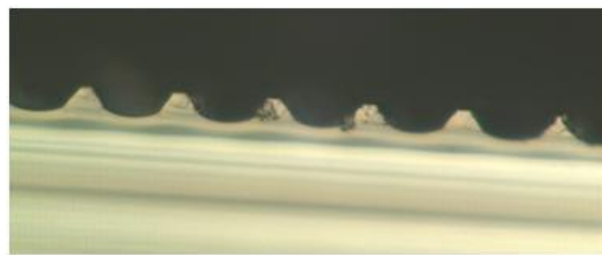


Figure 6.21: <110> Si + SiO₂ + PR + BOE - with Jet (AR= 0.3395, Q = 0.4995)

	<110>	<110>
Si+ SiO ₂ + PR + BOE	Q	AR
Control	0.54	0.2751
Jet	0.4995	0.3395

Quantitative Comparison	-0.075	0.234097
-------------------------	--------	----------

Table 6.24: Experiment Summary for <110> Si + SiO₂ + PR

Results for this experiment show again that the jet has the effect of significantly increasing aspect ratio for trenches etched in <110> Si by about 23.4 % and contribute to increasing the quality of the trenches by 7.5%. This result is consistent with previous findings for <110> jet etching experiment.

6.3.3 Silicon + Oxide + PR + BOE : <111> Si

Process Description	Process Characteristic
Jet Etch	No
Mask	Shiplely 1827 + SiO ₂
Hard Mask Opening Solution	BOE
Etchant	11:2:4
Jet Angle	N/A
Etching time	40s

Table 6.25: Experiment Conditions for <111> Si + SiO₂+PR+BOE – Control

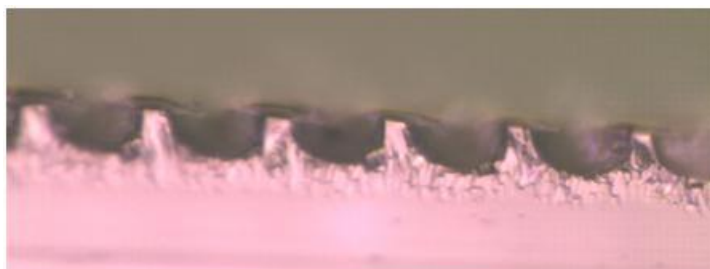


Figure 6.22: <111> Si + SiO₂ + PR + BOE – Control (AR = 0.4434, Q = 0.4705)

Process Description	Process Characteristic
Jet Etch	Yes- Moving
Mask	Shiplely 1827 + SiO ₂
Hard Mask Opening Solution	BOE
Etchant	11:2:4

Jet Angle	45°
Etching time	10s

Table 6.26: Experiment Conditions for <111> Si + SiO₂ + PR + BOE - Jet

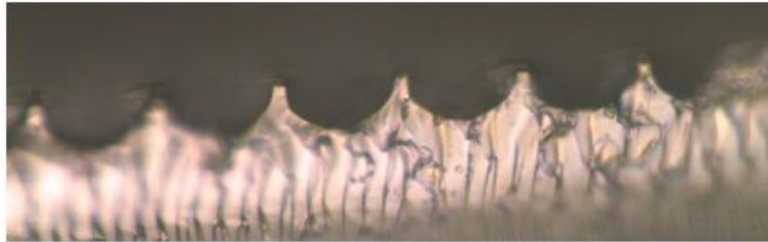


Figure 6.23: <111> Si + SiO₂ + PR + BOE - with Jet (AR = 0.4412, Q = 0.291)

	<111>	<111>
Si+ SiO ₂ + PR + BOE	Q	AR
Control	0.4705	0.4434
Jet	0.291	0.4412
Quantitative Comparison	-0.381509	-0.005

Table 6.27: Experiment summary for <111> Si + SiO₂ + PR + BOE

This experiment shows that while the jet does not have an effect on the aspect ratio of the trenches it significantly increases their quality in <111> silicon, which corroborates findings in section 6.2.2 for previous experiments in <111>.

We now summarize all the results of BOE experiments in Table 6.28 below to show a better view of results.

	<100>		<110>		<111>	
	Q	AR	Q	AR	Q	AR
Control	0.224	0.306	0.540	0.275	0.471	0.443
Jet	0.228	0.40	0.50	0.340	0.291	0.441
Comparison	1.87%	30.76%	-7.47%	23.41%	-38.15%	-0.49%

Table 6.28: Experiment Summary for Si + SiO₂ + PR + BOE

Overall, the results from etching <100>, <110> and <111> silicon with a hard mask consisting of thermally grown silicon which was opened by BOE, indicate that the jet has the effect of improving the light trapping capability of the trenches we would like to accomplish by improving either their aspect ratio, their quality factor, or both at the same time. In the case of <100> Si, aspect ratios were

significantly improved (by about 30%) and the quality factor remainder high even if it decreased slightly. In the case of $\langle 110 \rangle$ the aspect ratios are also improved (23.4%) while the quality of the trench also improves (7.5 %). Finally, $\langle 111 \rangle$ silicon shows improvement in quality (38.2%) but little change in the aspect ratios. We can therefore state that the jet etching process improves the overall quality of the trenches in all the crystal orientations tested.

Additionally, we can conclude from these experiments that the etching solution used (11:2:4) has an isotropic etching behavior only in $\langle 100 \rangle$ silicon. In the other two orientations $\langle 110 \rangle$ and $\langle 111 \rangle$ the etchant results in cross-sectional shapes that have steep walls and flat bottoms which reduces their quality significantly and the jet etching process has difficulties compensating for the lack of isotropy of 11:2:4 in these crystal orientations. In other words, while the jet etching process improves the quality of the trenches compared to no jet scenario in $\langle 110 \rangle$ and $\langle 111 \rangle$ silicon, it still does not bring it to the level of quality associated with $\langle 100 \rangle$ silicon.

6.4 Discussion of Results

In this section, we have described the experiments conducted using jet etching. We first presented results for stationary jet etching of $\langle 100 \rangle$ Si using a photo-resist mask. Then, we experimented with a hard mask of silicon oxide opened using concentrated HF and etched using a moving jet for samples of $\langle 100 \rangle$, $\langle 110 \rangle$, $\langle 111 \rangle$ and multi-crystalline silicon. Finally, we have conducted a last set of experiments using $\langle 100 \rangle$, $\langle 110 \rangle$ and $\langle 111 \rangle$ Silicon with an oxide mask, opened using 5:1 BOE and etching using a moving jet etch apparatus.

First, we find that the jet etching process confirms the simulation results from chapter 3 which is that a local jet effect takes place in the trenches resulting a selective etching at the bottom of the trenches which results in higher aspect ratios and better light trapping quality in the trench profiles.

We notice that for $\langle 100 \rangle$ Si the aspect ratio is significantly increased. The aspect ratio is improved by 50.4 % in the Shipley coated sample and stationary nozzle case, 10% in the oxide mask opened with 1:1 HF with moving nozzle case and finally the AR is improved by 30.7% in the oxide mask opened with BOE, etched with moving nozzle.

In the case of <110> Si the aspect ratios were increased as well in all cases as well. In the case where the <110> Si sample with an oxide mask and 1:1 HF opening, the aspect ratio was increased by 65.2%. Additionally, in the case where the sample with an oxide mask was opened using 5:1 BOE, the AR was improved by 23.4%.

However, in the case of <111> Silicon we find that the jet does not have a significant effect of the aspect ratio of the trenches. In both cases considered, an oxide mask sample opened with 1:1 HF and an oxide mask sample opened with BOE, the aspect ratios resulting from the jet etching case were actually decreases compared to the control, by 11.9% and 0.49% respectively. This shouldn't interpreted as disqualifying the positive effect of the jet since the etchant used was found not to be isotropic as expected and could therefore have the particular effect of etching <111> Si samples in a way that causes the jet to be ineffective in this particular configuration. Although the jet has little effect on the aspect ratio of features in the <111> orientation, it has however a strong effect on improving their light trapping quality.

Light trapping quality in <111> samples has shown significant improvement from the jet. In the case where the oxide mask <111> sample opened with 1:1 HF, the light trapping quality of the trenches underwent an improvement of about 13.2% while the case of the samples opened with BOE, it improved by 38.15%.

Similarly, in the <110> samples, we notice an improvement in the light trapping quality of the trenches. In the case of the opening the oxide mask with 1:1 HF, the light trapping quality of the trenches was improved by 1.55%, while it was improved with 7.5% in the case where the oxide mask was opened with BOE.

Finally, in the case of the <100> samples, the light trapping quality was improved as well when it wasn't already high. In the case of the <100> samples with only a photo-resist mask (no oxide mask), the light trapping quality was improved by 17.5%. In the case of the oxide mask opened with 1:1 HF, it was improved by 13.4%. Finally, the case of oxide mask opened with BOE, the light trapping quality remained roughly the same as the control case, which was already very high.

When we conducted experiments on multi-crystalline silicon, we found that in the case of a wafer etched for saw damage removal, the resulting trenches were non-uniform and non-symmetrical. Although we found high aspect ratios and desirable light trapping quality on the control samples (with no -jet), there was little uniformity between the trenches. In this case, the jet had the effect of

improving the uniformity of the trenches while not affecting the quality and the aspect ratios of the trenches.

However, the experiments we conducted on the polished multi-crystalline wafers showed results that suggest that the jet does improve both the quality and the aspect ratio of the trenches. Compared to the control experiment, the light trapping quality was improved by 21.5% and the aspect ratio by 9.0%. This result corroborates the previous findings for all crystallographic directions tested.

During our experiments we have tested two mask types and two different methods for opening the silicon oxide mask. We found that using a photo-resist mask yielded poor results overall since the mask lifted off early during the etching process. This was noticed more often in the case of the jet etching compared to the etching process during the control experiment. We solved this problem by using a hard mask, silicon oxide, which was made from growing a layer of thermal oxide and patterning it with the photo-resist. Opening the mask with a 1:1 HF solution proved to be difficult to control, because the photo-resist lifted off early in the etching process causing the remaining mask pattern to be different from the mask pattern. Finally, for the last set of experiments we used a 5:1 BOE solution to etch the oxide mask. This method enabled the photo-resist to remain on the surface of the sample during the etching process resulting in an adequate duplication of the photo-resist pattern onto the oxide mask.

Finally, the results of the experiments above did not show a consistent repeatability. Although multiple samples were etched for each experiment configuration, they did not all indicate the same result. The primary inconsistency we noticed related to etch time. Although, we took great care into determining the appropriate etch time for each experiment by etching samples prior to each experiment in the sole purpose of determining the appropriate etch times, we still found samples that were either under-etched or over-etched. We therefore showed results for the samples that were properly etched. The etch time variations could be due to the fact that we recycled the etching solution for multiple experiments which could have caused some reaction products to alter the etching properties of the etchant. In sum, we showed results for the best sample we obtained in each experiment, leaving etchant controllability and result repeatability for future work.

6.5 Conclusion and Future Work.

In conclusion, the jet etching process has shown results indicating that it is capable of increasing the light trapping quality of the trenches as well as their aspect ratio. In all crystallographic directions tested, we have seen that jet has a positive effect, either in increasing the aspect ratio, the light trapping ability or both at the same time. We also found that on multi-crystalline silicon, the jet had the effect of improving the uniformity of the etched trenches, especially when the wafer was initially processed for saw damage removal.

The masks used in these experiments lead to the conclusion that a hard mask is necessary in order to obtain the desired features. A photo-resist mask was not compatible with the process since it lifted off too early during etching. It must be noted that our method for obtaining a hard mask is most likely not scalable and further research needs to be conducted into low cost hard mask methods. An oxide mask takes 20 hours to grow at 1100°C and needs to be patterned with expensive photolithography steps. This makes the masking processes used in these experiments not suitable for large scale manufacturing.

In addition to more research in the masking step, future work should include using an acid composition that is more suited for isotropic etching. We suggest that in the research for this composition that crystal orientation of <100>, <110> and <111> should be used such that we ensure that the composition is indeed capable of isotropic etching. Finally, the new acid composition should be tested on multi-crystalline silicon to make sure that it is isotropic.

Future work should also be conducted for higher impinging jet velocities. Although our simulation work indicated that jet velocities of 5 m/s and 10m/s should give better jet effect than 3 m/s, we used the latter for safety purposes mainly since HF and Nitric acids are hazardous chemicals. Higher jet velocities can be tested with more sophisticated, contained equipment.

Finally, the effect of the jet were observed in this case on sample that were no larger than 1 cm². Therefore, testing jet etching on 156 x 156 mm wafers would yield results more appropriate to real size processing.

Chapter 7 Cost Analysis.

7.1 Introduction

To measure the economic impact of the technical work described in the previous section, it is necessary to conduct a cost analysis of the cell making process which includes a new jet etching step. The main goal of this cost analysis is to determine the necessary efficiency improvements that the jet etching process would have to deliver in order to be economically feasible. To do so, we construct a cost model of a standard solar cell manufacturing process, supplemented with recent developments in the cell making process and compare it to the jet etching cost model. In this section, we describe the basic processes involved in the cell making process, then we discuss how the cost of each step was modeled. Finally we discuss the necessary efficiency that must be yielded by a process that includes jet etching and its implication on the target aspect ratio and Q-factor that would be necessary for the economic feasibility.

7.2 Cell Making Process Description

Crystalline solar cells are manufactured using for the most part well established semi-conductor processing steps. In this analysis we limit our study to the cell making steps only. Costs involved in wafer manufacturing and module assembly are not included.

The diagram shown in Figure 7.1 describes the cell processing steps described in this work. All three scenarios are shown in this figure with the additional step standing out in lighter color.

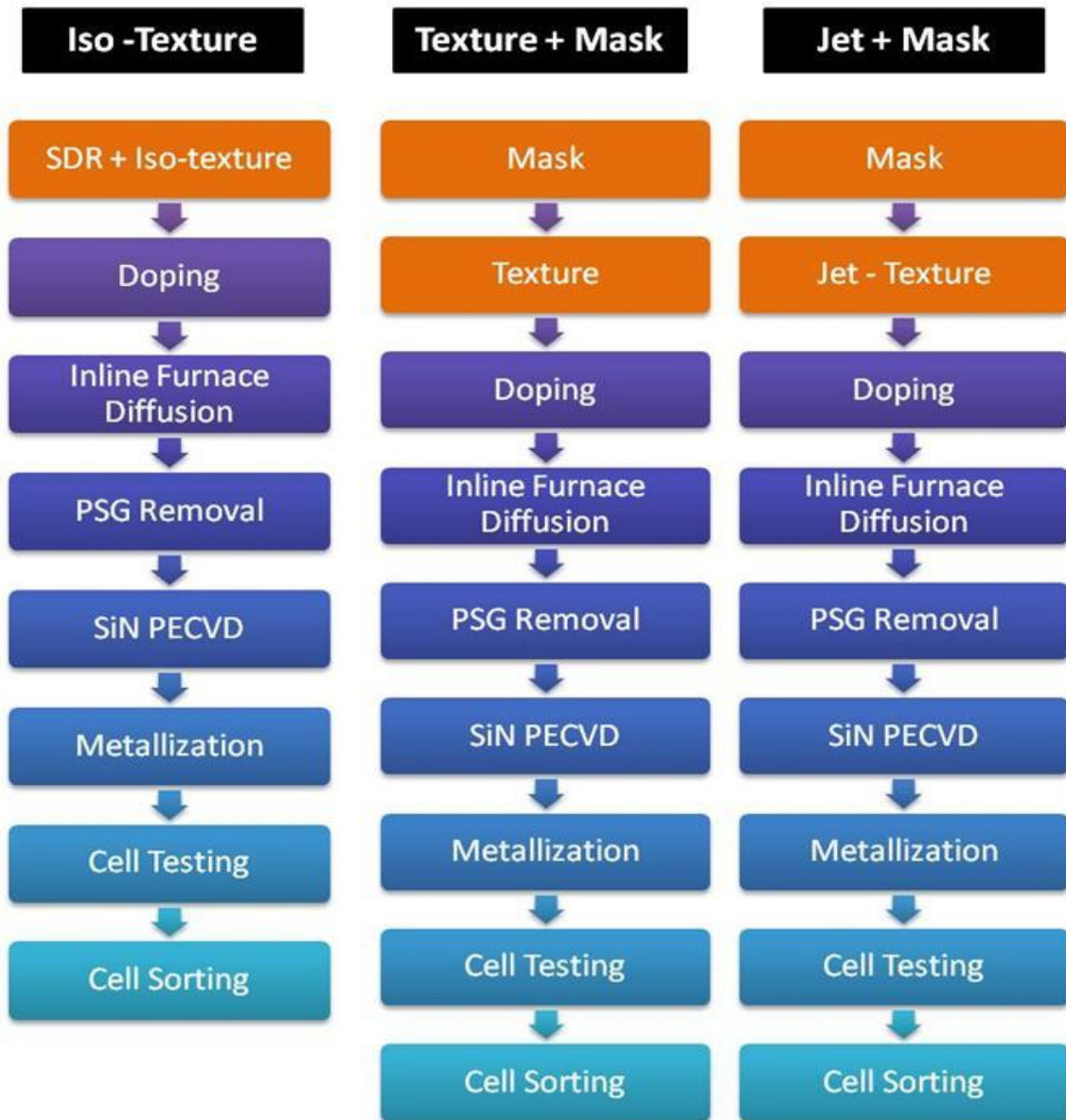


Figure 7.1: Cell processing steps diagram⁴

7.2.1. SDR removal + Iso- Texture:

The Saw Damage Removal (SDR) step is the first in the process and serves the purpose of reducing damage inflicted to the wafer from the wafer sawing steps. Wafers resulting from the ingot

⁴ The iso-texture processing step is actually combined with the SDR step. We separate it in this diagram from clarity purposes.

wire-sawing process typically have micro-cracks on their surface which must be removed for proper processing of the wafer into a solar cell. This step is typically conducted by immersing the wafers in a bath of acid with a composition specifically designated to remove about 3-5 μm of material on both sides of the wafer in order to remove the micro-crack. In recent manufacturing development, the SDR step has become combined with a surface texture step called iso-texture. As the wafers are being etched for saw damage removal they are at the same time patterned for surface texturing which increases their light trapping ability. The equipment used in this step is a wet etching bench that is typically capable to process 1200 to 2400 (29) wafers per hour. At the end of the process the wafers are cleaned with DI water and dried for further processing.

The saw damage removal combined with iso-texturing step cost is estimated using the information summarized in Table 7.1 below. The principal cost elements modeled in this step are the cost of equipment, consumables and labor. We assume that this step would require 0.5 operators per shift average for a 24 hours, 7 days a week operation, according to information from industry insiders. Each work shift is 8 hours long and the modeled plant would operate 335 days per year amounting to 8040 hours. Engineers and managers work hours are estimated as a fraction of the operators work hours and are respectively 25% and 5% according to estimates from the Centrotherm case study(30), while worker yearly salary are taken as the yearly average salary for industrial managers, engineers and technicians from the Bureau of Labor Statistics (31). The depreciation period for the equipment is assumed to be 5 years with a 7% discount rate. The cost of water is calculated from the information on water consumption from the manufacturer and multiplied by the assumed cost of DI water, which we assume to be 0.5 $\text{¢}/\text{L}$. Electricity costs are estimated based on manufacturer's information on average electricity consumption multiplied by a 7 $\text{¢}/\text{kWh}$ assumed electricity cost. Finally, the cost of acids is obtained by assuming that the SDR + Iso-texture step remove about 5 μm of silicon from each side of the wafer, which can yield the amount of HF and HNO_3 acids required to remove this quantity of silicon.

Costs		\$/cell	\$/Wp
Equipment	SDR + Iso-Text	0.021014	0.005911
Consumables			
	Water	0.009098	0.002559
	Electricity	0.00273	0.000768

	Acids	0.0113	0.003179
Labor			
	Operators	0.008968	0.002523
	Engineers	0.002242	0.000631
	Management	0.000448	0.000126
TOTAL		0.0558	0.0156

Table 7.1: SDR + Iso-texture step cost

The cost of production of each cell is an amount that is independent of cell efficiency and reflects the cost of production of each solar cell on a \$ / cell basis. In contrast, the cost per peak power output of the cell depends on the efficiency of the device. The \$/Wp amount is inversely proportional to the efficiency of the cell and follows the equation below:

$$C_{Wp} = \frac{C_{cell}}{A * G * \eta}$$

Where: C_{Wp} , is the cell cost in \$/Wp; C_{cell} is the cell cost in \$/cell; A is the surface area of the cell; G is the peak solar radiation at the surface of the earth = 1000 W/m²; and η is the cell efficiency.

Therefore while the cost of a cell might be increasing due to additional manufacturing steps, the cost of the watt output could decrease if the additional steps increase the efficiency of the device. In the case shown in Table 7.1 the cost of the SDR+ Iso texture step is 5.58 ¢ / cell, mainly due to the cost of consumables used in this step.

7.2.2 Doping Step and In-line Furnace:

The doping step consists of diffusing phosphorus into the wafer in order to create a PN junction in the wafer. This step can be conducted in two different ways. The first involves the use of high temperature (about 1000 C) tube furnaces where wafers are inserted in batches, then doped by diffusion of Phosphorus OxyChloride (POCl₃) gas into the chamber. The second method consists of depositing a fluid layer of phosphorus dopant (typically phosphorus acid) onto the surface of the wafer which is then introduced into an in-line furnace where the diffusion takes place again at about 1000 C.

The main difference between the two methods is that one offers a batch processing solution while the other is an in-line processing method.

The doping step is modeled following similar assumptions as the SDR+ Iso texturing step. Equipment cost information was obtained from Photon International Magazine(32), however dopant mixture costs were obtained from Photovoltaic International(33). The assumed throughput in this case is the same as above and is estimated from the Centrotherm (30) case study. We see that the cost of the dopant deposition step is about 3.26 ¢/ cell. This step is relatively inexpensive due to low cost of consumables for doping and the low equipment cost.

Costs		\$/cell	\$/Wp
Equipment	Spray on Doper	0.010256	0.002885
Consumables			
	Water	0	0
	Electricity	0.000284	7.97E-05
	Dopant Mixture	0.0104	0.002916
Labor			
	Operators	0.008968	0.002523
	Engineers	0.002242	0.000631
	Management	0.000448	0.000126
TOTAL		0.0325	0.0091

Table 7.2 Doping Step Cost Analysis

In the case of the In-line furnace step, since this step consists essentially in heating up the wafers for an extended period of time, energy costs is a significant portion of the total cost per cell in this case about 23%. The largest portion of the cost of this step is however the cost of equipment at about 52%. The cost per cell for the modeled line which employs two in-line furnaces is about 4.82 ¢/ cell.

Costs		\$/cell	\$/Wp
Equipment	Inline furnace	0.025481	0.007168

Consumables			
	Water	0	0
	Electricity	0.011159	0.003139
Labor			
	Operators	0.008968	0.002523
	Engineers	0.002242	0.000631
	Management	0.000448	0.000126
TOTAL		0.0482	0.0135

Table 7.3: In-Line Furnace Step

7.2.3 PSG removal:

After the diffusion step, a thin layer of Phospho-Silicate Glass grows on the surface of the wafer due to the presence of O₂ in the diffusion environment. This layer is undesirable for the cell making process and must be removed. In this same step, an etching process is performed in order to isolate the pn-junction formed during the diffusion process. The equipment used for removing the PSG layer and performing the junction isolation is a wet etching station, similar in nature to the one employed in the SDR step. Typical throughputs of such equipment is 1200 to 2400 wafers as well. At the end of this step the wafers are cleaned with DI water, dried and transferred to the next step.

The PSG step consists of a wet etching station tailored to removing the PSG layer and performs the step of edge isolation. The cost of acids is the largest consumable cost. The cost per cell of this step is 5.7 ¢/ cell.

Costs		\$/cell	\$/Wp
Equipment	PSG-Junction removal	0.020930918	0.005887741
Consumables			
	Water	0.002380952	0.000669748
	Electricity	0.000924	0.000259916
	Acids	0.0032	0.000888628

Labor			
	Operators	0.017935522	0.005045154
	Engineers	0.004483881	0.001261288
	Management	0.000896776	0.000252258
TOTAL		0.0507	0.0142

Table 7.4: PSG removal step

7.2.4 Silicon Nitride PECVD:

Once the wafers are doped and rid of their PSG layer, they are then submitted to a deposition of a thin layer of Silicon Nitride (Si_3N_4) about 80nm in thickness. The purpose of this layer is to cover the surface of the cell with an anti-reflective coating which significantly increases the light absorptivity of the cell. A SiN layer results in a deep blue color with high absorptivity. This process is done using a Plasma Enhanced Chemical Vapor Deposition chamber. PECVD processes typically involve expensive equipment that require high vacuum for their operation. Silane and Ammonia gases are used as the principal chemical species in this procedure, which can be a slow process that is often a bottle neck in solar cell fabrication.

A large portion of the total cost is due to equipment cost at about 28.2%, which can be explained by the complexity of the PECVD equipment and the fact that multiple stations in parallel are necessary. However, the largest portion of the cost of the cell is due to the gasses used for this process. Silane and Ammonia gasses combined represent 41.8% of the cost per cell for this step. A reduction in the cost of procurement of these gases would have a significant impact on the cell making process.

Costs		\$/cell	\$/Wp
Equipment	PECVD	0.032761	0.009216
Consumables			
	Water	0.009524	0.002679
	Electricity	0.00231	0.00065
	Gas- Silane	0.0213	0.005978
	Gas- Ammonia	0.0275	0.007735
Labor			
	Operators	0.017936	0.005045

	Engineers	0.004484	0.001261
	Management	0.000897	0.000252
TOTAL		0.1166	0.0328

Table 7.5: SiN PECVD Step Cost

7.2.5 Metallization:

Once the wafers have been coated with a Silicon Nitride anti-reflective layer, they are then processed for metallization. This step serves the purpose of depositing electrically conductive fingers on the surface of the cell that act as an electron capturing device. The fingers are made of a highly conductive silver paste that is deposited on the surface of the wafer using a screen printing process, where the paste is pressed through a silk screen using a squeegee and results in the desired deposition pattern. The wafer, along with the freshly deposited silver paste are inserted in a firing furnace where the paste dries and bonds to the surface of the wafer at about 450 C.

According to our model, the metallization step is the most expensive one in the entire cell making process. This is primarily due to elevated costs of consumables employed in this step. The combined costs of all contacts in this step represent 82% of total step cost. The pastes used for this process are silver based, which explains their elevated cost. Again, a significant cost opportunity reduction lies in researching alternate metallization methods that would either reduce the amount of consumables needed or significantly reduce their cost.

Costs		\$/cell	\$/Wp
Equipment	Metallization	0.050962235	0.014335368
			0
Consumables			0
	Water	0	0
	Electricity	0.0002835	7.97468E-05
	Paste front Cost	0.1580	0.04444557
	Paste back Area	0.1479	0.0416
	Paste back contact	0.1577	0.044360056
Labor			
	Operators	0.035871045	0.010090308
	Engineers	0.008967761	0.002522577

	Management	0.001793552	0.000504515
TOTAL		0.56147	0.1579

Table 7.6: Metallization Step Cost

We model the firing step as an in-line furnace with a throughput high enough such that only one furnace is used. The furnace involved in this step uses temperature significantly lower than the diffusion step (about 450 C) and electricity is the main consumable for this step. This step is relatively inexpensive compared to the rest of the process.

Costs		\$/cell	\$/Wp
Equipment	Firing furnace	0.012741	0.003584
Consumables			
	Water	0	0
	Electricity /year	0.010043	0.002825
Labor			
	Operators	0.008968	0.002523
	Engineers	0.002242	0.000631
	Management	0.000448	0.000126
TOTAL		0.034442	0.009688

Table 7.7: Firing Furnace Step Cost

7.2.6 Cell Testing and Sorting:

After the firing step, the wafers are now functioning solar cells. They must be tested for their I-V curve characteristics in order to separate the cells into matching current and voltage characteristics which is critical for the module making process. Finally the cells are sorted in batches ready for module processing.

The cell testing and sorting steps are relatively inexpensive steps. The majority of the cost is embedded in the equipment and operation costs, as can be seen in Table 7.8 below.

Costs		\$/cell	\$/Wp
Equipment	Cell Tester+ Sorter	0.013472	0.00379
Consumables			
	Water		
	Electricity	0.000421	0.000118
Labor			
	Operators	0.017936	0.005045
	Engineers	0.004484	0.001261
	Management	0.000897	0.000252
TOTAL		0.037209	0.010467

Table 7.8: Cell Testing and Sorting Step Cost

7.2.7 Additional Steps

In the model we compare two scenarios to the jet etching scenario. First, we compare a cell making process that includes a combined iso-texturing process and an SDR process to the process that includes jet etching. Then we compare the jet etching process with a texturing step that is preceded with a masking step for specific, non-random, light trapping features.

7.2.7.1 Texture with mask.

The latest developments in surface texturing of the solar cells have led to the establishment of a new process of isotropic etching of light trapping features. This new process involves a masking step which delivers a predetermined etching pattern resulting in controlled light trapping features which have better light trapping ability than the random iso-texture. The added cost of the masking step would be compensated by the increase in efficiency resulting from better light trapping features.

For this step, we assume that the process is similar the iso-texturing step but with an additional masking step. This masking step involves depositing on the wafer a thin layer of masking compound, similar to photo-lithography processing. Knowing that the number of steps and the cost of consumables for photo-lithography are too expensive to be incorporated in this process, we assume that this masking step is a novel type of masking process with a cost comparable to the doping step (lowest step cost in the process and similar processing technique). It is fair to assume that the equipment for a novel

masking layer would be similar to a spray doping equipment since the process of coating a wafer with a mask would involve a process similar to spraying, so we estimate its cost to vary within +/- 20% of the doping step cost.

7.2.7.2 Jet etching with mask:

This step represents our attempt to integrate the present research work into the cell making process. If the jet etching process were to be implemented in a cell making line, it would have to include a masking step and added cost for a jet etching station. This latter one would essentially be a wet etching station fitted with additional parts in order to achieve the jet of etchant necessary for higher aspect ratio and higher Q-factor trapping features.

The jet etching step is modeled from the iso-texturing step. Given that a would-be jet etching station should be similar in nature to a texturing station, we estimate a jet etching station cost from the texturing station cost and account for additional equipment necessary such as nozzles, revolving mechanisms and pumps pressurizing the jet. For simplicity and given the early stage of the jet etching device constructed, we estimate a would-be jet etching station cost as a texturing station multiplied by a factor varying between 0 to 30% of additional cost.

7.3 Cost of Cell Making Process:

The analysis assumes a wafer geometry of 156 mm x 156 mm and a thickness of 180 μm . For a device with random iso-texture, we assume that the efficiency is 15.8% (30). Additionally, we assume that an additional masking step combined with a specific light trapping feature would raise the cell efficiency by about 0.5% absolute to 16.3%⁵.

This section is a summary of all costs involved in the cell making process for three scenarios considered: a cell with iso-texture, a cell with texture through mask and finally the jet texture which includes a masking step. Figure 7.2 below, shows the cost of cell making of the first three processes compared with the jet etching process. As the efficiency of a jet etched cell increases, its cost decreases, which is indicated by the negative slope of the jet texture curve. Most importantly, this graph shows the

required minimum cell efficiency of a jet etching process to be cost competitive with the other two processes.

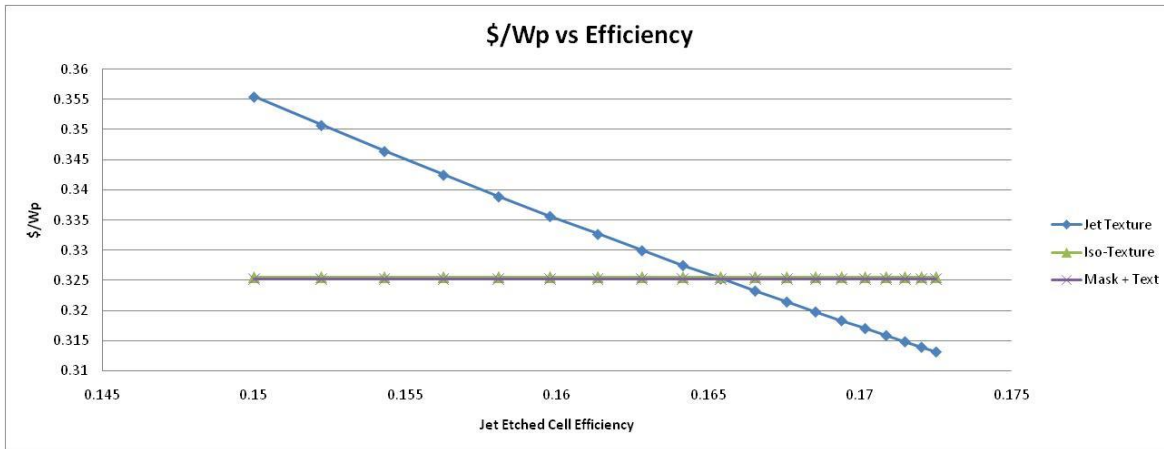


Figure 7.2: Comparison of two cell making processes with the jet etching process (assuming the jet etcher additional cost is 20% more than iso-texturing equipment and the masking step is the same cost as the doping step)

7.3.1 Iso-Texture

The iso-texture process consists of etching random features on the surface of a cell in order to increase its light trapping ability. This adds an additional step to the process thus raising the total cost per cell. However, this process also increases the efficiency of the resulting cell to about 15.8%. As can be seen in

Step Description	Cost / cell	Cost/Wp
SDR removal + Texture	0.0558	0.0157
Doping	0.0326	0.0092
Inline Diff Furnace	0.0483	0.0136
PSG removal	0.0507	0.0143
SiN PECVD	0.1167	0.0328
Metallization	0.5615	0.1579
Firing Furnace	0.0344	0.0097
Cell Sorting	0.0372	0.0105
Building	0.1116	0.0314
Auxiliary + Miscal 10%	0.1049	0.0295
Total	1.1537	0.3245

Table 7.9, the cost of a watt produced with this process is about 32.45 ¢/Wp. We should note that the 15.8% efficiency value used in this model is stated to be a minimum value for this process, which could therefore yield higher cost savings if the process yielded higher efficiencies. Additionally, the industry has adopted this step in their fabrication lines, which is a testament to its cost saving potential.

Step Description	Cost / cell	Cost/Wp
SDR removal + Texture	0.0558	0.0157
Doping	0.0326	0.0092
Inline Diff Furnace	0.0483	0.0136
PSG removal	0.0507	0.0143
SiN PECVD	0.1167	0.0328
Metallization	0.5615	0.1579
Firing Furnace	0.0344	0.0097
Cell Sorting	0.0372	0.0105
Building	0.1116	0.0314
Auxiliary + Miscal 10%	0.1049	0.0295
Total	1.1537	0.3245

Table 7.9: Cell making cost for a process with Iso- Texture

Comparing this step with the jet etching process in Figure 7.2, indicates that jet etched cells would have to reach efficiencies around 16.6% for cost competitiveness. Again this efficiency range is realistic given the fact that the jet etching step yields higher efficiencies than the texture with mask step which can add an additional 0.8% efficiency to the iso-texture step.

7.3.2 Texture + Mask

This processing step is still in research and development phase, some experimental cells have been produced using a masking step and isotropic etching acids (34) and show high potential for efficiency improvement. We therefore model this step as being similar to the iso-texture step in equipment cost with an additional cost for the masking step. This latter one is estimated from the doping step cost with a sensitivity range of + or – 20%, as explained in section 7.2.7.1. Table 7.10 below summarizes the cell cost and power output cost for a cell incurring this process, with the assumption

that the added cost of the making step is equal to the cost of the doping step and the cell efficiency to be 16.3 %, which is 0.5% more than the iso-texture step.

Step Description	Cost \$/ cell	Cost \$/Wp
Masking Step	0.0326	0.0089
Texture	0.0558	0.0152
Doping	0.0326	0.0089
Inline Diff Furnace	0.0483	0.0132
PSG removal	0.0507	0.0138
SiN PECVD	0.1167	0.0318
Metallization	0.5615	0.1531
Firing Furnace	0.0344	0.0094
Cell Sorting	0.0372	0.0101
0.0000	0.0000	0.0000
Building	0.1116	0.0304
Aux+Misc	0.1081	0.0295
Total	1.1895	0.3243

Table 7.10: Cell making cost for a process with texture + mask

For this step to be economically viable it has to be able to deliver 0.5% additional efficiency at the large scale manufacturing level and utilize masking processes that are similar to the cost of the spray-on doping step. We conduct a sensitivity analysis for the cost of the masking step and discuss it below. For the assumptions used in this case, which are the same as the assumptions used to generate the graph in Figure 7.2, the minimum required efficiency for jet etched cells would have to be 16.6%.

7.3.3 Jet Etching + Mask

The jet etching step is modeled using the same information as the texture with mask step and adding an additional cost factor for the jetting capabilities of a wet etching machine. As discussed in section 8.2.2.3, the jet etching equipment cost is estimated from the texturing equipment with an additional 0 to 30% added cost to account for jetting capabilities.

Step Description	Cost \$/ cell	Cost \$/Wp
Masking Step	0.0326	0.0085
Jet Texture	0.0670	0.0175
Doping	0.0326	0.0085

Inline Diff Furnace	0.0483	0.0126
PSG removal	0.0507	0.0133
SiN PECVD	0.1167	0.0305
Metallization	0.5615	0.1468
Firing Furnace	0.0344	0.0090
Cell Sorting	0.0372	0.0097
Building	0.1116	0.0292
Aux+ Misc	0.1093	0.0307
Total	1.0925	0.3164

Table 7.11, shows the costs for this step assuming an additional 20% cost factor for the jet etching equipment and a cell efficiency of 17%. This yields a cost of power output of 31.6 of ¢/Wp, which indicates that if a jet etching process were to yield 17% efficiency cells with a 20% added cost of equipment, the resulting cells would be economically more desirable than all the above scenarios and would represent a cost improvement of about 2.4%.

Step Description	Cost \$/ cell	Cost \$/Wp
Masking Step	0.0326	0.0085
Jet Texture	0.0670	0.0175
Doping	0.0326	0.0085
Inline Diff Furnace	0.0483	0.0126
PSG removal	0.0507	0.0133
SiN PECVD	0.1167	0.0305
Metallization	0.5615	0.1468
Firing Furnace	0.0344	0.0090
Cell Sorting	0.0372	0.0097
Building	0.1116	0.0292
Aux+ Misc	0.1093	0.0307
Total	1.0925	0.3164

Table 7.11: Cell making cost for a Jet etching process which includes a mask.

Not knowing the exact cost for equipment of a jet etcher and having little information on novel, low cost masking steps, we conduct sensitivity analyses to determine in what range these values should be located.

It is important to note that the range of cell costs resulting from our model is within the range of costs found in the literature. In the Centrotherm case study (30), the estimated cell cost is about 0.35 \$/Wp, calculated for a model that attempts to achieve the lowest cost possible in December 2008.

7.4 Sensitivity Analysis

In this section, we perform various sensitivity analyses in order to test the robustness of our assumptions as well as determine the proper range of values where some assumed variable should be located

7.4.1 Sensitivity Analysis for Jet Texture with Iso-Texture.

We conduct a sensitivity analysis for cell efficiencies in the jet etching process versus the iso-texturing process. Figure 7.3 summarizes this analysis. On the vertical axis, we plot the cost difference between the jet etching process and the iso-texture process (Jet – Iso). The cost parity line is indicated on the figure as well. As the iso-texture cell efficiency increases, the corresponding jet etched cell efficiency also increases. For values beyond 16.2% efficiency for iso-textured cells, the jet etched cells would have to exceed 16.8% efficiency to be cost competitive, which is to be difficult to achieve. However, for the assumed 15.8 % iso-texture efficiency, cost parity can be achieved by jet etched cell efficiency of about 16.5 %. If however, this latter is around 17%, it could bring cost savings in the order of 0.01 \$/Wp.

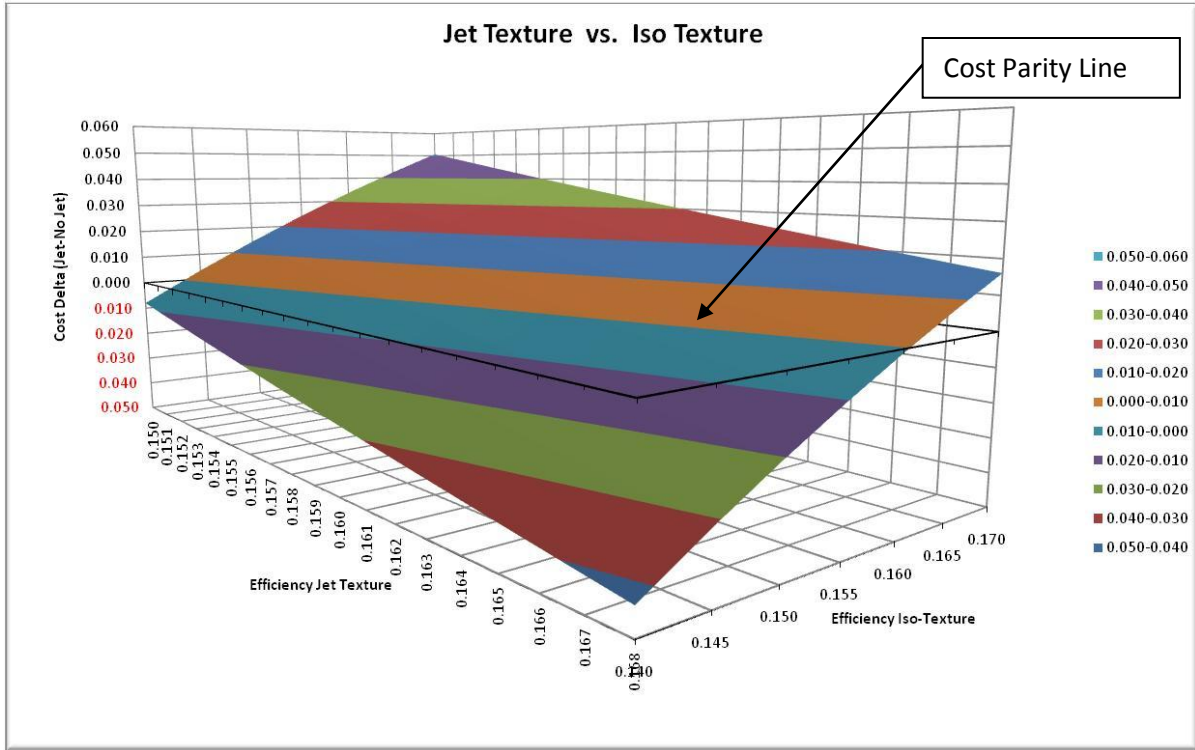


Figure 7.3: Sensitivity analysis for Jet texture compared to Iso-Texture

7.4.2 Sensitivity Analysis of Jet Texture with Texture + Mask

We perform an additional sensitivity analysis for jet etched cell efficiency versus cells textured with mask. The results are summarized in Figure 7.4 below. This analysis assumes that the cost of the mask step is the same for both processes and is equal to the doping step cost. Again, as similar remarks as above can be made.

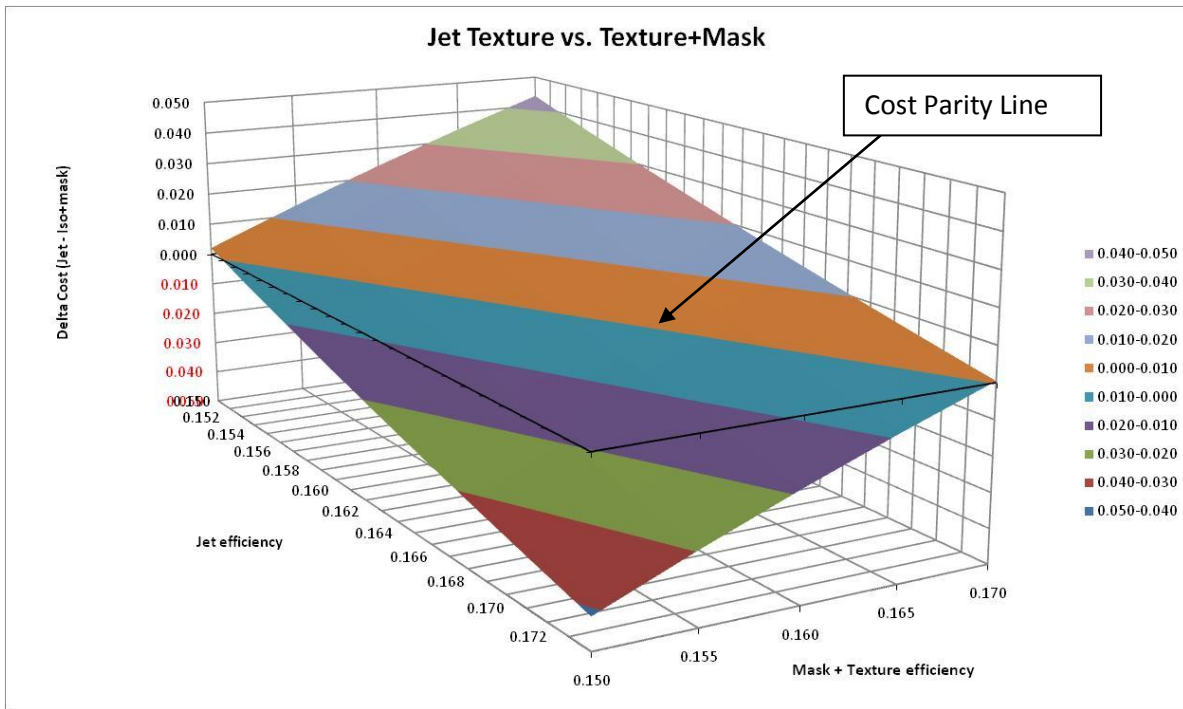


Figure 7.4: Sensitivity Analysis for Jet Texture compared to Texture + Mask

In this case, if the texture with mask process were to yield efficiencies higher than 16.3%, then the jet etching process would have to deliver efficiencies higher than 16.6% for cost competitiveness.

7.4.3 Sensitivity Analysis for Jet etching Cost and Texture + Mask cost.

Since we assumed the jet etcher cost to be an added percentage cost of the texturing process and the masking step cost to be in the range of the doping step cost, we perform a sensitivity analysis to determine the minimum efficiency that a jet etching process must yield. We vary the additional cost of the jet etching equipment from 0 to 30%, while we vary the masking from 20% cheaper than the doping step to 20% more expensive. The analysis result is summarized in Figure 7.5 below.

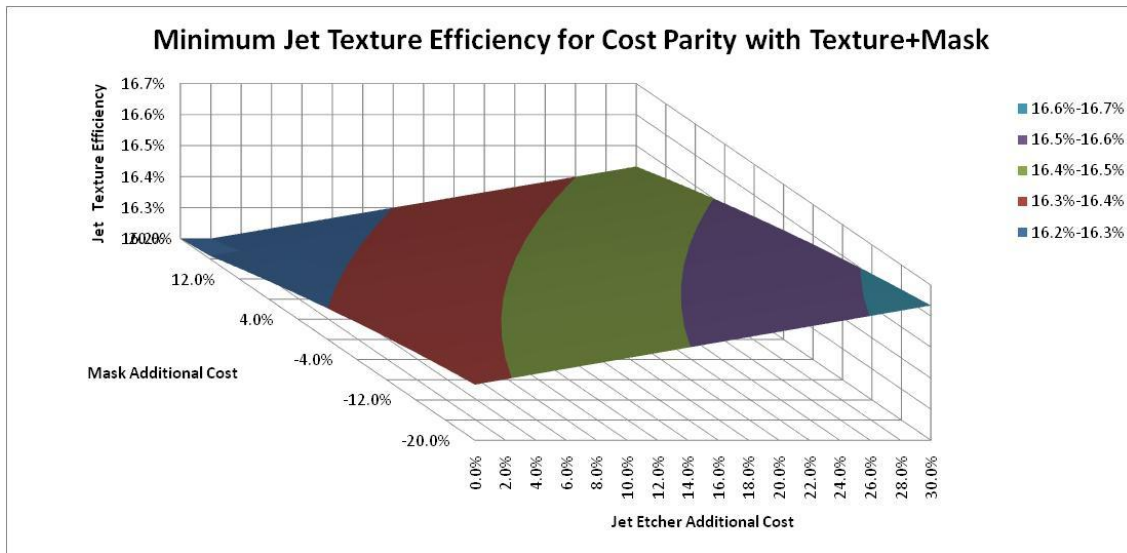


Figure 7.5: Sensitivity analysis for jet etcher cost and masking cost

The first significant result is that for the scenario of 30% additional cost for jet etching step and 20% additional cost for the masking step, we find that the required efficiency of the jet etching process for cost competitiveness is about 16.45%. This represents a 0.15% improvement from the assumed cell efficiency resulting from a cell textured with a mask. In other words, 0.15% efficiency improvement from the texture with mask process is required for jet etching to be cost competitive when the cost of the mask is highest. However, in the case when the mask is 20% cheaper than the spraying on doping step and the jet is 30% more expensive than iso-texture, then the minimum efficiency that the jet would have to deliver is 16.63%, which is about 0.33% higher than the assumed efficiency for the texture with mask case.

In the case where the masking step cost is as low as the doping step cost (i.e. 0% added cost), the minimum required jet etched cell efficiency is about 16.55% for a jet etching added cost of 30%. This shows that the required efficiency from the jet etching process is not very sensitive to the masking step cost when it is in the order of the doping step cost.

7.5 Implications of efficiency for aspect ratio.

Our cost model has enabled us to compare the jet etching process to other cell making processes both established and under development. We now set out to determine the relationship between cell efficiency and aspect ratio of the light trapping features.

As discussed in chapter 2, a ray tracing analysis yielded the relationship between detector hits and aspect ratio shown in Figure 2.2 and Figure 7.6 below. Assuming that the features are parabolas with constant width but increasing aspect ratio, we derive the corresponding relationship between aspect ratios and Q-factor which is shown in Figure 7.7. Noting that for a parabola of given aspect ratio, the value of the Q-factor can be calculated, we therefore only need to use either A.R. or Q-factor for analysis. We choose to use the A.R. for further discussion.

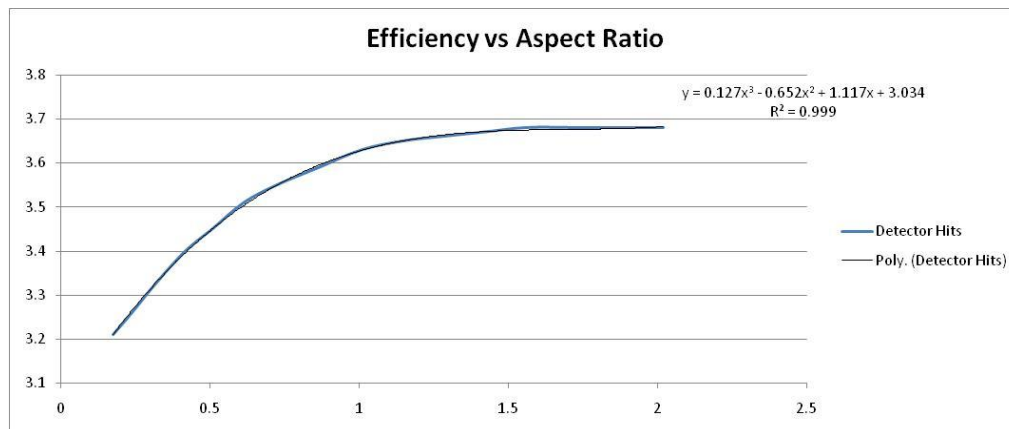


Figure 7.6: Relationship between aspect ratios and detector hits

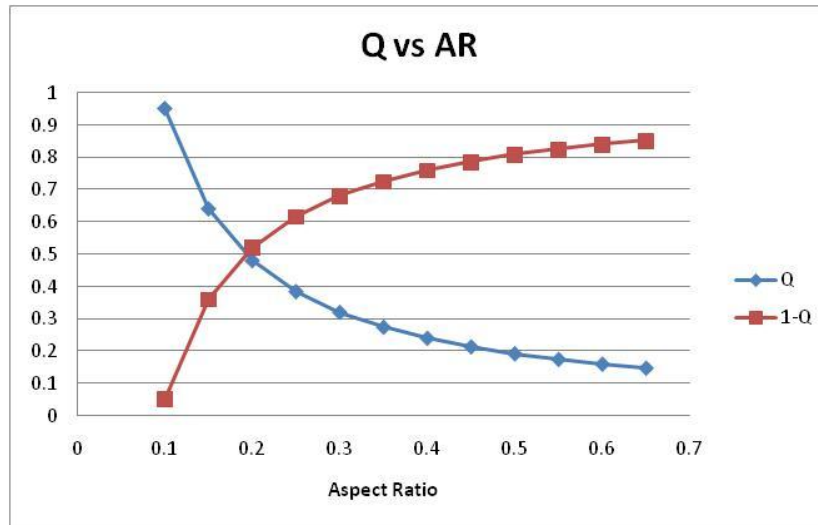


Figure 7.7: Relationship between Q-factor and aspect ratio.

Next we determine the relationship between the A.R. and the resulting efficiency of the cell. We assume that for A.R. = 1 the cell efficiency would be in the vicinity of 17.25% and for A.R. = 0.1 the associated efficiency would be 15%. We then scale the A.R. range according to the equation given from the curve-fit in Figure 7.6 to obtain a relationship between A.R. and efficiency as shown in Figure 7.8.

To verify that this relationship is robust, we compare known cell efficiencies and their corresponding A.R. to the relationship below. First, a cell with no texture typically has an efficiency of about 14.5%. Since no texture is applied to this cell, the aspect ratio of its features is 0. Verifying against the relationship in Figure 7.8, we find that if we extended the curve to an A.R. = 0 it would result in an efficiency of about 14.5% confirming the stated 14.5% efficiency for no texture cells. Second, according to the source of our model, a cell with iso-texture has a cell efficiency of about 15.8%. This corresponds to an A.R. of about 0.3. Given that our experimental data described in chapter 6 has sometimes yielded aspect ratios in this range for crystal orientation such as <110> without jet etching, it seems plausible that a well executed iso-texture etch without a mask could have aspect ratios of about 0.3. Finally, we have assumed a cell efficiency of 16.3% for a texturing process that uses a mask but no jet, which is in effect similar to the control experiments discussed in chapter 6. According to Figure 7.8 below, an efficiency of 16.3% translates to an A.R. = 0.4. We have often encountered such aspect ratios for our control experiments (etching with no jet), which confirms that the efficiency and aspect ratio relationship in Figure 7.8 is reliable for the purposes of this work.

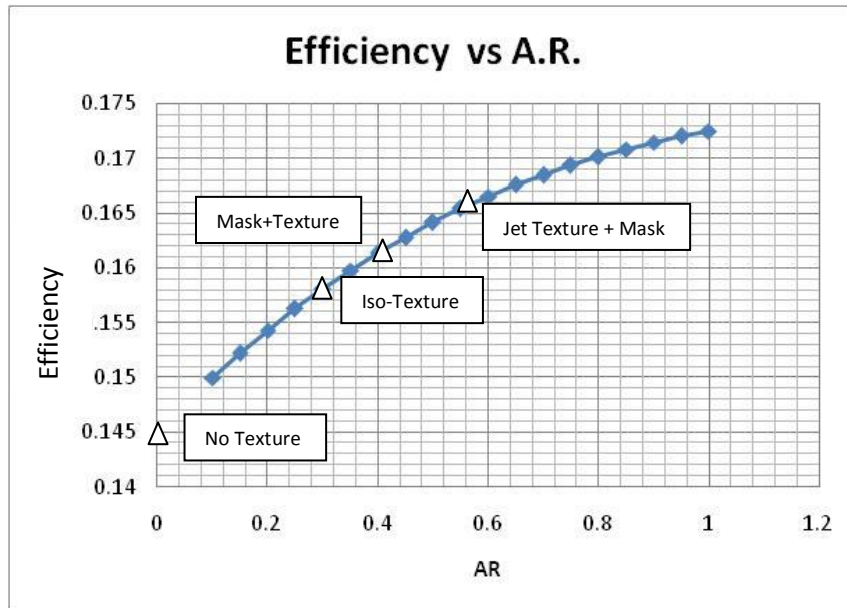


Figure 7.8: Relationship between aspect ratio and cell efficiency

According to our cost model analysis the highest efficiency that the jet etching process must achieve for cost parity with the worst case scenario was 16.63%. This corresponds to an aspect ratio of about 0.57. Such an aspect ratio is theoretically impossible to achieve with simple isotropic etching process, however we showed in our experiments that jet etching is capable of etching features with aspect ratios reaching 0.62 and has exceeded aspect ratios of 0.5 for multiple experiments. This indicates that the jet etching process developed in this work is capable of achieving the aspect ratios necessary for the modeled jet etching process cost to be competitive.

7.6 Discussion and Conclusion

The cost analysis performed in this work has enabled us to find interesting results relevant to cell making economics and to the target value of cell efficiency that the jet etching process must be able to achieve.

In detailing the cost of each step, we find that the cost of consumables in cell making is a large portion of the total cell cost. According to our model, the cost of consumables represents about 50% of total cell cost. This value is higher than the values found in the literature, which suggest that the cost of

consumable is about 40% (35). Our higher estimate is most-likely due to the difficulty to obtain reliable costs of procurement of consumables and the scale at which they are consumed. Nonetheless, consumable represent a significant cost reduction opportunity, especially in the SiN PECVD deposition process and the screen printing process. Research should be undertaken for low cost anti-reflective coatings with high throughput methods and also for metallization steps that do not require expensive consumables.

Our sensitivity analysis shows that for an added cost of 30% for jet etching equipment and -20% for masking equipment (compared to the texturing equipment and the doping equipment respectively), the jet etching process would have to yield a minimum efficiency of about 16.63%. This corresponds to aspect ratios around 0.57. This raises an important remark on target setting.

This work was initially started with a target aspect ratio of 1.0 according to ray tracing simulation results. This target, which was set from a technical analysis perspective proved difficult to achieve using the jet etching method. Noting that the jet etching process yielded aspect ratios around 0.6, the target aspect ratio was modified to 0.75. As it still proved difficult to achieve this target, the jet etching process was found to be able to improve the quality of the features but not able to reach the target set from the technical analysis. However, it would be interesting to find out if the partial achievements that jet etching delivers would be enough to justify its implementation in the cell making process.

Our cost analysis enabled us to answer this question. We find that jet etching process would have to have a 16.63% efficiency for cost competitiveness, which corresponds to aspect ratios of 0.57. This value of aspect ratio is within the reach of the jet etching process as experimental results show. Therefore according to this analysis, the jet etching process would have a viable integration in the cell making process.

Bibliography

1. *Solar and Wind Energy Resources and Prediction*. **Quanhua Liu, Qinxian Miao, Jue J. Liu and Wenli Yang**. 043105, s.l. : American Institute of Physics, July 15, 2009, Journal of Renewable and Sustainable Energy, Vol. 1.
2. **Tester, Jefferson W, et al.** *Sustainable Energy: Choosing Among Options*. s.l. : MIT Press, 2005.
3. Revision 2004. *www.un.org*. [Online] Population Division of the Department of Economic. [Cited: 02 11, 2010.] <http://www.un.org/esa/population/publications/WPP2004/2004EnglishES.pdf>.
4. World Energy Demand and Economic Outlook. *www.eia.gov*. [Online] May 27, 2009. [Cited: 05 03, 2010.] <http://www.eia.doe.gov/oiaf/ieo/world.html>.
5. International Energy Outlook 2009. *www.eia.gov*. [Online] Energy Information Administration. [Cited: 02 11, 2010.] http://www.eia.doe.gov/oiaf/ieo/pdf/ieoreftab_1.pdf.
6. Annual Insolation. *www.nrel.gov*. [Online] Electric and Hydrogen Technologies and Systems Center, May 2004. [Cited: 02 11, 2010.] http://www.nrel.gov/gis/images/us_pv_annual_may2004.jpg.
7. **Nemet, Gregory**. Learning Curves for Photovoltaics. *www.iea.org*. [Online] June 2007. [Cited: 05 03, 2010.] https://www.iea.org/work/2007/learning/Nemet_PV.pdf.
8. PV Module Cost. *www.nrel.gov*. [Online] [Cited: 02 11, 2010.] <http://www.nrel.gov/docs/fy01osti/29462.pdf>.
9. NCPV Best Cells. *www.nrel.gov*. [Online] [Cited: 05 03, 2010.] www.nrel.gov/ncpv/thin_film/docs/kaz_best_research_cells.ppt.
10. **Ruggiero, Christopher**. *A Ray Tracing Investigation of Light Trapping due to Grooves in Solar Cell*. Cambridge, MA : MIT, 2007.
11. *Investigations of Random Pyramid Texture on the Surface of Single Crystalline Silicon for Solar Cells*. **Xin Zhu, Lei Wang, Deren Yang**. Hangzhou : Solar World Congress 2007, 2007.
12. *Micropyramidal Hillocks on KOH etched {100} silicon surfaces: formation, prevention and removal*. **H Schroder, E Obermeier, A Steckkenborn**. 1999, Berlin, Germany : J. Micromech. Microeng., 1998, Vols. 139-145.
13. *Texturing Industrial Multicrystalline Silicon Solar Cells*. **D. Macdonald, A. Cuevas, M. Kerr, C. Samundsett, D. Ruby, S. Winderbaum and A. Leo**. Acton Australia : ISES 2001 Solar World Congress, 2001.

14. *Texturing of Multicrystalline Silicon with Acidic Wet Chemical Etching and Plasma Etching*. **O. Schlutz, G. Emanuel, S.W Glunz, G.P Willeke**. Freiburg, Germany : 3rd World Conference of Photovoltaic Energy Conversion, 2003.
15. *Comparative Study of Different Approaches of Multicrystalline Silicon Texturing for Solar Cell Fabrication*. **U. Gangopadhyay, S.K. Dhungel, P.K. Basu, S.K. Dutta, H. Saha, J.Yi**. 285-289, s.l. : Solar Energy Materials and Solar Cells, 2007, Vol. 91.
16. **Emanuel Sachs, James Brecht**. *Solar Cell Light Trapping and Metallization using a Self-Aligning Mask*. Cambridge : MIT, 2007.
17. *Chemical Etching of Silicon I. The System HF, HNO₃, and H₂O*. **H. Robbins, B.Schwartz**. 6, New Port Beach, CA : Journal of the Electromechanical Society, June 1959, Vol. 106, pp. 505-508.
18. *Chemical Etching of Silicon II. The System HF, HNO₃, H₂O and HC₂H₃O₂*. **H. Robbins, B.Schwartz**. 2, New Port Beach, CA : Journal of the Electrochemical Society, February 1960, Vol. 107, pp. 108-111.
19. *Acid-Based Etching of Silicon Wafers: Mass-Transfer and Kinetics Effects*. **Milind S. Kulkarni, Henry F. Erk**. 1, Saint Peters, MI : Journal of the Electromechanical Society, 2000, Vol. 147, pp. 176-188.
20. **Shimura, F**. *Semiconductor Silicon Crystal Technology*. San Diego : Academic Press, Inc, 1989. pp. 184-186.
21. *Reactivity of Crystalline Silicon in the system HF-HNO₃-H₂O (A Novel Study)*. **Rover, Ingo, et al**. Paris : European PV Solar Energy Conference, 2004.
22. *The Effect of H₂SiF₆ on the surface morphology of textured multi-crystalline silicon*. **Wenke Weinreich, Jorg Acker, Iris Graber**. Dresden, Germany : Institute of Physics Publishing, 2006, Semicond. Sci. Technol., Vol. 21, pp. 1278-1286.
23. **Frank Incropera, David DeWitt**. *Fundamentals of Heat and Mass Transfer*. 5th. s.l. : John Wiley & Son, 2002. p. 391.
24. *Centrifugal Etching*. **al/, R.P. Tijburg et**. 6, Utrecht : Journal of the Electrochemical Society, 2003, Vol. 150, pp. C440-C444.
25. **Bennett, Charles A**. Chapter 3- Reflection and Refraction. *Principles of Physical Optics*. s.l. : John Wiley & Sons, 2008.
26. Total Internal Reflection. [www.wikipedia.org](http://en.wikipedia.org/wiki/Total_internal_reflection). [Online] 03 11, 2010. [Cited: 03 22, 2010.] http://en.wikipedia.org/wiki/Total_internal_reflection.
27. Total Internal Reflection. [www.wikipedia.org](http://en.wikipedia.org/wiki/File:Total_internal_reflection.jpg). [Online] [Cited: 03 22, 2010.] http://en.wikipedia.org/wiki/File:Total_internal_reflection.jpg.
28. **Williams, Kirt R**. Etch Rates for Micromachining Processing—Part II. *Journal of Microelectromechanical Systems*. December 2003, Vol. 12, 6, pp. 761-778.

29. **Schmela, Michael.** Wet Etching Equipment for Wafer-Based PV cells. *Photon International*. December 2009, p. 170.
30. **Anne Kreutzmann, Michael Schmela.** Emancipation from Subsidy Programs. . *Photon International*. 12, 2008.
31. May 2008 National Occupational Employment and Wage Estimates. *www.bls.gov*. [Online] [Cited: 05 03, 2010.] http://www.bls.gov/oes/2008/may/oes_nat.htm#b00-0000.
32. **Schmela, Michael.** Dopers Market Survey. *Photon International*. August 2009, p. 160.
33. **Jimenez, David.** Cost of Ownership and Overall Equipment Efficiency: a Photovoltaics Perspective. *Photovoltaic International*. Sixth, November 2009, pp. 16-22.
34. *19.8% efficient "honeycomb" textured multicrystalline and 24.4% monocrystalline silicon solar cells.* **Zhao, Jianhua, et al.** 14, s.l. : Applied Physics Letters, 1998, Vol. 73.
35. **Song, Joonki, et al.** *The True Cost of solar power: Race to 1 \$/W.* s.l. : Photon Consulting, 2009.

Appendix A:

Matlab code for trench evaluation:

```
% Finding the minimum Aspect Ratio necessary for a 21 degree line to
% escape a trench and not bounce back into the surface of Silicon

x=[-10:0.01:10];
W = 20; % width
D = 10; % Depth
c = D/(W/2)^2
AR = D/W

y = c.* x.^2;
%y_prime = -0.38.*x;
s = tan(21/180 * pi);

x_tang_21 = - s/(2*c);
y_tang_21 = c*x_tang_21^2;
b = y_tang_21 + s*x_tang_21; % y= a*x + b => b = y-a*x
y_tang = -s*x + b;
d = y_tang_21 - (1/s)*x_tang_21;
y_tang_perp = (1/s)*x + d;
t = tan(48/180*pi);
e = y_tang_21 - t*x_tang_21;
y_21_bounce = t*x + e;

plot (x,y)
axis equal
hold on
%plot (x,y_prime)
plot (x,y_tang,'--')
plot (x,y_tang_perp,'--')
plot (x,y_21_bounce,':')
xlabel('µm')
ylabel('µm')
legend('Trench Profile','Tangent 20.9 deg','Perpendicular to
Tangent','Reflected Light Ray')
```

```

% Finding the minimum Aspect Ratio necessary for a 21 degree line to
% escape a trench and not bounce back into the surface of Silicon

x=[-10:0.01:10];
W = 20; % width
D = 20; % Depth
c = D/(W/2)^2
AR = D/W

y = c.* x.^2;
%y_prime = -0.38.*x;
s = tan(21/180 * pi);

x_tang_21 = - s/(2*c);
y_tang_21 = c*x_tang_21^2;
b = y_tang_21 + s*x_tang_21; % y= a*x + b => b = y-a*x
y_tang = -s*x + b;
d = y_tang_21 - (1/s)*x_tang_21;
y_tang_perp = (1/s)*x + d;
t = tan(48/180*pi);
e = y_tang_21 - t*x_tang_21;
y_21_bounce = t*x + e;

figure (2)
plot (x,y)
axis equal
hold on
%plot (x,y_prime)
plot (x,y_tang,'--')
plot (x,y_tang_perp,'--')
plot (x,y_21_bounce,':')
xlabel('µm')
ylabel('µm')
legend('Trench Profile','Tangent 20.9 deg','Perpendicular to
Tangent','Reflected Light Ray')

```

```

x=[-10:0.01:10];
W = 20; % width
%D = 10;% Depth
c = 0.13%D/(W/2)^2

AR = c*(W/2)^2/W

y = c.* x.^2;
%y_prime = -0.38.*x;
s = tan(21/180 * pi);

x_tang_21 = - s/(2*c);
y_tang_21 = c*x_tang_21^2;
b = y_tang_21 + s*x_tang_21; % y= a*x + b => b = y-a*x
y_tang = -s*x + b;
d = y_tang_21 - (1/s)*x_tang_21;
y_tang_perp = (1/s)*x +d;
t = tan(48/180*pi);
e = y_tang_21 - t*x_tang_21;
y_21_bounce = t*x + e;

figure (3)
plot (x,y)
axis equal
hold on
%plot (x,y_prime)
plot (x,y_tang,'--')
plot (x,y_tang_perp,'--')
plot (x,y_21_bounce,':')
xlabel('µm')
ylabel('µm')
legend('Trench Profile','Tangent 20.9 deg','Perpendicular to
Tangent','Reflected Light Ray')

```

Matlab Code for Boundary Layer

```
% Boundary Layer Calculations for Trenches Fluid boundary layer
rho = 998;% density of water [kg/m^3]
mu = 959e-6; % viscosity of water [N.s/m^2]
nu = mu / rho; % Kinematic viscosity
V1 = 1; % [m/s]
V2=0.5;
V3=0.1;
V4=2;
V5=3;
x = [0:1e-7:2e-5]; % x dimension in meter
Rex1 = V1.*x/nu;
Rex2 = V2.*x/nu;
Rex3 = V3.*x/nu;
Rex4 = V4.*x/nu;
Rex5 = V5.*x/nu;% Reynolds number
T1=5.*x./sqrt(Rex1);
T2=5.*x./sqrt(Rex2);
T3=5.*x./sqrt(Rex3);% Boundary Layer thickness.
T4=5.*x./sqrt(Rex4);
T5=5.*x./sqrt(Rex5);
x_um = x.*1e6;
T1_um = T1.*1e6;
T2_um = T2.*1e6;
T3_um = T3.*1e6;
T4_um = T4.*1e6;
T5_um = T5.*1e6;

plot(x_um, T1_um, 'b')
hold on
plot(x_um, T2_um, '+')
plot(x_um, T3_um, ':')
plot(x_um, T4_um, '--')
plot(x_um, T5_um, '-.')

xlabel('Distance x in um')
ylabel('Boundary layer thickness in um')
legend('V = 1 m/s', 'V= 0.5 m/s', 'V= 0.1 m/s', 'V= 2 m/s', 'V= 3 m/s')
```